

Machine learning on DNA-encoded library count data using an uncertainty-aware probabilistic loss function

Katherine S. Lim,^{†,‡} Andrew G. Reidenbach,[¶] Bruce K. Hua,^{§,¶} Jeremy W. Mason,^{¶,||} Christopher J. Gerry,^{§,¶} Paul A. Clemons,^{*,¶} and Connor W. Coley^{*,†,⊥,¶}

[†]*Department of Electrical Engineering and Computer Science, Massachusetts Institute of Technology, 77 Massachusetts Avenue, Cambridge, Massachusetts 02139, United States*

[‡]*Department of Biology, Massachusetts Institute of Technology, 77 Massachusetts Avenue, Cambridge, Massachusetts 02139, United States*

[¶]*Chemical Biology and Therapeutics Science Program, Broad Institute, 415 Main Street, Cambridge, Massachusetts 02142, United States*

[§]*Department of Chemistry and Chemical Biology, Harvard University, 12 Oxford Street, Cambridge, Massachusetts 02138, United States*

^{||}*Novartis Institutes for BioMedical Research, Cambridge, Massachusetts 02139, United States*

[⊥]*Department of Chemical Engineering, Massachusetts Institute of Technology, 77 Massachusetts Avenue, Cambridge, Massachusetts 02139, United States*

E-mail: pclemons@broadinstitute.org; ccoley@mit.edu

Abstract

DNA-encoded library (DEL) screening and quantitative structure-activity relationship (QSAR) modeling are two techniques used in drug discovery to find novel small molecules that bind a protein target. Applying QSAR modeling to DEL selection data can facilitate the selection of compounds for off-DNA synthesis and evaluation. Such a combined approach has been done very recently by training binary classifiers to learn DEL enrichments of aggregated "disynthons" in order to accommodate the sparse and noisy nature of DEL data. However, a binary classification model cannot distinguish between different levels of enrichment, and information is potentially lost during disynthon aggregation. Here we demonstrate a regression approach to learning DEL enrichments of individual molecules, using a custom negative-log-likelihood loss function, that effectively denoises DEL data and introduces opportunities for visualization of learned structure-activity relationships. Our approach explicitly models the Poisson statistics of the sequencing process used in the DEL experimental workflow under a frequentist view. We illustrate this approach on a DEL dataset of 108,528 compounds screened against carbonic anhydrase (CAIX), and a dataset of 5,655,000 compounds screened against soluble epoxide hydrolase (sEH) and SIRT2. Due to the treatment of uncertainty in the data through the negative-log-likelihood loss used during training, the models can ignore low-confidence outliers. While our approach does not demonstrate a benefit for extrapolation to novel structures, we expect our denoising and visualization pipeline to be useful in identifying structure-activity trends and highly enriched pharmacophores in DEL data. Further, this approach to uncertainty-aware regression modeling is applicable to other sparse or noisy datasets where the nature of stochasticity is known or can be modeled; in particular, the Poisson enrichment ratio metric we use can apply to other settings that compare sequencing count data between two experimental conditions.

Introduction

The discovery of new small-molecule therapeutics or chemical probes often starts with finding compounds with affinity to a protein of interest. Most existing medicines depend on such interactions between small molecules and therapeutically relevant proteins.^{1,2} To find molecules that selectively bind a protein of interest, it can be valuable to synthesize and screen diverse libraries of small molecules. DNA-encoded libraries (DELs) are one technology for achieving this goal.³⁻⁶

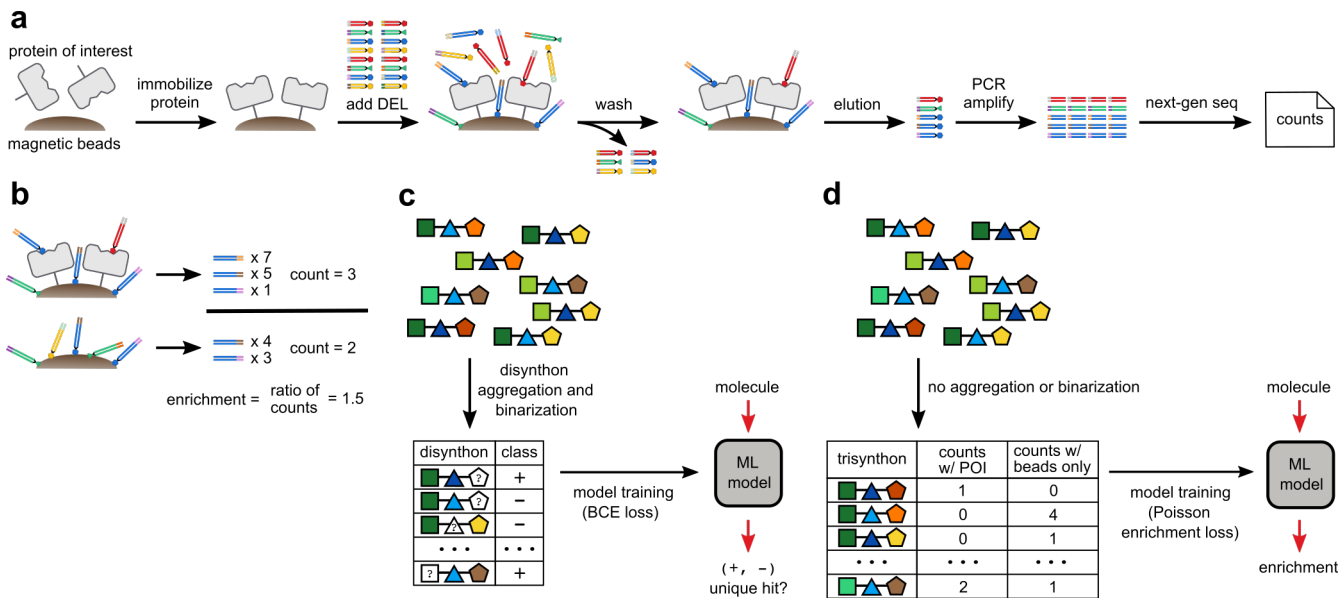


Figure 1: Approaches to analyzing DNA-encoded library (DEL) selection data to infer structure-activity relationships. **(a)** DEL experimental workflow. **(b)** Classic way of getting hits: raw normalized counts. **(c)** McCloskey et al.’s approach: binary classification of “disynthons”.⁷ **(d)** Our approach: regression task on “trisynthons,” taking uncertainty into account. The trisynthon drawing style was adapted from McCloskey et al.).

DELs are constructed by split-pool synthesis, which involves generating a combinatorially large number (up to trillions) of small molecules attached to single- or double-stranded DNA “barcodes” used to identify the molecules. These DNA-tagged molecules are then screened for binding against a protein of interest (POI). To do this, the POI is immobilized, and the DEL molecules are incubated with the POI. Molecules that have weaker affinity for the POI (non-binders) are removed by washing, and the remaining stronger binders are

eluted. The binders are then identified via next-generation sequencing of their DNA tags after amplification by PCR, and the sequencing reads are processed into *counts* (number of observations) for each barcode (Figure 1a). These *counts* are used to calculate an *enrichment* value for each small molecule after normalization (e.g., to a beads-only control condition), with a higher enrichment value ostensibly indicating higher binding affinity to the POI (Figure 1b), although a direct quantitative link has not been established,^{8,9} potentially due to confounding factors such as chemical yields during library synthesis, baseline abundances of library members, stringency of washing, and PCR sensitivity.^{10–15} A subset of compounds are selected for follow-up investigation via on- or off-DNA validation binding assays. These compounds may be determined based on various factors, such as high enrichments, raw counts, selective enrichment across related protein targets, enrichment across multiple protein concentrations, chemical yield, structural similarity to other predicted hits, and physicochemical properties.^{3,14–18} However, count values in DEL screens are generally noisy and sparse, meaning that exclusively following up on the molecules with highest enrichment values (potentially with additional filtering based on other properties, as mentioned above) may leave out many promising molecules and overlook potentially useful structure-activity relationship (SAR) information. Aggregation of enrichment data, e.g., at the level of “monosynthons” (all molecules with one building block in common) or “disynthons” (all molecules with two building blocks in common), may help denoise counts; however, information about individual molecules (i.e., “trisynthons” for libraries constructed from three families of building blocks) is lost in the process of aggregation. In addition, the top hits may be challenging to synthesize off DNA, have poor predicted solubility, or be the product of prospective side reactions, limiting the ability of researchers to validate their perceived affinity.

To address these issues, quantitative structure-activity relationship (QSAR) modeling can enable a more automated and holistic way of codifying relationships between molecule structure and protein-binding activity. QSAR modeling typically involves learning a math-

emational relationship based on labeled (structure, activity) data.^{19,20} In the case of DEL data, QSAR modeling might provide a smooth, continuous mapping from molecular structure to enrichment as a proxy measure of protein-binding affinity, with the caveat that the intended structure of a DEL member may not have been what was actually synthesized. Such a model could be used in a virtual screening setting to evaluate libraries of candidate molecules, including ones not present in the original DEL.

While QSAR modeling is ubiquitous in small-molecule drug discovery, it had not been applied to DELs until very recently.⁷ McCloskey et al. applied QSAR modeling to DEL data by grouping molecules and using their aggregated enrichment data to label each group as a competitive binder to the POI or not—a binary classification problem (Figure 1c).⁷ Aggregating molecules at the level of disynths partially mitigates the sparsity of DEL data and increases the certainty of assigned labels. QSAR models were trained on good/bad disynths and used to screen compounds in a virtual make-on-demand library, ultimately leading to the successful identification of hits with micromolar activity. However, two potential downsides to this modeling approach are that (a) models cannot distinguish between different levels of enrichment (e.g., values of 1.5 and 10.0 are both “enriched” in a binary sense but not equally so) and (b) information about the enrichment of individual molecules is lost during aggregation.

In this work, we explore an alternate approach to combining QSAR modeling and DEL data in a regression formulation that avoids both the binarization and aggregation of enrichment data (Figure 1d). While we do not demonstrate ability to generalize to new chemical structures as McCloskey et al.⁷ achieved, we do show that the models can effectively de-noise DEL data due to the novel uncertainty-aware loss function used during training. Such smoothing of DEL data may allow for the elucidation of patterns in SAR and weaker binders that would otherwise be obscured by noise. We also present a pipeline for visualization of the learned SAR of our fingerprint-based models, which in general can be used to improve the utility of such models’ predictions for medicinal chemists. Specifically, understanding the

learned SAR of such models increases confidence in top predicted compounds and allows for rational modification of structures to improve synthetic accessibility or solubility as needed to facilitate experimental validation off-DNA. In our approach, we use a probabilistic loss function that we argue is more suitable to modeling DEL data than standard regression loss functions like mean-squared error (MSE) due to the stochastic nature of how the data are acquired. Because the next-generation sequencing step of DEL synthesis corresponds well with a Poisson distribution,^{21–23} we can define a loss function that accounts for the uncertainty that results from Poisson sampling. Mathematically, the goal is for the model to predict enrichment values that minimize the negative log-likelihood (NLL) of failing to reject a null hypothesis that the true enrichment ratio equals the predicted enrichment ratio under a two-sided test given the observed barcode counts that we measure in a DEL experiment; the true enrichment value for each molecule corresponds to the (unknown) ratio of the molecule’s relative abundance after affinity selection to the molecule’s relative abundance in a beads-only control experiment. We provide an example of this loss function’s treatment of uncertainty (Figure 2c; Methods).

We evaluated and compared model performance using three different molecule representations (Figure 2a; one-hot encoding of building blocks, Morgan circular fingerprints,²⁵ and molecular graphs), two different model types (Figure 2b; feed-forward neural networks and directed message-passing networks²⁶), and eight data splits—ways of dividing molecules in a dataset for model training and evaluation (Figure 2d; Methods; random split and various cycle splits). We trained and evaluated these QSAR models on two DELs containing 108,528 and 5,655,000 compounds corresponding to DOS-DEL-1 from Gerry et al.²⁷ (abbreviated here as DD1S; in this paper, the names DD1S and DOS-DEL-1 are used interchangeably) and a derivative of DEL-A from Clark et al.³ (referred to here as the triazine library) (Table S1). DOS-DEL-1 was tested against carbonic anhydrase IX (CAIX) as a model protein target, for which we expected to confirm that benzenesulfonamides are active pharmacophores; the triazine library was tested against soluble epoxide hydrolase (sEH) and

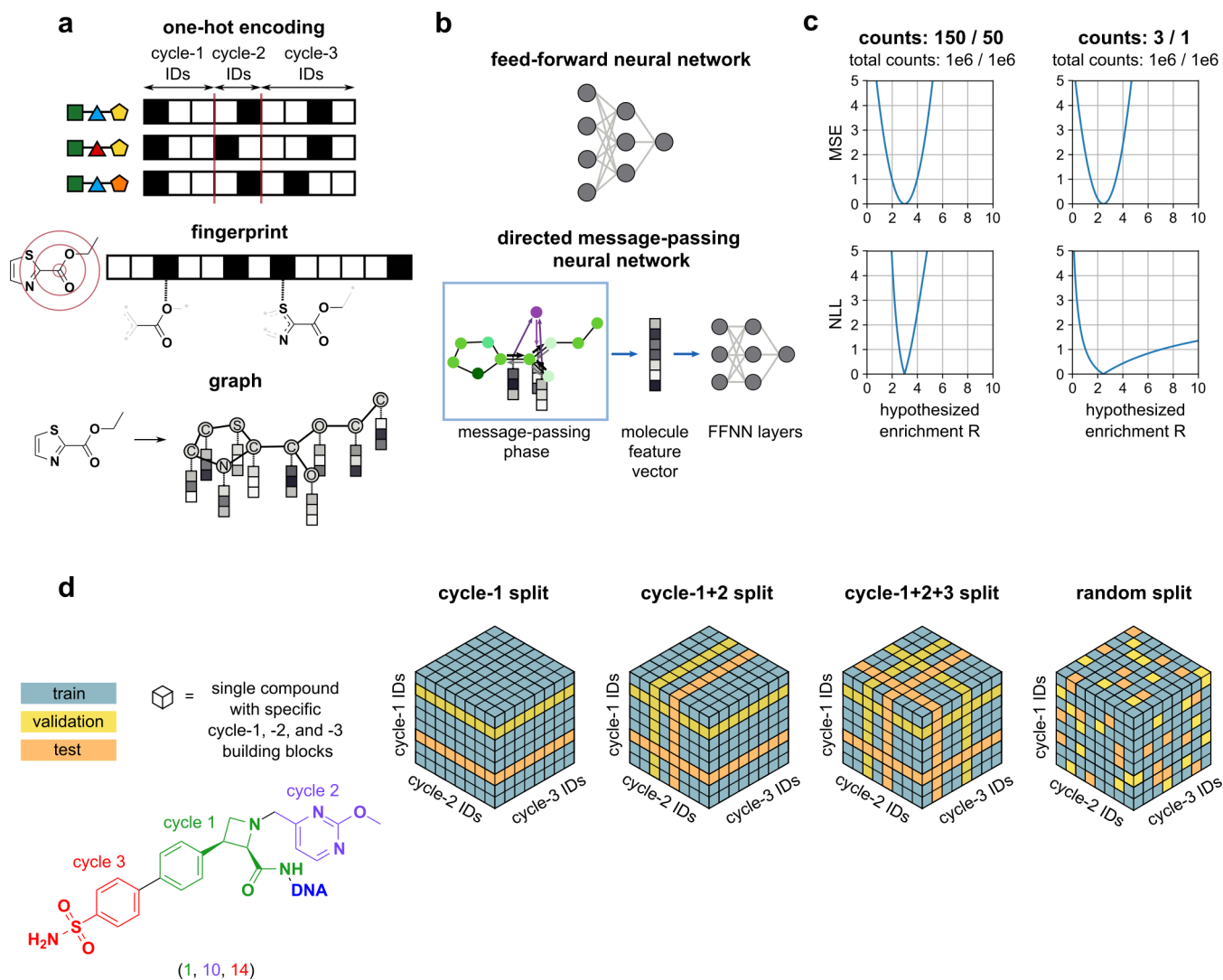


Figure 2: **(a)** Molecule representations. **(b)** Model architectures (message passing network drawing style adapted from Wu et al.). **(c)** Training objectives / loss functions for theoretical count values. **(d)** How molecules in a dataset are divided for model training and evaluation (data splits). NLL: negative-log likelihood; MSE: mean-squared error.

SIRT2. We show that models trained with a NLL loss function outperform baseline models trained using a MSE loss without treatment of data uncertainty, in addition to random and weak (k-nearest-neighbors) baselines. The NLL-trained models also reveal an ability to act as structural regularizers, smoothing noisy enrichment values for individual compounds in a DEL, and enable visualizations of learned SAR to inform follow-up medicinal chemistry. Due to the general applicability of NLL loss functions to training regression models in maximum likelihood settings, we expect our approach to apply to regression modeling on other sparse or noisy datasets where the stochasticity is known or can be modeled.

Results

Single-task model performance is improved when trained on the NLL

The first evaluation was intended to directly compare the models trained using the NLL loss function to models trained using the MSE loss and a point estimate of the calculated enrichment (“pt”) without regard for uncertainty, in addition to k-nearest-neighbors (KNN) and random baselines that also use these point estimates. For each dataset, model type, and data split type, the average test NLL was calculated over several trials, where each trial used a different random seed for data splitting (Figures 3, S11; Tables S4, S5, S6). Overall, the models explicitly trained using the uncertainty-aware Poisson enrichment loss function show higher performance than the baseline point prediction, KNN, and random models when evaluated in terms of that same metric. For completeness, we also calculated the test MSE loss and rank correlation coefficient for the same models when treating the calculated enrichments as precise measurements, which we know not to be the case (Figures S13, S14, S15, S16; Tables S7, S8, S9, S10, S11, S12). We note that the KNN baseline models tend to show poorer performance than the random baselines; this is reasonable given that the KNN model is likely trying to fit to noisy data, whereas the predict-all-ones random

baseline benefits from a smoothing effect since the average enrichment across all compounds in the test set is likely close to 1. The shuffle-predictions random baseline (randomly shuffling the test-set predictions of a FP-FFNN model) similarly benefits from the FP-FFNN’s predicted enrichments likely being close to the average.

The three molecular representations used—a one-hot encoded feed-forward network, a fingerprint-based feed-forward network, and the graph-based directed message-passing neural network—show similar performance within each data split. Considering that one-hot models are incapable of generalizing to new chemical structures, it is surprising to see them perform comparably to the fingerprint-based feed-forward networks and message-passing networks on the cycle splits (*vide infra*). Whereas the random split only requires a model to interpolate to new combinations of chemical building blocks seen during training, cycle splits require the model to generalize to chemical building blocks not included in either the training or validation sets.

In addition, the models trained using a cycle split generally have larger variability in performance than the models trained using a random split over the 5 repeated trials. This variability is attributable to models getting “lucky” or “unlucky” in terms of which building blocks happen to appear in their test sets and whether the distribution of enrichments differs between the training and test sets. In particular, prediction on the test set may be difficult for certain cycle splits if the test-set building blocks are structurally dissimilar to the building blocks used for training, since the model will not generalize well from the structures it has seen during training to make predictions for the test-set compounds. Prediction on the test set may also be difficult if the test- and training-set building blocks are similar in structure but have very different effects on enrichment (e.g., as in activity cliffs, where it would be unreasonable to expect a model to detect the sharp changes in activity, having never seen the structures corresponding to them). For instance, for the DD1S CAIX dataset, there is an activity cliff for compounds with a benzenesulfonamide; prediction on the test set for this dataset may be difficult if the test set includes building blocks with a benzenesulfonamide

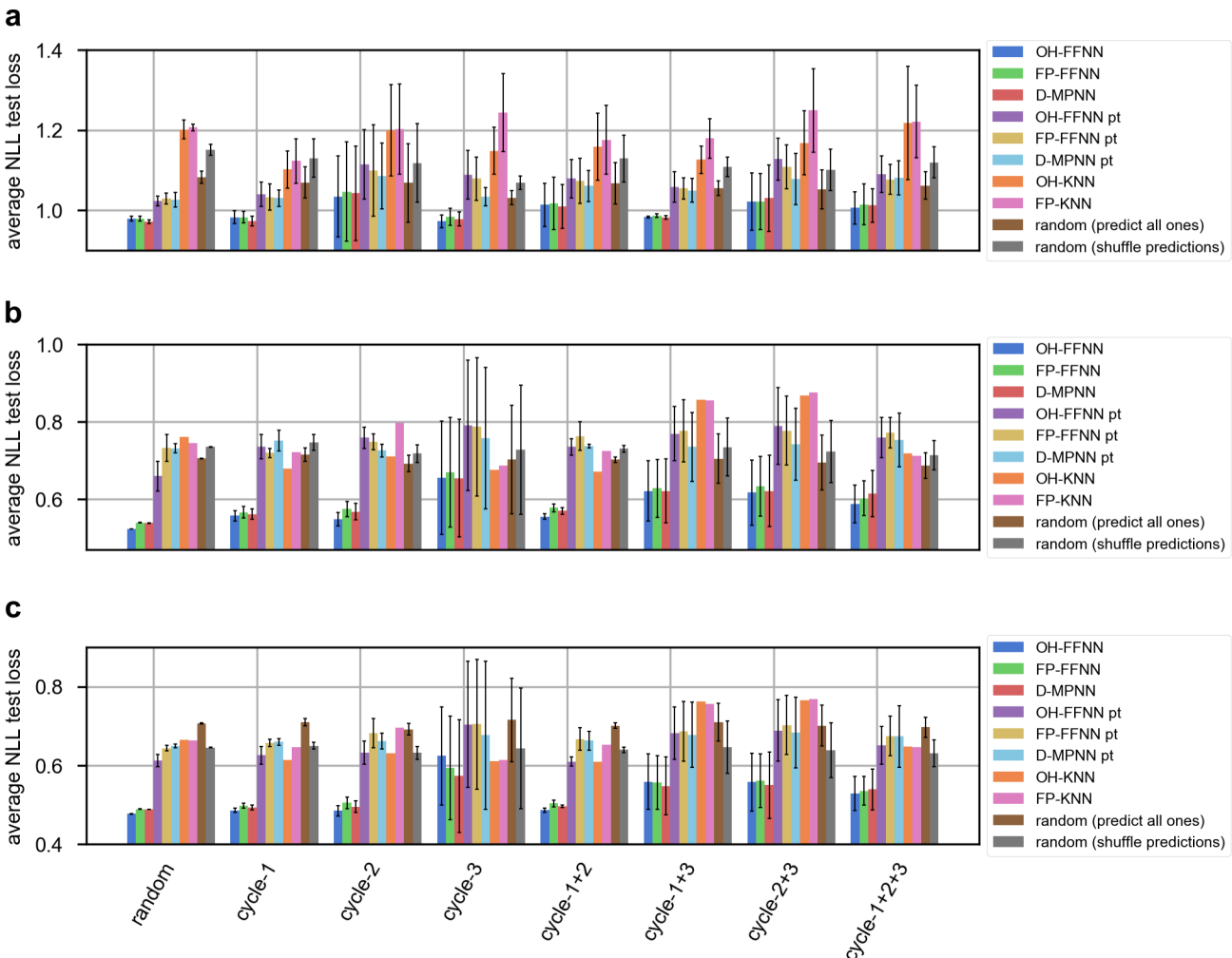


Figure 3: Comparison of model performance, as measured by negative log-likelihood (NLL) loss. OH: one-hot; FP: fingerprint; FFNN: feed-forward neural network; D-MPNN: directed message-passing neural network; KNN: k-nearest neighbors. The NLL test losses of the NLL-trained models (OH-FFNN, FP-FFNN, D-MPNN) are compared to those of the baseline point-prediction-trained models (OH-FFNN pt, FP-FFNN pt, D-MPNN pt), k-nearest-neighbors models (OH-KNN, FP-KNN), and random models (predict all ones, shuffle predictions), for various data splits (*cf.* Figure 2d) on the (a) DD1S CAIX, (b) triazine sEH, (c) triazine SIRT2 datasets. Error bars represent \pm one standard deviation. OH-FFNN, FP-FFNN, OH-FFNN pt, FP-FFNN pt, random (predict all ones), and random (shuffle predictions) results are averaged over five trials for each dataset; D-MPNN and D-MPNN pt results are averaged over five trials for the DD1S CAIX dataset and over three trials for the triazine sEH and triazine SIRT2 datasets; OH-KNN and FP-KNN results are averaged over five trials for the DD1S CAIX dataset and are single trials on a random 10% of the test set for the triazine sEH and triazine SIRT2 datasets. The result of each trial is shown separately in the SI (Figure S11).

while the training set does not.

As such, among the various cycle splits, certain cycle splits have considerably higher variability in test loss, depending on the dataset. For example, the DD1S CAIX dataset shows the highest variability for test loss using the cycle-2 split, mostly due to high test losses for one of the trials (the trial using random seed 4; Figure S11). The higher test loss for this trial may be explained by a distributional shift in calculated enrichments for the compounds in the trial’s test set (Figure S21). For the triazine sEH and triazine SIRT2 datasets, the cycle-3 split (and to a lesser extent the cycle-1+3 and cycle-2+3 splits) shows the greatest variability. Certain cycle-3 building blocks (building blocks 58, 157, and 179) are uniquely in the test set for the cycle-3, cycle-1+3, and cycle-2+3 splits for one of the five random seeds; the models’ abilities to extrapolate to these particular structures seem to be poor.

Performance on DOS-DEL-1 for CAIX shows denoising ability and illustrates connection between counts and uncertainty levels

In addition to the quantitative metrics (Figure 3) that summarize overall performance, we sought a more qualitative evaluation of model fit. The correlation between the predicted and calculated enrichments of the test-set compounds for a random split using a fingerprint-based model indicates good agreement (Figures 4a, S17). Further, there is visible separation in predicted enrichments between the compounds with a benzenesulfonamide substructure and the compounds without a benzenesulfonamide substructure (Figure 4b), which is known to be an important motif for binding CAIX’s zinc atom in the active site.^{27–29} We provide analogous visualizations of predicted enrichments for benzenesulfonamides versus non-benzenesulfonamides for an MSE-loss-trained fingerprint-based model on the same split of the data (Figure S18). Disynthon aggregation results in a lesser extent of separation in the enrichments of compounds with or without a benzenesulfonamide, further suggesting that our trisynthon-based approach is particularly useful for denoising counts without obscuring

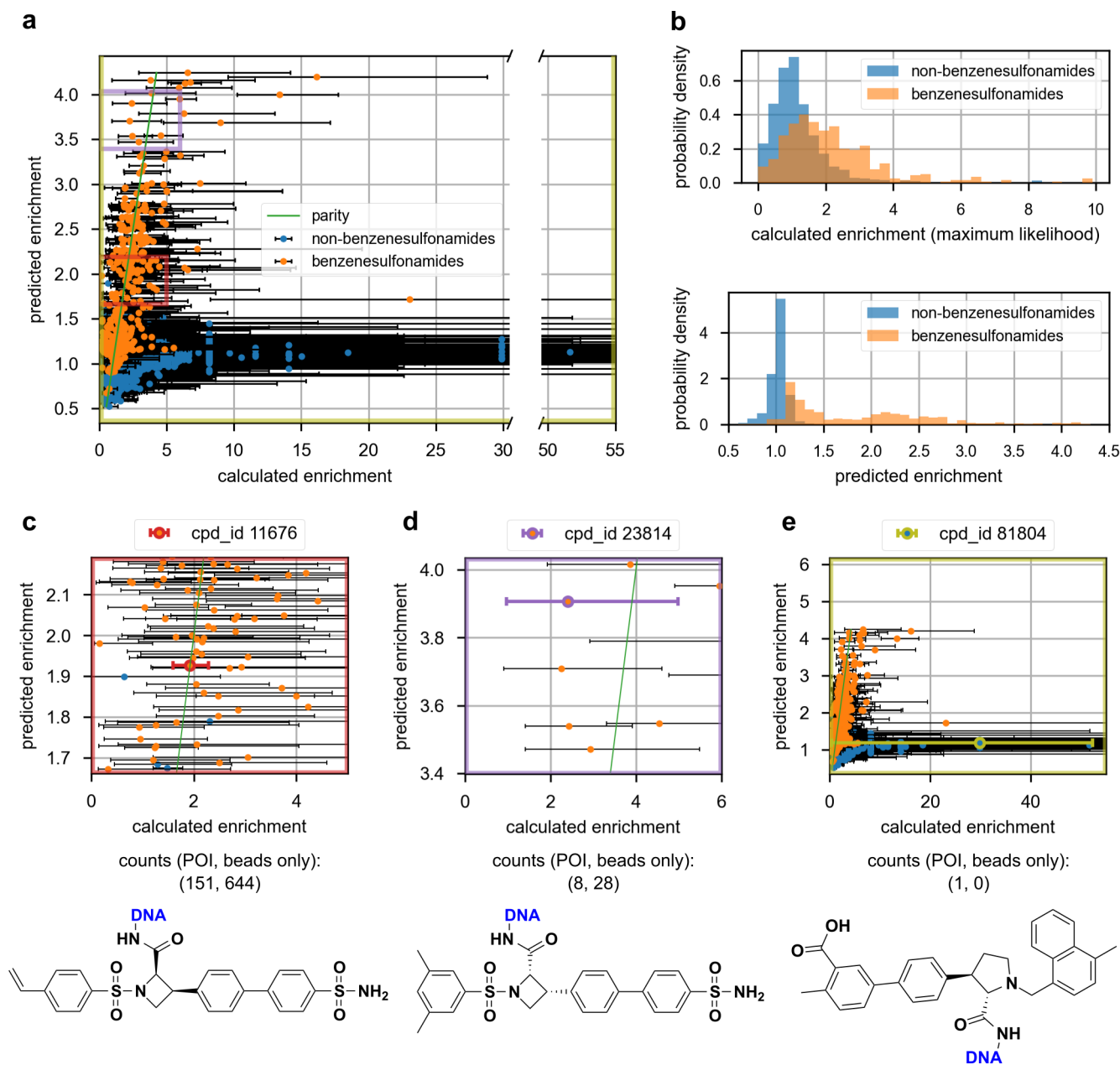


Figure 4: **(a)** Scatter plot of predicted and calculated enrichments for the test-set compounds of a FP-FFNN on a random split (*cf.* Figure 2d) of the DD1S CAIX dataset. The green parity line is the identity function, for reference. **(b)** Histograms of calculated and predicted enrichments for the test-set compounds of a FP-FFNN on a random split (*cf.* Figure 2d) of the DD1S CAIX dataset. The horizontal axis cutoff of 10 in the histogram of calculated enrichments is arbitrary, for the sake of legibility. **(c)** Close-up of a compound (ID 11676) with high counts (POI, beads only: 151, 644) and low uncertainty. The predicted enrichment of 1.93 approximates the calculated enrichment of 1.92. **(d)** Close-up of a compound (ID 23814) with low counts (POI, beads only: 8, 28) and high uncertainty. The predicted enrichment of 3.91 is high relative to the calculated enrichment of 2.41. **(e)** Close-up of a compound (ID 81804) with low counts (POI, beads only: 1, 0) and high uncertainty. The predicted enrichment of 1.19 is low relative to the calculated enrichment of 29.89. The total barcode counts in this dataset are 638,831 and 5,208,230 for the POI and beads-only conditions, respectively. Error bars represent 95% confidence intervals for calculated enrichments; the horizontal axis values of the scatter plot datapoints are maximum-likelihood calculated enrichments (calculated using $z = 0$; Methods). Compound IDs (“cpd_id”) are sequential based on building block cycle numbers.

the underlying structure-activity trends (Figure S19).

Examples of individual compounds illustrate the connection between counts and levels of uncertainty in their calculated enrichments (Figure 4cde). For compounds with higher counts and lower uncertainty, reflected by smaller error bars, the predicted enrichment tends to be closer to the calculated enrichment. For compounds with lower counts and higher uncertainty, the predicted enrichment may be further from the calculated enrichment, but not significantly so. For each of the three example compounds, model predictions fall within the 95% confidence interval estimated from the count data (Figure 4cde); averaging over all random splits, 92.94% of model predicted enrichments fall within the 95% confidence interval (Figure 4cde; Table S13).

The low-count high-uncertainty datapoints illustrate a key motivation for using an uncertainty-aware loss function during training. By taking into account the high uncertainty in the calculated enrichments of compounds with low counts during training, the model avoids giving too much weight to such outliers. While these compounds could potentially correspond to potent binders, there is not as much evidence about their enrichment as there is about the enrichment of high-count, low-uncertainty compounds. Further, comparison of example outliers with their nearest neighbors in the DD1S CAIX dataset suggests that these outliers are unlikely to be potent binders, since structurally similar compounds in the dataset have relatively low calculated enrichments (Table S26).

Performance on the triazine library for sEH and SIRT2 shows a coarse correlation between predicted and calculated enrichments

A similar visual inspection of the correlation between predicted and calculated trisynthon enrichments is less informative for the sEH and SIRT2 datasets due to the much larger uncertainties of calculated enrichments. The increase in uncertainties stems from the much larger size of the triazine library (5.7 million compounds compared to 109k for the DD1S CAIX dataset). Since the sequencing depth is not proportionately scaled up, the increase in

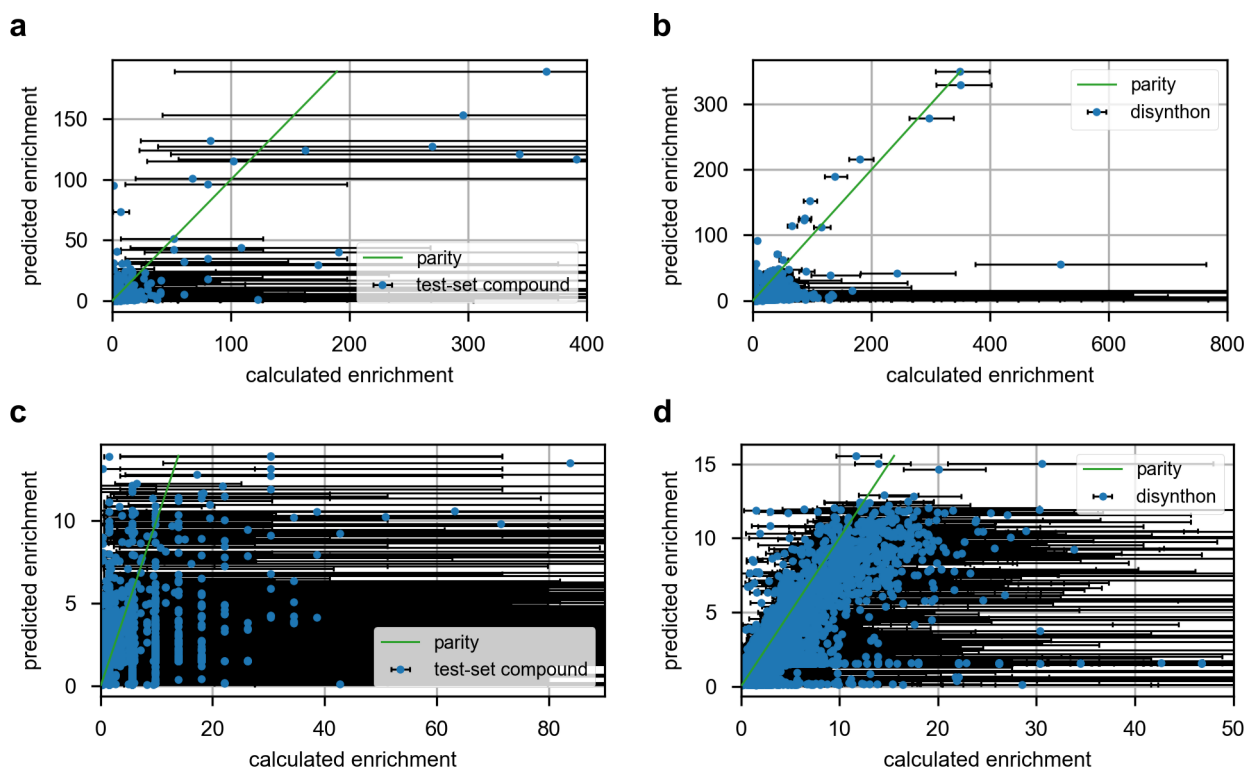


Figure 5: Scatter plot of predicted and calculated enrichments for a random subset (20,000 compounds) of the test set of a FP-FFNN on a random split (*cf.* Figure 2d) of the (a) triazine sEH, (c) triazine SIRT2 dataset, and for all disynthons in the (b) triazine sEH, (d) triazine SIRT2 dataset. The green parity line is the identity function, for reference. Error bars represent 95% confidence intervals for calculated enrichments; the horizontal axis values of the datapoints are maximum-likelihood calculated enrichments (calculated using $z = 0$; Methods).

number of compounds results in fewer average counts per compound (Table S1).

Parity plots for a fingerprint-based feed-forward network on a random split of the triazine sEH and triazine SIRT2 datasets (Figures 5ac, S20ac) show a coarse linear correlation between predicted and calculated enrichments; the same data can be visualized as 2D histograms (Figures S25, S26, S27). We also compared predicted and calculated enrichments of aggregated disynthons on the same datasets (Figures 5bd, S20bd; Methods) and found a clearer linear correlation, suggesting that the coarse correlation for individual compounds may be attributed to the noisiness of the data.

Binary classification baseline comparisons show no evidence of a benefit to regression modeling

As a baseline comparison motivated by McCloskey et al.⁷’s binary classification approach, we trained binary classifiers on each of the datasets, and also evaluated the trained regression models as classifiers. The results (Figures S22, S23, S24; Tables S14, S15, S16) are inconclusive; based on the PR and ROC AUC metrics for classification, there is no evidence of a benefit to regression modeling of these data using a NLL loss function.

Visualization of learned SAR reveals substructures driving enrichment

The ability to interpret what has been learned by a SAR model can improve the utility of its predictions for medicinal chemists.^{30–33} In particular, SAR model interpretation allows researchers to understand the rationale behind top predicted compounds and may facilitate the rational design of more potent binders that can be experimentally validated. As fingerprint-based models are especially conducive to substructure-based interpretation, we explored two ways of visualizing the learned SAR of our fingerprint-based feed-forward networks: atom-centered Gaussian visualizations³⁴ (Figure 6a) and fingerprint bit and substructure importance (Figure 6b). Interpretation of the message-passing neural networks

through atom masking, integrated gradients, or similar substructure importance estimation techniques is left to future work.

Atom-centered Gaussian visualizations provide a qualitative evaluation of model learning and generalization performance

Atom-centered Gaussian visualizations allow for visualization of atomic contributions to model predictions for a given molecule. Each visualization shows the structure of the molecule, with atoms contributing positively to enrichment highlighted in green, and atoms contributing negatively to enrichment highlighted in pink (Figure 6a; Methods). Visualizations of several compounds’ enrichments for fingerprint-based feed-forward networks trained on a random split of each dataset are shown as examples (Figures 6d, S50, 7). For the DD1S CAIX dataset, the visualization algorithm highlights benzenesulfonamides as strongly enriched pharmacophores, as expected (Figure 6d).

The atom-centered Gaussian visualizations for the top test-set compounds predicted by a random split model on the triazine sEH dataset provide qualitative evidence that the models are learning reasonable SAR (Figure S51). We consistently see a trifluoromethylphenyl or dichlorophenyl group as a strongly enriched motif in these top predicted compounds, which is reasonable given that many potent sEH binders reported in the literature contain these substructures, among other fluorinated or chlorinated phenyl substituents.^{35–38} A similar visual evaluation of top predicted compounds for the triazine SIRT2 dataset reveals a cyanothiazole as a strongly enriched motif (Figure S52), although this substructure lacks literature support.

We also used these visualizations to qualitatively evaluate our fingerprint-based models’ empirical abilities to generalize on the triazine sEH and triazine SIRT2 datasets (*cf.* Discussion). More specifically, we generated atom-centered Gaussian visualizations for the top predicted compounds for a model extrapolating on a cycle-1+2+3 split, as well as visualizations of the same compounds for a corresponding model interpolating on a random split

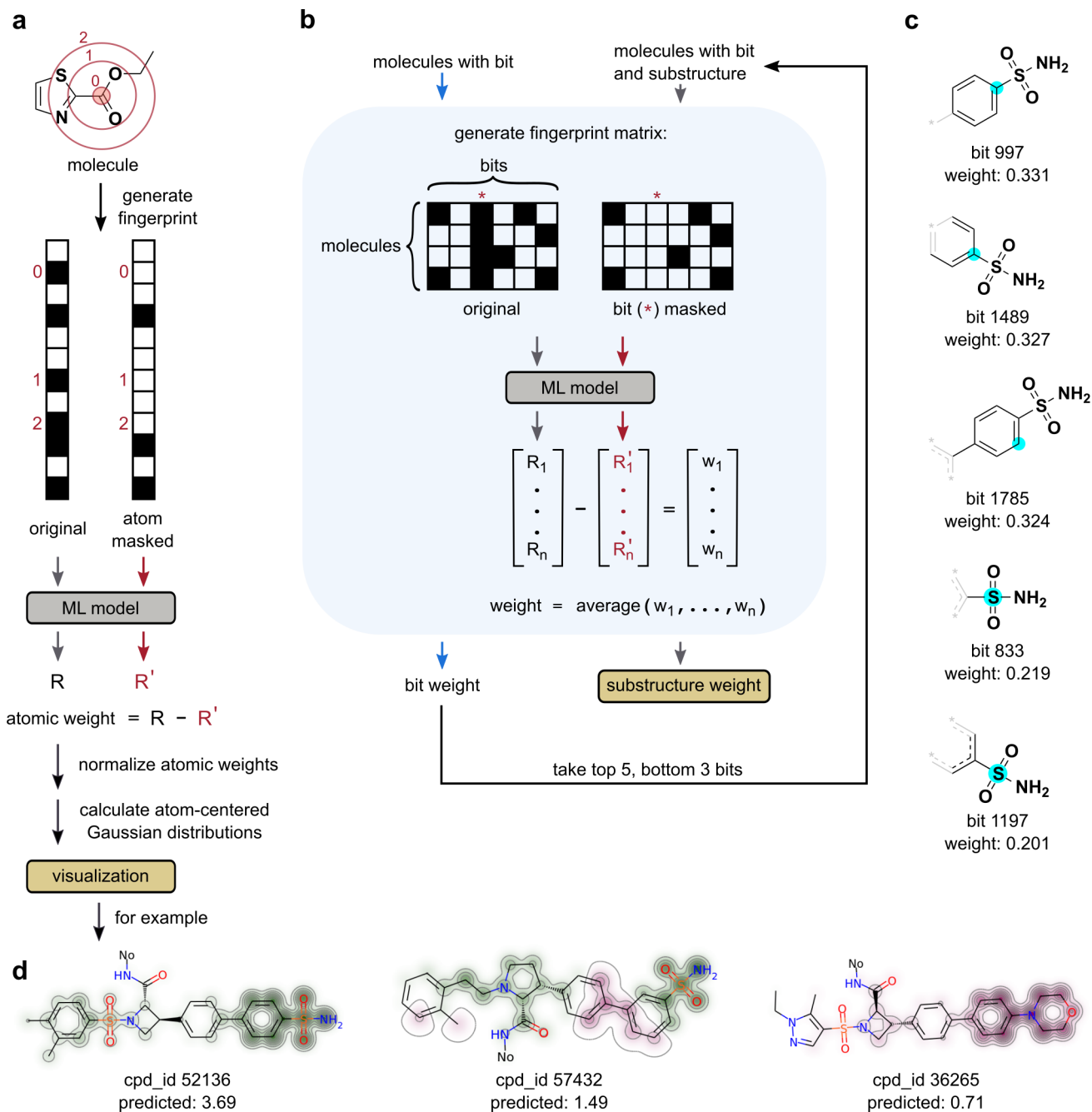


Figure 6: **(a)** Workflow for the generation of atom-centered Gaussian visualizations. **(b)** Workflow for calculating fingerprint bit and substructure importance. **(c)** Top 5 substructures and **(d)** example visualizations for compounds in the DD1S CAIX dataset based on the predictions of a FP-FFNN trained on a random split (*cf.* Figure 2d) of the DD1S CAIX dataset. In the example visualizations, atoms contributing positively to enrichment are highlighted in green, and atoms contributing negatively to enrichment are highlighted in pink, with color intensity corresponding to the level of contribution to enrichment. “No” represents the DNA linker attachment point. Compound IDs (“cpd_id”) are sequential based on building block cycle numbers.

of the data (Figures S53, S54). For the top predicted compounds, we did not observe much similarity between the structures that the cycle-1+2+3 split model and the random split model predict as contributing positively or negatively to enrichment. This dissimilarity in learned SAR suggests that the cycle-1+2+3 split models, having never seen any of the three building blocks, lack the random split models’ understanding of the aspects of the building blocks’ structures that will positively or negatively contribute to overall enrichment.

Bit and substructure importance confirms previously found SAR for CAIX and identifies substructures driving enrichment for sEH and SIRT2

The second approach to SAR visualization involved identifying the fingerprint bits and substructures that contribute most heavily to the predicted enrichment (Figure 6b; *cf.* Methods). This process involved iterating through bit-masked predictions to find the most important fingerprint bits and from those bits identifying the most important corresponding substructures without hand-selecting individual molecules to look at. As Morgan circular fingerprints were used in this study, the result of this analysis is a set of atom-centered neighborhoods of up to radius 3 and their importance weights.

For the DD1S CAIX dataset, the top 5 substructures contributing to enrichment (Figures 6c, S28, S29; Table S17) all correspond to an arylsulfonamide, with the first and third corresponding specifically to a *para*-substituted benzenesulfonamide, the second to a *para*-substituted arylsulfonamide, the fourth to any arylsulfonamide, and the fifth to *para*- and *meta*-substituted arylsulfonamides; note, however, that the only two arylsulfonamide motifs in DD1S are *para*- and *meta*-substituted benzenesulfonamides. These results are consistent with prior observations that the benzenesulfonamide is the most important motif for binding affinity to carbonic anhydrase, and more specifically that compounds with a *para*-substituted benzenesulfonamide are more highly enriched than compounds with a *meta*-substituted benzenesulfonamide.^{27–29} The top 5 bits (and corresponding substructures) from this analysis are consistent across two other random splits of the DD1S CAIX dataset (Fig-

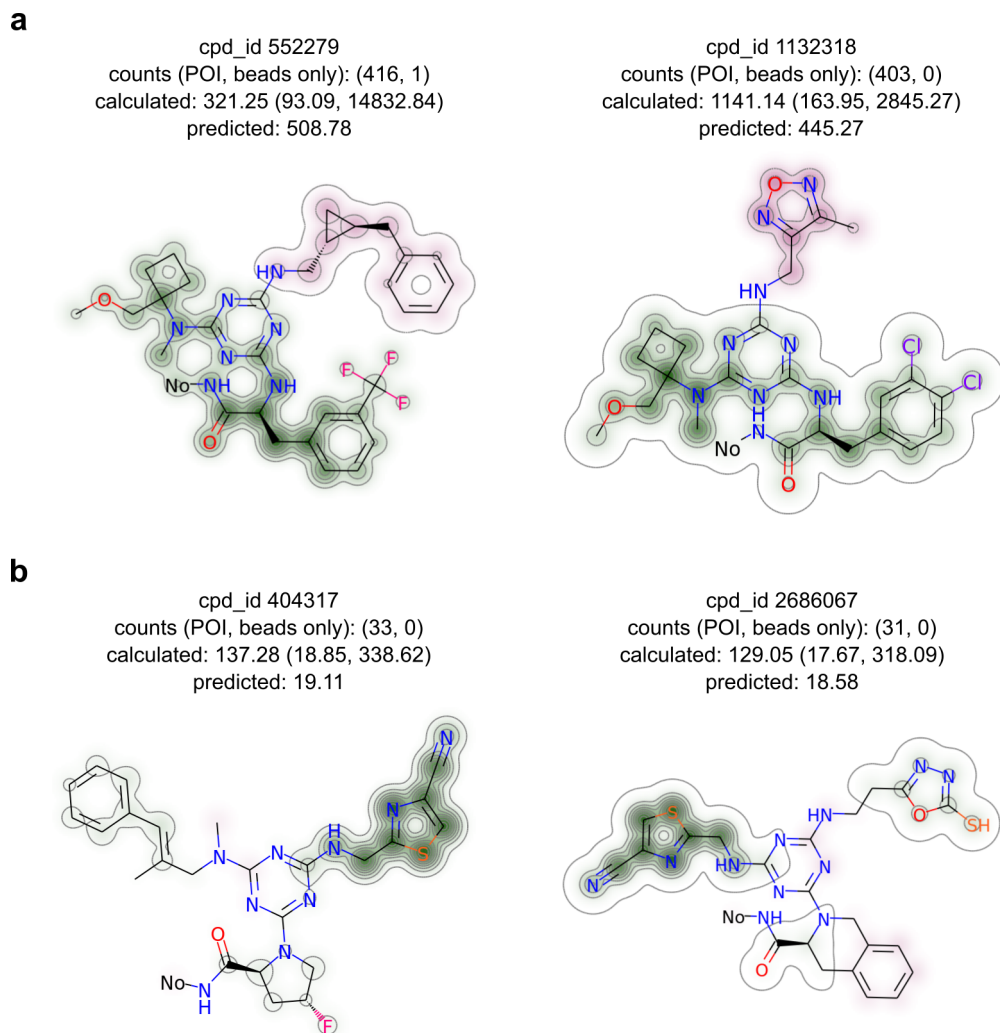


Figure 7: Atom-centered Gaussian visualizations for example compounds in the test set of a FP-FFNN trained on a random split (*cf.* Figure 2d) of the **(a)** triazine sEH, **(b)** triazine SIRT2 dataset. Atoms contributing positively to enrichment are highlighted in green, and atoms contributing negatively to enrichment are highlighted in pink, with color intensity corresponding to the level of contribution to enrichment. “No” represents the DNA linker attachment point. Compound IDs (“cpd_id”) are sequential based on building block cycle numbers.

ures S30, S31, S32, S33), although the bottom 3 bits—corresponding to substructures most strongly contributing to *lower* enrichments—vary. This variance is unsurprising given that low enrichments are associated with low counts and higher uncertainty.

For the triazine sEH dataset, the top substructure (Figures S34, S35; Table S18) consists mostly of the triazine core (which is shared by all molecules in the dataset) with a methylated tertiary nitrogen. The tertiary nitrogen is also present in several of the other substructures with the highest weights. Lastly for the triazine SIRT2 dataset (Figures S36, S37; Table S19), the top five substructures correspond to the cyanothiazole in cycle-3 building block 67 (and equivalently cycle-2 building block 66).

In addition to analyzing the most important individual substructures, we also investigated contributions of pairs of substructures to model predictions (Figures S38, S40, S42, S44, S46, S39, S41, S43, S45, S47; Tables S20, S21, S22, S23, S24). Whereas enrichment of a single substructure indicates that one specific motif may be sufficient for high affinity, enrichment of a pair of substructures would indicate that a specific combination or arrangement of motifs may account for affinity. SAR for such combinations of structural motifs have previously been explored.^{39–41}

Multitask models show no significant difference in performance

We also investigated whether multitask modeling would result in improved model performance for the sEH and SIRT2 protein targets on the triazine dataset. Models’ output layers were extended to a dimension of two to simultaneously predict enrichment for both protein targets. One would expect improved model performance on the multitask setting *if* the factors that contribute to enrichment or lack thereof are similar across the tasks. Since sEH and SIRT2 both have hits from the triazine library, we explored training a model simultaneously on the two targets, for both a random split and a cycle-1+2+3 split (Table 1; Figure S12). There is no significant difference in model performance for the single task versus multitask models on either data split, suggesting that the chemical features responsible for affinity to

sEH and SIRT2 are distinct. Note that one could still consider extending this approach to a greater number of protein targets to assist in the prediction of *selective* enrichment.

Table 1: Test-set losses (mean \pm standard deviation) for single-task and multi-task NLL models on the triazine sEH and SIRT2 datasets. OH-FFNN and FP-FFNN results are averaged over five trials; D-MPNN results are averaged over three trials.

model	sEH			
	<i>random split</i>		<i>cycle-1+2+3 split</i>	
	single-task loss	multi-task loss	single-task loss	multi-task loss
OH-FFNN	0.5240 ± 0.0002	0.5236 ± 0.0005	0.5882 ± 0.0486	0.5884 ± 0.0491
FP-FFNN	0.5400 ± 0.0004	0.5398 ± 0.0004	0.6031 ± 0.0445	0.6045 ± 0.0435
D-MPNN	0.5390 ± 0.0006	0.5393 ± 0.0006	0.6155 ± 0.0598	0.6162 ± 0.0568
model	SIRT2			
	<i>random split</i>		<i>cycle-1+2+3 split</i>	
	single-task loss	multi-task loss	single-task loss	multi-task loss
OH-FFNN	0.4770 ± 0.0005	0.4770 ± 0.0007	0.5282 ± 0.0431	0.5270 ± 0.0441
FP-FFNN	0.4884 ± 0.0008	0.4886 ± 0.0007	0.5353 ± 0.0363	0.5368 ± 0.0351
D-MPNN	0.4882 ± 0.0007	0.4881 ± 0.0007	0.5388 ± 0.0521	0.5407 ± 0.0494

Discussion

Ability to smooth the response surface

To evaluate how the models handle the noise in the DEL data, we compared the distributions for the calculated enrichments and model-predicted enrichments on the DD1S CAIX dataset. It is well established that the main structural motif determining binding affinity to carbonic anhydrase is the presence of a benzenesulfonamide;^{27–29} compounds in DD1S with a benzenesulfonamide have very high affinity for the protein, whereas other compounds have comparatively low affinity. Compared to the calculated enrichments for the compounds in the dataset, we noticed better separation between the model-predicted enrichments for compounds with a benzenesulfonamide and compounds without a benzenesulfonamide (Figure 4b). This greater separation in enrichments shows that the models are able to act as structural regularizers and smooth noisy enrichment values for individual compounds. Such denoising of enrichments may improve the selection of compounds for follow-up investiga-

tion by enabling the detection of SAR patterns and reducing the number of false-positive compounds chosen solely based on count data.

Generalization performance

Quantitative performance (as measured by the NLL loss function) on the cycle splits is similar between the one-hot feed-forward networks, which by design cannot generalize, and the models using structure-based representations (*cf.* Figure 3). Therefore, the NLL metric alone does not reveal evidence of the models generalizing to new chemical structures. It has been noted³⁹ that the gain in generality with structure-based representations is accompanied by a loss of synthetic accessibility if the input representation is directly optimized to propose new molecular candidates; synthon-based descriptors (e.g., one-hot encoding of building blocks) denote a synthesis recipe, while generic fingerprints and other structure-based representations rely on abstract features that may warrant custom synthesis routes for corresponding products.

To confirm our models’ generalization performance, we analyzed the predictions of models trained on a cycle-1+2+3 split of the triazine sEH and triazine SIRT2 datasets, focusing on the test-set compounds that do not share a building block with *any* of the compounds in the training or validation sets. Due to structural symmetry in the triazine library, where a subset of cycle-2 building blocks are structurally identical to a cycle-3 building block and *vice versa*, in our analysis we excluded compounds with a test-set building block that is structurally identical to a training-set or validation-set building block. We did not observe high correlation between the predicted and calculated enrichments for these compounds with all building blocks uniquely in the test set, making it unclear whether the models are generalizing (Figures S48, S49). The one-hot feed-forward networks, which again cannot generalize, predict relatively similar values for all the molecules, as expected; the spread in the predicted enrichments is due to random weight initializations.

We also investigated the top predicted compounds for the fingerprint-based feed-forward

networks by comparing their atom-centered Gaussian visualizations for both the model generalizing on a cycle-1+2+3 split, and a corresponding model interpolating on a random split (Figures S53, S54). We did not observe much similarity in learned SAR between the cycle-1+2+3 split and random split models—this qualitative evaluation did not reveal evidence of the models extrapolating. We also noted that for a given model, the coloring of the same building block in the atom-centered Gaussian visualizations of different molecules may differ. This disparity may be explained by the fact that the atom-level weights used to generate the atom-centered Gaussian visualizations are normalized on a per-molecule basis, as opposed to being normalized across the entire dataset.

Domain of applicability and chemical diversity

Any QSAR model’s domain of applicability will depend on the diversity of the compounds in the training data. The triazine library we used contains all combinations of 78 building blocks for cycle 1, 290 building blocks for cycle 2, and 250 building blocks for cycle 3, attached to a common triazine core. These compounds may not cover enough chemical space for the models to generalize to new scaffolds, particularly those not containing the triazine core. In particular, the models’ domain of applicability is likely limited compared to that of the models built by McCloskey et al., which were trained on 31 to 42 pooled libraries with more extensive coverage of chemical space and successfully generalized to new structures as confirmed experimentally.⁷ UMAP projections (Figure 8; Methods) of both of the libraries we used (DOS-DEL-1 and the triazine library) and of a random sample of 600,000 compounds from PubChem show that our datasets cover relatively localized areas of chemical space, with relatively sparse coverage compared to compounds in PubChem. This sparse chemical coverage suggests that our models would likely have trouble generalizing to compounds dissimilar to those in these DELs. Further, little chemical similarity was found between compounds in the Enamine compound collections (REAL database and screening collection) and the top five compounds (by lower bound of calculated enrichment) in the

DD1S CAIX dataset, likely because commercially available compounds lack the scaffolds used in DOS-DEL-1 (Table S25).

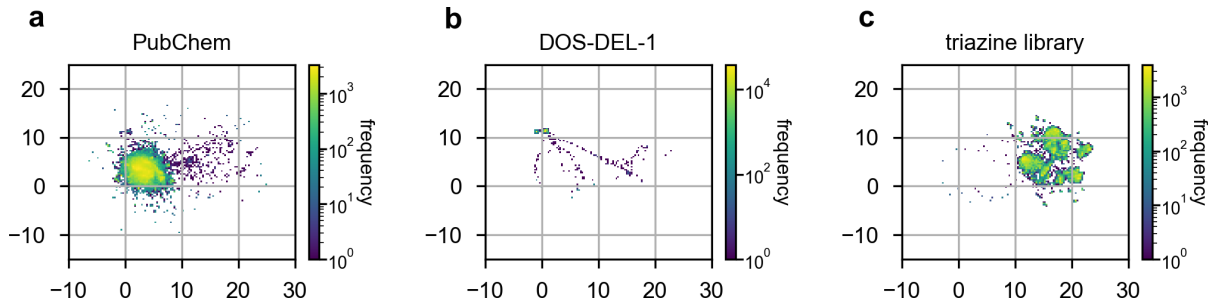


Figure 8: UMAP projection for (a) a random sample of 600k compounds from PubChem, (b) DOS-DEL-1, and (c) a random sample of 10% of the compounds in the triazine library. The UMAP embedding was fit to all three sets of compounds (using a random 10% of the compounds in DOS-DEL-1) simultaneously (*cf.* Methods). The coordinates of each plot represent the two dimensions to which the molecular fingerprints were projected.

Generality of the loss function

Using a NLL loss function is a general way to train a regression model in a maximum likelihood setting. As such, we expect our approach to apply to modeling on other sparse or noisy datasets where the stochasticity is known or can be modeled; in our case, we model the stochasticity of the DEL data using Poisson distributions. The Poisson enrichment ratio metric is relevant to other settings that compare sequencing count data between two experimental conditions (e.g., a treatment condition versus a control condition), and it admits extension across multiple off-target controls using comparison metrics based on multiple Poisson ratio test values and confidence intervals. Moreover, it can be used at multiple levels of resolution (e.g., mono-, di-, and tri-synthons) which suggests opportunities for combining synthetic history-based analyses with structure-based cheminformatics. We acknowledge that this is an active area of investigation,^{7,42} including a graph neural network (GNN)-based regression model to predict enrichment scores in noisy data accounting for confounding factors.⁴² In the context of DELs, we expect our modeling approach to be especially useful when learning from selection data for larger libraries with higher levels of noise due to low

sequencing coverage relative to the size of the library.

Conclusion

Our use of a Poisson enrichment ratio loss function to train enrichment-predicting regression models on DEL data for individual compounds introduces a novel approach to QSAR modeling on DEL data. Training to optimize the uncertainty-aware NLL directly leads to improved performance over a MSE loss as measured by the consistency between the model and data. Analysis of model predictions on the DD1S CAIX dataset, in the context of known SAR for carbonic anhydrase, shows that these models can act as structural regularizers and smooth noisy enrichment values for individual compounds in a DEL, which may reduce the risk of selecting a false-positive trisynthon based solely on its count data. However, based on a comparison of quantitative performance across the NLL model types, the calculated and predicted enrichments for compounds with chemical building blocks not used to train the models, and visualizations of learned SAR for the fingerprint-based feed-forward networks, it is unclear whether the models are generalizing. Nevertheless, the visualization procedure does reveal the substructures the model relies on for making its predictions and allows for a retrospective analysis of SAR trends without requiring monosynthon or disynthon aggregation. Additionally, it is possible that the lack of apparent generalization ability is a limitation of the data (i.e., the sparse chemical coverage of the libraries used to train the models) as opposed to the methods.

Further work can be done to explore more model types, more datasets, and other ways of improving model training (including pretraining). One of the more interesting extensions would be to connect to off-DNA affinity data by determining dissociation constants of the top predicted molecules from our models. Although this study does not include any off-DNA affinity data or experimental validation, on-DNA activity is already presumed to have some correlation (albeit noisy) with off-DNA activity based on previous successes in

hit finding.^{43–46} Another extension might include treating model predictions themselves as uncertain.⁴⁷ This modification would require a different loss function, since log likelihood calculation assumes that the enrichment is a fixed but unknown parameter, and that the data are what are stochastic (i.e., a frequentist view).

In summary, this work builds upon that of McCloskey et al., which demonstrates that binary classification of aggregated disynthons can identify diverse, drug-like hits with micromolar activity.⁷ We provide a proof of concept for an alternate approach applying regression modeling with a NLL loss function to individual compounds of a DEL, and anticipate that such an approach may prove useful for future work in this emerging field of machine learning on DEL data to improve the selection of compounds for follow-up investigation.

Methods

Problem formulation: regression

In our approach to QSAR modeling on DEL data, we treated learning DEL enrichments as a regression task of predicting enrichments of individual compounds. More specifically, the enrichment we predicted for each molecule is the ratio of the relative abundance of the DNA barcode for that molecule in the condition with the POI to the relative abundance of the barcode in the beads-only control. This enrichment served as a proxy measure of the molecule’s affinity for the protein of interest. Such a regression approach to modeling with DEL data had not been done before, likely due to the fact that DEL data is generally noisy and sparse, with high uncertainty in enrichments calculated for individual compounds. Usually when training regression models, the MSE is used, but this loss function does not consider uncertainty in the training data. As such, the MSE loss function is not appropriate for modeling with DEL data.

Problem formulation: loss function

Our regression modeling approach uses an uncertainty-aware NLL loss function. Uncertainty in DEL data arises in part from the stochastic nature of the sequencing step in the DEL experimental workflow, which we accounted for by modeling sequencing as random sampling (of DNA barcodes to be ligated onto the oligos bound to the chip) without replacement. Since there is an excess of DNA post-amplification relative to the number of measured sequencing reads (i.e., the number of sampled barcodes), we approximated sampling without replacement as sampling with replacement, yielding a binomial distribution that in the limit of low probabilities can be closely approximated by a Poisson distribution.²² In the regime of DEL data, where the total number of sequencing reads is large and the relative abundances of individual DNA barcodes are small, the probability mass functions of the Poisson and binomial distributions are nearly identical.

Modeling barcode count distributions as Poisson distributions allows us to use a Poisson ratio test to evaluate the consistency of the barcode counts observed in a DEL experiment with a hypothesized enrichment ratio, R . To perform the ratio test, we compared two known counts (k_1, k_2) from two experiments (one with the POI, one with beads only) with different total counts (n_1, n_2) drawn from two unknown Poisson distributions (described by λ_1, λ_2) using the following hypothesis test:

$$\text{null hypothesis: } H_0 = \frac{\lambda_1}{\lambda_2} \leq R_0$$

$$\text{alternate hypothesis: } H_1 = \frac{\lambda_1}{\lambda_2} > R_0$$

where R_0 is an enrichment threshold that we can freely specify for the purposes of hypothesis testing. Based on a variance stabilizing square root transformation⁴⁸, we can calculate a

z -score as:

$$z = 2 \frac{\sqrt{k_1 + \frac{3}{8}} - \sqrt{\left(\frac{n_1}{n_2} R_0\right) \left(k_2 + \frac{3}{8}\right)}}{\sqrt{1 + \left(\frac{n_1}{n_2} R_0\right)}} \sim N(0, 1)$$

In practice, we convert this calculation to a probability score for a two-sided alternate hypothesis, following Gu et al.:

$$p(k_1, k_2 | n_1, n_2, R_0 = R) \propto 1 - \phi(|z|)$$

where ϕ is the standard normal cumulative distribution function. Finally, we defined the loss function as the negative log likelihood of the probability that we would fail to reject the null hypothesis given the observed data:

$$\text{Loss}(R) = -\log p(k_1, k_2 | n_1, n_2, R_0 = R)$$

This loss function’s treatment of uncertainty in the training data is illustrated in plots of the NLL as a function of predicted enrichment for various theoretical count values (Figure S1). Note that with this loss function, the model will learn to predict a value of R given a molecular structure and will not separately predict λ_1 and λ_2 . The total counts (n_1, n_2) are calculated as the sum of all observed counts *after* any deduplication or thresholding based on UMI abundances.

Problem formulation: calculation of enrichment

We can invert the problem and solve for the R_0 for various values of z , roughly corresponding to different levels of confidence. Here we used $z = -2$ for the lower bound of calculated enrichment, $z = 0$ for the maximum likelihood calculated enrichment, and $z = 2$ for the upper bound of calculated enrichment.

Baseline formulation

Five different baselines were implemented: (a) one-hot encoded feed-forward networks, (b) point prediction (“pt”) models, (c) k-nearest-neighbors (KNN) regression models, (d) random models, and (e) binary classifiers.

The one-hot encoded feed-forward networks are incapable of generalization, and were thus used as one way of evaluating the extrapolative abilities of the models using structure-based representations.

The point prediction (“pt”) models were trained using the MSE loss function and a point estimate of the calculated enrichment, without treatment of uncertainty. These models were used to evaluate whether there is a benefit (as measured by NLL) to using an uncertainty-aware loss function during training.

Two types of random models were implemented: one with all predicted enrichments of test-set compounds set to 1 (“predict all ones”), and one where the predictions of a FP-FFNN on the same data split were randomly shuffled (“shuffle predictions”).

The binary classifiers were trained on random splits of the data, using binary cross entropy (BCE) loss and a fixed threshold for enrichment; we defined the top 0.5% and 0.01% of compounds in the training set to be enriched for the DD1S CAIX and triazine library datasets, respectively. This baseline was included to evaluate whether regression modeling yields any benefit to model performance (as measured by PR / ROC AUC) over a binary classification approach.

Models and representations tested

We used three different molecule representations (one-hot encoding, Morgan circular fingerprints,²⁵ and molecular graphs) and two model types (feed-forward neural networks and directed message-passing networks²⁶). The one-hot and fingerprint-based feed-forward neural networks are abbreviated as OH-FFNN and FP-FFNN respectively, and the graph-based directed message-passing neural networks are abbreviated as D-MPNN. RDKit⁴⁹ was used

to generate the Morgan circular fingerprints, using 2048 bits and a radius of 3. To generate a fingerprint for each molecule, atomic neighborhoods of radius 0 to 3 centered at each atom in the molecule were hashed to integer identifiers, which were then hashed to 2048 bits to produce the molecular fingerprint as a bit vector. PyTorch was used to build the models, and the Chemprop²⁶ package was specifically used to build the directed message-passing networks. We note that this study is not meant to be an exhaustive exploration of representations and model architectures.

Hyperparameter optimization

To evaluate and compare model performance for different representations, model types, and loss functions, we performed hyperparameter optimization via the Optuna Python package, using loss on the validation set as the objective function. From each run of optimization, we took the performance (as measured by NLL, MSE, rank correlation coefficient, PR AUC, or ROC AUC) of the model with the lowest validation loss. In particular for the FFNNs, we optimized each model’s dropout rate, hidden layer sizes, and initial learning rate (Table S2). For the D-MPNNs, we optimized the dropout rate, hidden layer size, number of message-passing steps, number of feed-forward layers, and initial learning rate (Table S3; Figures S8, S9; *cf.* Supporting Information). For the KNN baseline models, we optimized each model’s number of nearest neighbors, k (Table S2; Figure S10).

Data

Two DEL datasets were used for model training and evaluation. The first is from a screen of DOS-DEL-1 (DD1S), which contains 108,528 compounds and is a resynthesis of the library from Gerry et al.,²⁷ with carbonic anhydrase IX (CAIX) as the protein target. The primary structural motif driving enrichment in this dataset is well established in the literature: compounds with a benzenesulfonamide have very high affinity for carbonic anhydrase, whereas other compounds have comparatively low affinity.^{27–29} As such, this dataset was mainly used

as a tool to understand what the models were learning and to validate our analyses. While modeled after the experiment in Gerry et al., this dataset has not been previously published.

The second dataset is from a screen of a triazine library of 5,655,000 compounds, modeled after Clark et al.’s DEL-A,³ with the protein targets sEH and SIRT2, both of which have enriched compounds belonging to the triazine library. This experiment and dataset have not been previously published.

Each combination of building blocks within a library was assigned a unique integer compound ID (“cpd_id”) for tracking. Further details on the synthesis and screening of the DELs are provided below.

DEL synthesis

DOS-DEL-1²⁷ and the triazine library³ were synthesized following the previously reported conditions. The eight cycle-1 building blocks (i.e., scaffolds) used in DOS-DEL-1 were prepared according to the reported methods,^{27,50} and the remainder of the building blocks for DOS-DEL-1 and the triazine library were sourced from commercial vendors and used without further purification. The DNA “headpiece” (Figure S2) and DNA cycle tags (Figure S4) were purchased as custom orders from LGC Biosearch Technologies as lyophilized powders with all 5’ ends phosphorylated, and the double-stranded oligonucleotides containing primer-binding sites (Figure S3) were purchased as custom orders from IDT as lyophilized powders with all 5’ ends phosphorylated. For both libraries, the DNA headpiece was additionally extended using Fmoc-15-amino-4,7,10,13-tetraoxapentadecanoic acid, the “AOP linker.”

DOS-DEL-1 was synthesized according to protocols adapted from previously reported conditions²⁷ (modifications detailed below). Following each synthesis step, the material was purified by ethanol precipitation and reverse-phase ISCO (RediSep Rf Gold C18 columns) rather than semi-preparative reverse-phase HPLC. The cycle-4 tag (i.e., library identifier) and closing primer (Figures S5, S6) were installed in a single ligation step rather than two separate steps. Following ligation of the cycle-4 tag and closing primer, the final screening

construct was additionally purified using the Model 491 prep cell (Bio-Rad).

The triazine library was synthesized according to protocols adapted from previously reported conditions for “DEL-A”³ (modifications detailed below). The library was constructed using a set of 78 Fmoc-amino acids as the cycle-1 building blocks, 290 amines as the cycle-2 building blocks, and 250 amines as the cycle-3 building blocks; these building blocks differed from those used by Clark et al..³ Following ligation of the cycle-4 tag and closing primer, the final screening construct was purified using the Model 491 prep cell (Bio-Rad).

DEL affinity selection and sequencing

Preparation of protein and library were performed on ice and all other steps were performed at room temperature unless otherwise indicated. Affinity selection was carried out with a KingFisher Duo Prime (ThermoFisher Scientific). CAIX (R&D Systems 2188-CA-010), sEH (Cayman Chemical 10011669-50), and SIRT2 (Cayman Chemical 20011191-100) were purchased from commercial vendors. Each protein was screened in duplicate. Buffers used are as follows: B Buffer [25 mM HEPES pH 7.4, 150 mM NaCl, 0.05% Tween-20 (w/v)] and S Buffer [25 mM HEPES pH 7.4, 150 mM NaCl, 0.05% Tween-20 (w/v), 0.3 mg/mL Ultrapure Salmon Sperm DNA (ThermoFisher Scientific 15632011)]. Dynabeads™ MyOne™ Streptavidin C1 (ThermoFisher Scientific 65001) were washed three times with B buffer before protein immobilization. 40 μ L of beads were used for each sample. A Tris-NTA biotin adapter (Sigma 75543) was used (231 ng per sample) to immobilize the His-tagged proteins. Six molar equivalents of NiCl₂ were added to the adapter and incubated for 5 min. This solution was added to the strep beads agitated for 15 min; then the beads were washed three times with B buffer. Each protein (100 μ L, 111 pmol, 1.11 μ M) was immobilized (1 h, medium mix) and then washed twice with 200 μ L B Buffer before DEL addition. 1 million copies of each library member were diluted in S Buffer and were added to the immobilized protein and incubated (60 min, medium mix). The DEL-protein mixture was washed once with S Buffer (200 μ L, 3 min, medium mix) and twice with B Buffer (200 μ L, 3 min, medium

mix) before heat elution in B Buffer (100 μ L, 10 min, 90 °C). 20 μ L of each elution was restriction digested with *Stu*I (NEB R0187) (2 h, 37 °C) and cleaned up using ChargeSwitch PCR Clean-Up Kit (ThermoFisher Scientific CS12000). $\sim 4 \times 10^8$ molecules of DNA (19 μ L) were used for PCR reactions that contained 25 μ L of Invitrogen Platinum™ Hot Start PCR Master Mix (2X) (Invitrogen 13000012), 3 μ L i5 index primer (10 μ M stock) and 3 μ L i7 index primer (10 μ M stock concentration). The PCR method is as follows: 95 °C for 2 min; [20 cycles of 95 °C (15 s), 55 °C (15 s), 72 °C (30 s)]; 72 °C for 7 min; hold at 4 °C. PCR products were cleaned up with ChargeSwitch PCR Clean-Up Kit, pooled in equimolar amounts, and the 187 bp amplicon was gel purified using a 2% E-Gel™ EX Agarose Gels (ThermoFisher Scientific G401002) and QIAquick Gel Extraction Kit (Qiagen 28704). DNA concentration was obtained using the Qubit dsDNA BR assay kit and sequenced using a HiSeq SBS v4 50 cycle kit (Illumina FC-401-4002) and HiSeq SR Cluster Kit v4 (Illumina GD-401-4001) on a HiSeq 2500 instrument (Illumina) in a single 50-base read with custom primer CTTAGCTCCCAGCGACCTGCTTCAATGTCGGATAGTG and 8-base index read using custom primer CTGATGGAGGTAGAAGCCGCAGTGAGCATGGT.

Data processing

Reads observed during sequencing were processed into counts for each barcoded small molecule through a custom Python script. Inexact matches were allowed for each of the cycle-1, cycle-2, cycle-3, and library tags if observed sequences could be matched unambiguously to the most likely expected sequence. For DOS-DEL-1, up to 1 error was allowed in the cycle-1 tag and up to 2 errors in the library tag. For the triazine library, up to 1 error was allowed in the library tag. Unique molecular identifiers (UMIs) were used to de-duplicate reads using the directed graph approach implemented in the `umi_tools` package.⁵¹ Due to the high sequencing depth of DOS-DEL-1 relative to the size of the library, a minimum read threshold (minimum number of reads per UMI) of 5 was imposed to prevent counts from being inflated by erroneous reads or PCR errors in the UMI region that were not identified through the

directed graph approach (Figure S7).

Data splits

Table 2: Sizes of the training, validation, and test sets for each data split on the DD1S CAIX and triazine library datasets.

dataset	data split	training set size	validation set size	test set size
DD1S	random	75969	10853	21706
	cycle 1	67830	13566	27132
	cycle 2	75208	11424	21896
	cycle 3	75696	10944	21888
	cycle 1+2	47005	17969	43554
	cycle 1+3	47310	17670	43548
	cycle 2+3	52456	16704	39368
	cycle 1+2+3	32785	19085	56658
triazine	random	3958499	565501	1131000
	cycle 1	3915000	580000	1160000
	cycle 2	3958500	565500	1131000
	cycle 3	3958500	565500	1131000
	cycle 1+2	2740500	855500	2059000
	cycle 1+3	2740500	855500	2059000
	cycle 2+3	2770950	848250	2035800
	cycle 1+2+3	1918350	958450	2778200

To split the data into training, validation, and test sets, we used both random splits and various cycle splits (Figure 2d; Table 2). Random splits involved a 70%/10%/20% partitioning of the data into train/validation/test. For the cycle splits, we randomly split the building-block IDs for different cycles into training, validation, and test sets (again using a 70%/10%/20% split for each set of cycle building blocks). For each cycle split along one cycle A , the compounds in the dataset were randomly split by their cycle- A building-block ID into training, validation, and test sets. For each cycle split along two cycles A and B , the cycle- A and cycle- B building-block IDs were each split into training, validation, and test sets. Compounds with a building-block ID in at least one of the two test building-block ID sets made up the final test set; compounds that did not have a test-set building-block ID but did have a validation-set building-block ID made up the final validation set; all remaining

compounds made up the final training set. Similarly for cycle split along all three cycles, the compounds were first split separately by cycle-1, cycle-2, and cycle-3 building-block IDs into training, validation, and test sets. The union of the three test sets was the final test set; the union of the three validation sets minus the test set was the final validation set; all remaining compounds went to the final training set. All possible (unordered) combinations of cycles were used for the cycle splits, for a total of seven different cycle splits. We note that for these splits, building blocks were distinguished by ID rather than structure.

Quantitative evaluation metrics

We evaluated the performance of the regression models using the NLL loss of the test set, to match the loss function of the experimental NLL models. For the baseline point prediction (pt) models, the point value of enrichment was used to calculate loss during training. For completeness, we also evaluated the models using the MSE loss and rank correlation coefficient when treating the calculated enrichment as a precise measurement, although we believe the NLL loss is still the more relevant metric due to the stochastic nature of how sequencing data are obtained.

For the baseline binary classifiers and regression models evaluated as classifiers (using a fixed threshold for enrichment), we evaluated model performance using the PR AUC and ROC AUC of the test set. Since with DEL data we are typically interested only in the top predicted compounds in highly imbalanced datasets, PR AUC is the more relevant metric.

Disynthon analysis

To investigate whether the coarse correlation between predicted and calculated enrichments for the triazine sEH and triazine SIRT2 datasets (Figure 5ac) may be attributed to the noisiness of the data, we compared the predicted and calculated enrichments of aggregated disynthons on the same datasets (Figure 5bd). For each disynthon, the calculated enrichment was obtained using the summed counts for all constituent trisynthons. The predicted disyn-

thon enrichment was a simple average of all constituent trisynthons’ predicted enrichments. This simple average provides a qualitative understanding of enrichment; for future work, we note that for a more accurate measure of enrichment, the average should be weighted to correct for the non-uniform baseline abundances of the compounds, which affect the disynthon enrichment calculated by pooling counts. For example, consider the theoretical case of a disynthon that has two constituent trisynthons with counts (POI, beads only) of (4, 1) and (16, 2), which give maximum likelihood enrichment ratios of 4 and 8, respectively. Pooling the trisynthon counts gives a disynthon enrichment of $20/3 \approx 6.67$. Taking a simple average of the individual estimates of trisynthon enrichments, however, results in a different disynthon enrichment of 6.

Visualization

The first approach we used to visualize learned SAR was through atom-centered Gaussian visualizations (Figure 6a). These visualizations were generated by first calculating a weight for each atom in the molecule. The bits of the molecular fingerprint corresponding to the atom and the atomic neighborhoods (with radius up to 3) centered at that atom were masked, and the model’s prediction on the masked fingerprint was subtracted from the model’s prediction on the original fingerprint. The weights were then normalized by dividing by the absolute value of the weight with the greatest magnitude. Finally, these normalized weights were used to calculate atom-centered Gaussian distributions and generate a map of the molecule indicating which parts of the molecule contribute positively or negatively to enrichment.

The second approach we explored for visualization was calculating bit and substructure importance (Figure 6b). To do this, we first calculated a weight for each of the 2048 fingerprint bits, corresponding to the bit’s contribution to model predictions. We note that there were fingerprint bit collisions where multiple substructures were mapped to the same bit; to quantify the contribution of each specific substructure, even among substructures mapped to the same bit, we calculated substructure weights in addition to bit weights. To calculate each

bit weight, we first computed molecule-level weights—for each molecular fingerprint with the bit, we took the model’s prediction on the original fingerprint, and subtracted the model’s prediction on the same fingerprint but with the bit masked. We averaged these molecule-level weights to get the final bit weight. Afterwards, we analyzed the substructures mapped to the 5 bits with the highest weights (to investigate positive SAR) and the 3 bits with the lowest weights (to investigate negative SAR). More specifically, we calculated a weight for each substructure (corresponding to the substructure’s contribution to model predictions) by averaging the molecule-level weights corresponding to molecules with the substructure.

UMAP details

We trained a UMAP embedding on 4096-bit radius-3 Morgan circular fingerprints of a combination of 600k compounds randomly sampled from PubChem, a random 10% of DOS-DEL-1, and a random 10% of the triazine library. We increased the number of fingerprint bits from 2048 (as used for the QSAR models) to 4096 in order to reduce bit collisions and thus encode more structural information in the fingerprints. The trained embedding was applied separately to each of the three libraries, i.e., the 600k PubChem compounds used for training, all compounds in DOS-DEL-1, and the subset of the triazine library used for training (Figure 8). As for UMAP parameters, the `metric` parameter was set to ‘jaccard’ since we were using bit-based fingerprints. Otherwise, default UMAP parameters (`n_neighbors=15`, `min_dist=0.1`, `n_components=2`) were used without tuning.

Acknowledgement

This work has been funded in part through the National Institute of General Medical Sciences (R35GM127045 awarded to S.L.S.) and the NIBR Scholar’s Program (co-led by Karin Briner, Fred Zicri, Cindy Hon, and Stuart Schreiber) and we are grateful to Stuart Schreiber for his support of this work. KSL thanks the MIT UROP Office for additional funding support.

We thank Alicia Lindeman (Novartis) for performing the next-generation sequencing. We thank the GCP research credits program for supporting the computational costs of this work run on Google Cloud Platform. The authors acknowledge the MIT SuperCloud and Lincoln Laboratory Supercomputing Center for providing HPC resources that have contributed to the research results reported within this paper.

Data and Software Availability

All code, data, and tabulated results used in this study can be found at https://github.com/coleygroup/del_qsar.

Supporting Information Available

The Supporting Information contains additional methods relating to construction of the NLL loss function, calculation of bit and substructure importance for SAR visualization with substructure pairs, and further details of the DELs, hyperparameter optimization, and data processing for the DD1S CAIX dataset. We also include results relating to further comparisons of model performance on both scaffold-based and random splits of the data, and we provide tables with all raw performance numbers which appear in the charts in this paper. In addition, we analyze the class balance of classification datasets, analyze outliers and compare DD1S compounds to on-demand libraries, and provide further visualizations and a list of the RDKit calculated features used by our models.

References

- (1) Schreiber, S. L. A Chemical Biology View of Bioactive Small Molecules and a Binder-Based Approach to Connect Biology to Precision Medicines. *Isr. J. Chem.* **2019**, *59*, 52–59.

- (2) Imming, P.; Sinning, C.; Meyer, A. Drugs, their targets and the nature and number of drug targets. *Nat. Rev. Drug Discovery* **2006**, *5*, 821–834.
- (3) Clark, M. A.; Acharya, R. A.; Arico-Muendel, C. C.; Belyanskaya, S. L.; Benjamin, D. R.; Carlson, N. R.; Centrella, P. A.; Chiu, C. H.; Creaser, S. P.; Cuzzo, J. W.; Davie, C. P.; Ding, Y.; Franklin, G. J.; Franzen, K. D.; Geftter, M. L.; Hale, S. P.; Hansen, N. J. V.; Israel, D. I.; Jiang, J.; Kavarana, M. J.; Kelley, M. S.; Kollmann, C. S.; Li, F.; Lind, K.; Mataruse, S.; Medeiros, P. F.; Messer, J. A.; Myers, P.; O’Keefe, H.; Oliff, M. C.; Rise, C. E.; Satz, A. L.; Skinner, S. R.; Svendsen, J. L.; Tang, L.; van Vloten, K.; Wagner, R. W.; Yao, G.; Zhao, B.; Morgan, B. A. Design, synthesis and selection of DNA-encoded small-molecule libraries. *Nat. Chem. Biol.* **2009**, *5*, 647–654.
- (4) Kleiner, R. E.; Dumelin, C. E.; Liu, D. R. Small-molecule discovery from DNA-encoded chemical libraries. *Chem. Soc. Rev.* **2011**, *40*, 5707–5717.
- (5) Goodnow, R. A.; Dumelin, C. E.; Keefe, A. D. DNA-encoded chemistry: enabling the deeper sampling of chemical space. *Nat. Rev. Drug Discovery* **2017**, *16*, 131–147.
- (6) Flood, D. T.; Kingston, C.; Vantourout, J. C.; Dawson, P. E.; Baran, P. S. DNA Encoded Libraries: A Visitor’s Guide. *Isr. J. Chem.* **2020**, *60*, 268–280.
- (7) McCloskey, K.; Sigel, E. A.; Kearnes, S.; Xue, L.; Tian, X.; Moccia, D.; Gikunju, D.; Bazzaz, S.; Chan, B.; Clark, M. A.; Cuzzo, J. W.; Guié, M.-A.; Guiling, J. P.; Huguet, C.; Hupp, C. D.; Keefe, A. D.; Mulhern, C. J.; Zhang, Y.; Riley, P. Machine Learning on DNA-Encoded Libraries: A New Paradigm for Hit Finding. *J. Med. Chem.* **2020**, *63*, 8857–8866.
- (8) Franzini, R. M.; Ekblad, T.; Zhong, N.; Wichert, M.; Decurtins, W.; Nauer, A.; Zimmermann, M.; Samain, F.; Scheuermann, J.; Brown, P. J.; Hall, J.; Gräslund, S.; Schüler, H.; Neri, D. Identification of Structure–Activity Relationships from Screen-

- ing a Structurally Compact DNA-Encoded Chemical Library. *Angew. Chem., Int. Ed.* **2015**, *54*, 3927–3931.
- (9) Denton, K. E.; Wang, S.; Gignac, M. C.; Milosevich, N.; Hof, F.; Dykhuizen, E. C.; Krusemark, C. J. Robustness of In Vitro Selection Assays of DNA-Encoded Peptidomimetic Ligands to CBX7 and CBX8. *SLAS Discovery* **2018**, *23*, 417–428.
- (10) Satz, A. L. DNA Encoded Library Selections and Insights Provided by Computational Simulations. *ACS Chem. Biol.* **2015**, *10*, 2237–2245.
- (11) Satz, A. L. Simulated Screens of DNA Encoded Libraries: The Potential Influence of Chemical Synthesis Fidelity on Interpretation of Structure–Activity Relationships. *ACS Comb. Sci.* **2016**, *18*, 415–424.
- (12) Satz, A. L.; Hochstrasser, R.; Petersen, A. C. Analysis of Current DNA Encoded Library Screening Data Indicates Higher False Negative Rates for Numerically Larger Libraries. *ACS Comb. Sci.* **2017**, *19*, 234–238.
- (13) Sannino, A.; Gabriele, E.; Bigatti, M.; Mulatto, S.; Piazzzi, J.; Scheuermann, J.; Neri, D.; Donckele, E. J.; Samain, F. Quantitative Assessment of Affinity Selection Performance by Using DNA-Encoded Chemical Libraries. *ChemBioChem* **2019**, *20*, 955–962.
- (14) Hall, J.; Foley, T. L.; Chen, Q.; Israel, D. I.; Xu, Y.; Ford, K. K.; Xie, P.; Fan, J.; Wan, J. A simple method for determining compound affinity and chemical yield from DNA-encoded library selections. *Biochem. Biophys. Res. Commun.* **2020**, *527*, 250–256.
- (15) Foley, T. L.; Burchett, W.; Chen, Q.; Flanagan, M. E.; Kapinos, B.; Li, X.; Montgomery, J. I.; Ratnayake, A. S.; Zhu, H.; Peakman, M.-C. Selecting Approaches for Hit Identification and Increasing Options by Building the Efficient Discovery of Actionable Chemical Matter from DNA-Encoded Libraries. *SLAS Discovery* **2021**, *26*, 263–280.

- (16) Franzini, R. M.; Nauer, A.; Scheuermann, J.; Neri, D. Interrogating target-specificity by parallel screening of a DNA-encoded chemical library against closely related proteins. *Chem. Commun.* **2015**, *51*, 8014–8016.
- (17) Kung, P.-P.; Bingham, P.; Burke, B. J.; Chen, Q.; Cheng, X.; Deng, Y.-L.; Dou, D.; Feng, J.; Gallego, G. M.; Gehring, M. R.; Grant, S. K.; Greasley, S.; Harris, A. R.; Maegley, K. A.; Meier, J.; Meng, X.; Montano, J. L.; Morgan, B. A.; Naughton, B. S.; Palde, P. B.; Paul, T. A.; Richardson, P.; Sakata, S.; Shaginian, A.; Sonnenburg, W. K.; Subramanyam, C.; Timofeevski, S.; Wan, J.; Yan, W.; Stewart, A. E. Characterization of Specific *N* - α -Acetyltransferase 50 (Naa50) Inhibitors Identified Using a DNA Encoded Library. *ACS Med. Chem. Lett.* **2020**, *11*, 1175–1184.
- (18) Petersen, L. K.; Blakskjær, P.; Chaikuad, A.; Christensen, A. B.; Dietvorst, J.; Holmkvist, J.; Knapp, S.; Kořínek, M.; Larsen, L. K.; Pedersen, A. E.; Röhm, S.; Sløk, F. A.; Hansen, N. J. V. Novel p38 α MAP kinase inhibitors identified from yoc-toReactor DNA-encoded small molecule library. *MedChemComm* **2016**, *7*, 1332–1339.
- (19) Cherkasov, A.; Muratov, E. N.; Fourches, D.; Varnek, A.; Baskin, I. I.; Cronin, M.; Dearden, J.; Gramatica, P.; Martin, Y. C.; Todeschini, R.; Consonni, V.; Kuz'min, V. E.; Cramer, R.; Benigni, R.; Yang, C.; Rathman, J.; Terfloeth, L.; Gasteiger, J.; Richard, A.; Tropsha, A. QSAR Modeling: Where Have You Been? Where Are You Going To? *J. Med. Chem.* **2014**, *57*, 4977–5010.
- (20) Muratov, E. N.; Bajorath, J.; Sheridan, R. P.; Tetko, I. V.; Filimonov, D.; Poroikov, V.; Oprea, T. I.; Baskin, I. I.; Varnek, A.; Roitberg, A.; Isayev, O.; Curtalolo, S.; Fourches, D.; Cohen, Y.; Aspuru-Guzik, A.; Winkler, D. A.; Agrafiotis, D.; Cherkasov, A.; Tropsha, A. QSAR without Borders. *Chem. Soc. Rev.* **2020**, *49*, 3525–3564.
- (21) Bentley, D. R.; Balasubramanian, S.; Swerdlow, H. P.; Smith, G. P.; Milton, J.;

Brown, C. G.; Hall, K. P.; Evers, D. J.; Barnes, C. L.; Bignell, H. R.; Boutell, J. M.;
 Bryant, J.; Carter, R. J.; Keira Cheetham, R.; Cox, A. J.; Ellis, D. J.; Flatbush, M. R.;
 Gormley, N. A.; Humphray, S. J.; Irving, L. J.; Karbelashvili, M. S.; Kirk, S. M.; Li, H.;
 Liu, X.; Maisinger, K. S.; Murray, L. J.; Obradovic, B.; Ost, T.; Parkinson, M. L.;
 Pratt, M. R.; Rasolonjatovo, I. M. J.; Reed, M. T.; Rigatti, R.; Rodighiero, C.;
 Ross, M. T.; Sabot, A.; Sankar, S. V.; Scally, A.; Schroth, G. P.; Smith, M. E.;
 Smith, V. P.; Spiridou, A.; Torrance, P. E.; Tzonev, S. S.; Vermaas, E. H.; Wal-
 ter, K.; Wu, X.; Zhang, L.; Alam, M. D.; Anastasi, C.; Aniebo, I. C.; Bailey, D. M. D.;
 Bancarz, I. R.; Banerjee, S.; Barbour, S. G.; Baybayan, P. A.; Benoit, V. A.; Ben-
 son, K. F.; Bevis, C.; Black, P. J.; Boodhun, A.; Brennan, J. S.; Bridgham, J. A.;
 Brown, R. C.; Brown, A. A.; Buermann, D. H.; Bundu, A. A.; Burrows, J. C.;
 Carter, N. P.; Castillo, N.; Chiara E. Catenazzi, M.; Chang, S.; Neil Cooley, R.;
 Crake, N. R.; Dada, O. O.; Diakoumakos, K. D.; Dominguez-Fernandez, B.; Earn-
 shaw, D. J.; Egbujor, U. C.; Elmore, D. W.; Etchin, S. S.; Ewan, M. R.; Fedurco, M.;
 Fraser, L. J.; Fuentes Fajardo, K. V.; Scott Furey, W.; George, D.; Gietzen, K. J.; God-
 dard, C. P.; Golda, G. S.; Granieri, P. A.; Green, D. E.; Gustafson, D. L.; Hansen, N. F.;
 Harnish, K.; Haudenschild, C. D.; Heyer, N. I.; Hims, M. M.; Ho, J. T.; Horgan, A. M.;
 Hoschler, K.; Hurwitz, S.; Ivanov, D. V.; Johnson, M. Q.; James, T.; Huw Jones, T. A.;
 Kang, G.-D.; Kerelska, T. H.; Kersey, A. D.; Khrebtukova, I.; Kindwall, A. P.; Kings-
 bury, Z.; Kokko-Gonzales, P. I.; Kumar, A.; Laurent, M. A.; Lawley, C. T.; Lee, S. E.;
 Lee, X.; Liao, A. K.; Loch, J. A.; Lok, M.; Luo, S.; Mammen, R. M.; Martin, J. W.;
 McCauley, P. G.; McNitt, P.; Mehta, P.; Moon, K. W.; Mullens, J. W.; Newing-
 ton, T.; Ning, Z.; Ling Ng, B.; Novo, S. M.; O'Neill, M. J.; Osborne, M. A.; Os-
 nowski, A.; Ostadan, O.; Paraschos, L. L.; Pickering, L.; Pike, A. C.; Pike, A. C.;
 Chris Pinkard, D.; Pliskin, D. P.; Podhasky, J.; Quijano, V. J.; Raczy, C.; Rae, V. H.;
 Rawlings, S. R.; Chiva Rodriguez, A.; Roe, P. M.; Rogers, J.; Rogert Bacigalupo, M. C.;
 Romanov, N.; Romieu, A.; Roth, R. K.; Rourke, N. J.; Ruediger, S. T.; Rusman, E.;

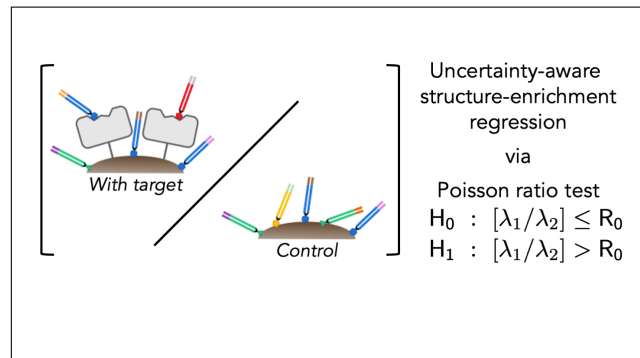
- Sanches-Kuiper, R. M.; Schenker, M. R.; Seoane, J. M.; Shaw, R. J.; Shiver, M. K.; Short, S. W.; Sizto, N. L.; Sluis, J. P.; Smith, M. A.; Ernest Sohna, J.; Spence, E. J.; Stevens, K.; Sutton, N.; Szajkowski, L.; Tregidgo, C. L.; Turcatti, G.; vandeVondele, S.; Verhovsky, Y.; Virk, S. M.; Wakelin, S.; Walcott, G. C.; Wang, J.; Worsley, G. J.; Yan, J.; Yau, L.; Zuerlein, M.; Rogers, J.; Mullikin, J. C.; Hurles, M. E.; McCooke, N. J.; West, J. S.; Oaks, F. L.; Lundberg, P. L.; Klennerman, D.; Durbin, R.; Smith, A. J. Accurate whole human genome sequencing using reversible terminator chemistry. *Nature* **2008**, *456*, 53–59.
- (22) Simons, G.; Johnson, N. L. On the Convergence of Binomial to Poisson Distributions. *Ann. Math. Stat.* **1971**, *42*, 1735–1736.
- (23) Kuai, L.; O’Keeffe, T.; Arico-Muendel, C. Randomness in DNA Encoded Library Selection Data Can Be Modeled for More Reliable Enrichment Calculation. *SLAS Discovery* **2018**, *23*, 405–416.
- (24) Wu, Z.; Ramsundar, B.; Feinberg, E.; Gomes, J.; Geniesse, C.; Pappu, A. S.; Leswing, K.; Pande, V. MoleculeNet: a benchmark for molecular machine learning. *Chem. Sci.* **2018**, *9*, 513–530.
- (25) Rogers, D.; Hahn, M. Extended-Connectivity Fingerprints. *J. Chem. Inf. Model.* **2010**, *50*, 742–754.
- (26) Yang, K.; Swanson, K.; Jin, W.; Coley, C.; Eiden, P.; Gao, H.; Guzman-Perez, A.; Hopper, T.; Kelley, B.; Mathea, M.; Palmer, A.; Settels, V.; Jaakkola, T.; Jensen, K.; Barzilay, R. Analyzing Learned Molecular Representations for Property Prediction. *J. Chem. Inf. Model.* **2019**, *59*, 3370–3388.
- (27) Gerry, C. J.; Wawer, M. J.; Clemons, P. A.; Schreiber, S. L. DNA Barcoding a Complete Matrix of Stereoisomeric Small Molecules. *J. Am. Chem. Soc.* **2019**, *141*, 10225–10235.

- (28) Li, Y.; De Luca, R.; Cazzamalli, S.; Pretto, F.; Bajic, D.; Scheuermann, J.; Neri, D. Versatile protein recognition by the encoded display of multiple chemical elements on a constant macrocyclic scaffold. *Nat. Chem.* **2018**, *10*, 441–448.
- (29) Buller, F.; Steiner, M.; Frey, K.; Mircsof, D.; Scheuermann, J.; Kalisch, M.; Bühlmann, P.; Supuran, C. T.; Neri, D. Selection of Carbonic Anhydrase IX Inhibitors from One Million DNA-Encoded Compounds. *ACS Chem. Biol.* **2011**, *6*, 336–344.
- (30) Deokar, H.; Deokar, M.; Wang, W.; Zhang, R.; Buolamwini, J. K. QSAR studies of new pyrido[3,4-b]indole derivatives as inhibitors of colon and pancreatic cancer cell proliferation. *Med. Chem. Res.* **2018**, *27*, 2466–2481.
- (31) Mahipal,; Prakash Tanwar, O.; Karthikeyan, C.; S. Hari Narayana Moorthy, N.; Trivedi, P. 3D QSAR of Aminophenyl Benzamide Derivatives as Histone Deacetylase Inhibitors. *Med. Chem.* **2010**, *6*, 277–285.
- (32) Gao, L.; Zu, M.; Wu, S.; Liu, A.-L.; Du, G.-H. 3D QSAR and docking study of flavone derivatives as potent inhibitors of influenza H1N1 virus neuraminidase. *Bioorganic Med. Chem. Lett.* **2011**, *21*, 5964–5970.
- (33) Alam, S.; Khan, F. 3D-QSAR studies on Maslinic acid analogs for Anticancer activity against Breast Cancer cell line MCF-7. *Sci. Rep.* **2017**, *7*, 6019.
- (34) Riniker, S.; Landrum, G. A. Similarity maps - a visualization strategy for molecular fingerprints and machine-learning methods. *J. Cheminf.* **2013**, *5*, 43.
- (35) Anandan, S.-K.; Webb, H. K.; Do, Z. N.; Gless, R. D. Unsymmetrical non-adamantyl N,N'-diaryl urea and amide inhibitors of soluble epoxide [sic] hydrolase. *Bioorganic Med. Chem. Lett.* **2009**, *19*, 4259–4263.
- (36) McElroy, N. R.; Jurs, P. C.; Morisseau, C.; Hammock, B. D. QSAR and Classification

- of Murine and Human Soluble Epoxide Hydrolase Inhibition by Urea-Like Compounds. *J. Med. Chem.* **2003**, *46*, 1066–1080.
- (37) Kramer, J. S.; Woltersdorf, S.; Dufloot, T.; Hiesinger, K.; Lillich, F. F.; Knöll, F.; Wittmann, S. K.; Klingler, F.-M.; Brunst, S.; Chaikuad, A.; Morisseau, C.; Hammock, B. D.; Buccellati, C.; Sala, A.; Rovati, G. E.; Leuillier, M.; Fraineau, S.; Rondeaux, J.; Hernandez-Olmos, V.; Heering, J.; Merk, D.; Pogoryelov, D.; Steinhilber, D.; Knapp, S.; Bellien, J.; Proschak, E. Discovery of the First in Vivo Active Inhibitors of the Soluble Epoxide Hydrolase Phosphatase Domain. *J. Med. Chem.* **2019**, *62*, 8443–8460.
- (38) Lee, K. S. S.; Liu, J.-Y.; Wagner, K. M.; Pakhomova, S.; Dong, H.; Morisseau, C.; Fu, S. H.; Yang, J.; Wang, P.; Ulu, A.; Mate, C. A.; Nguyen, L. V.; Hwang, S. H.; Edin, M. L.; Mara, A. A.; Wulff, H.; Newcomer, M. E.; Zeldin, D. C.; Hammock, B. D. Optimized Inhibitors of Soluble Epoxide Hydrolase Improve in Vitro Target Residence Time and in Vivo Efficacy. *J. Med. Chem.* **2014**, *57*, 7016–7030.
- (39) Wawer, M. J.; Jaramillo, D. E.; Dančák, V.; Fass, D. M.; Haggarty, S. J.; Shamji, A. F.; Wagner, B. K.; Schreiber, S. L.; Clemons, P. A. Automated Structure–Activity Relationship Mining: Connecting Chemical Structure to Biological Profiles. *J. Biomol. Screening* **2014**, *19*, 738–748.
- (40) Eberle, C.; Lauber, B. S.; Fankhauser, D.; Kaiser, M.; Brun, R.; Krauth-Siegel, R. L.; Diederich, F. Improved Inhibitors of Trypanothione Reductase by Combination of Motifs: Synthesis, Inhibitory Potency, Binding Mode, and Antiprotozoal Activities. *ChemMedChem* **2011**, *6*, 292–301.
- (41) Wassermann, A. M.; Bajorath, J. Directed R-Group Combination Graph: A Methodology To Uncover Structure–Activity Relationship Patterns in a Series of Analogues. *J. Med. Chem.* **2012**, *55*, 1215–1226.

- (42) Ma, R.; Dreiman, G. H. S.; Ruggiu, F.; Riesselman, A. J.; Liu, B.; James, K.; Sultan, M.; Koller, D. Regression modeling on DNA encoded libraries. <https://openreview.net/forum?id=rrcoPmV1XgN> **2021**,
- (43) Eidam, O.; L. Satz, A. Analysis of the productivity of DNA encoded libraries. *MedChemComm* **2016**, *7*, 1323–1331.
- (44) Arico-Muendel, C. C. From haystack to needle: finding value with DNA encoded library technology at GSK. *MedChemComm* **2016**, *7*, 1898–1909.
- (45) Favalli, N.; Bassi, G.; Scheuermann, J.; Neri, D. DNA-encoded chemical libraries - achievements and remaining challenges. *FEBS Lett.* **2018**, *592*, 2168–2180.
- (46) Kunig, V.; Potowski, M.; Gohla, A.; Brunschweiler, A. DNA-encoded libraries – an efficient small molecule discovery technology for the biomedical sciences. *Biol. Chem.* **2018**, *399*, 691–710.
- (47) Hirschfeld, L.; Swanson, K.; Yang, K.; Barzilay, R.; Coley, C. W. Uncertainty Quantification Using Neural Networks for Molecular Property Prediction. *J. Chem. Inf. Model.* **2020**, *60*, 3770–3780.
- (48) Gu, K.; Ng, H. K. T.; Tang, M. L.; Schucany, W. R. Testing the Ratio of Two Poisson Rates. *Biom. J.* **2008**, *50*, 283–298.
- (49) Landrum, G. A. RDKit: Open-source cheminformatics. <http://www.rdkit.org>, version 2020.03.2.
- (50) Verho, O.; Maetani, M.; Melillo, B.; Zoller, J.; Schreiber, S. L. Stereospecific Palladium-Catalyzed C-H Arylation of Pyroglutamic Acid Derivatives at the C3 Position Enabled by 8-Aminoquinoline as a Directing Group. *Org. Lett.* **2017**, *19*, 4424–4427.
- (51) Smith, T.; Heger, A.; Sudbery, I. UMI-tools: modeling sequencing errors in Unique Molecular Identifiers to improve quantification accuracy. *Genome Res.* *27*, 491–499.

Graphical TOC Entry



Supporting Information:

Machine learning on DNA-encoded library count data using an uncertainty-aware probabilistic loss function

Katherine S. Lim,^{†,‡} Andrew G. Reidenbach,[¶] Bruce K. Hua,^{§,¶} Jeremy W. Mason,^{¶,||} Christopher J. Gerry,^{§,¶} Paul A. Clemons,^{*,¶} and Connor W. Coley^{*,†,⊥,¶}

[†]*Department of Electrical Engineering and Computer Science, Massachusetts Institute of Technology, 77 Massachusetts Avenue, Cambridge, Massachusetts 02139, United States*

[‡]*Department of Biology, Massachusetts Institute of Technology, 77 Massachusetts Avenue, Cambridge, Massachusetts 02139, United States*

[¶]*Chemical Biology and Therapeutics Science Program, Broad Institute, 415 Main Street, Cambridge, Massachusetts 02142, United States*

[§]*Department of Chemistry and Chemical Biology, Harvard University, 12 Oxford Street, Cambridge, Massachusetts 02138, United States*

^{||}*Novartis Institutes for BioMedical Research, Cambridge, Massachusetts 02139, United States*

[⊥]*Department of Chemical Engineering, Massachusetts Institute of Technology, 77 Massachusetts Avenue, Cambridge, Massachusetts 02139, United States*

E-mail: pclemons@broadinstitute.org; ccoley@mit.edu

S1 Additional Methods

S1.1 NLL loss function

We assume that the counts for each barcode are distributed according to a Poisson distribution.^{S1} Poisson distributions are characterized by a single parameter λ that defines a rate of seeing a certain event under a continuous observation interval. Because the total number of counts is large ($n > 100,000$) and the number of counts for any individual barcode will be relatively small ($p < 0.01$), we approximate the counts/reads as a pseudo-continuous observation interval. The parameters describing the POI and beads-only distributions, λ_1 and λ_2 , are unknown. There is also some known ratio between these distributions, $R = \lambda_1/\lambda_2$. **This R is what we refer to as the enrichment ratio.**

With our k_1 counts from n_1 observations for the POI, we can estimate $\hat{\lambda}_1$ as k_1/n_1 —this is the most likely value of λ_1 given what we have observed, but it is unlikely to be exact. For example, if our true $\lambda_1 = 0.01$ and we have $n_1 = 1000$ observations, we would see $k_1 = 10$ *on average*; sometimes we'd see fewer counts, sometimes we'd see greater counts. The maximum likelihood estimates for λ_2 is similarly $\hat{\lambda}_2 = k_2/n_2$.

A naive enrichment metric could therefore be $\hat{R} = \hat{\lambda}_1/\hat{\lambda}_2$ —what is the ratio of the most likely values for these two Poisson distributions? This works okay most of the time, but does not take into account uncertainty well. Particularly in the low-count regime, things fall apart. If we observed $k_1 = 1$ in the experiment and $k_2 = 0$ in the beads-only, then we would estimate $\hat{R} = \infty$.

Instead of looking at the ratio of the most likely λ values for each population, we look at the most likely ratio of the λ values. The distinction is a little subtle, but the calculation and confidence intervals look quite different. Formally, we define a hypothesis test:

$$H_0 : \frac{\lambda_1}{\lambda_2} \leq R_0 \quad H_1 : \frac{\lambda_1}{\lambda_2} > R_0 \quad (1)$$

We would like to make an inference about the ratio between the true rates for the POI and beads-only case. Several metrics have been proposed for this test, but here we use one based on a variance stabilizing square root transformation.^{S2} We calculate a z -score as:

$$z = 2 \frac{\left(k_1 + \frac{3}{8}\right)^{1/2} - \left(k_2 + \frac{3}{8}\right)^{1/2} \left(\frac{n_1}{n_2} R_0\right)^{1/2}}{\left(1 + \frac{n_1}{n_2} R_0\right)^{1/2}} \quad (2)$$

This z should be normally distributed with a mean of 0 and variance of 1. Now, for specific values of R_0 , we can see what this ratio test will do.

Consider the simplifying case where $n_1 = n_2$ and we're testing $R_0 = 1$. The hypothesis test is therefore asking whether we believe the ratio between the true Poisson rates to be greater than $R_0 = 1$. Our z score simplifies to

$$z = \sqrt{2} \left(\left(k_1 + \frac{3}{8}\right)^{1/2} - \left(k_2 + \frac{3}{8}\right)^{1/2} \right) \quad n_1 = n_2, \quad R_0 = 1 \quad (3)$$

Clearly, if $k_1 = k_2$, we have no reason to believe that the true enrichment ratio is greater (or less) than one, so we will get $z = 0$. If we observe $k_1 > k_2$, we will start to believe there has been some enrichment ($z > 0$). The greater the discrepancy between k_1 and k_2 , the more significant this seems to be, and the more likely we will reject the null hypothesis.

We can finally invert the problem and solve for the R_0 for various values of z , roughly corresponding to different levels of confidence. Solving for $z = 0$ gives us the most likely enrichment ratio; we can calculate a confidence interval by solving for $z = \pm 2$.

As a toy example, consider a few cases where there seems to have been some enrichment. Take $n_1 = n_2 = 1,000,000$, and the following (k_1, k_2) values: (150, 50), (15, 5), and (3, 1). That is, we have a million total counts for the POI and beads-only experiments, and for a particular barcode, we have (POI, beads-only) counts of (150, 50), (15, 5), or (3, 1). The calculated R_0 for each of these cases is 2.99, 2.86, and 2.45, respectively, with confidence intervals of [2.18, 4.20], [1.13, 9.57], and [0.34, 119.00]. We can look at the negative-log likelihood (NLL) of failing to reject the null hypothesis that the true enrichment ratio is R , given k_1 , n_1 , k_2 , and n_2 , as a function of R (Figure S1).

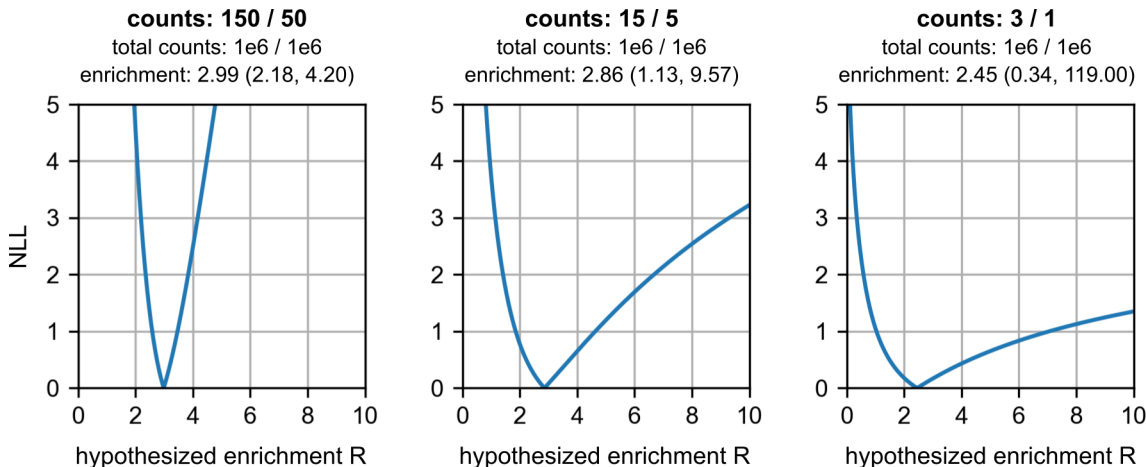


Figure S1: Plots of NLL as a function of predicted enrichment for various theoretical counts.

These plots demonstrate the NLL loss function’s treatment of uncertainty—with higher barcode counts, there is less uncertainty about the enrichment, and thus the loss function sharply penalizes model predictions that stray from the most likely enrichment. On the other hand, with lower barcode counts, there is greater uncertainty, so the loss function is more lenient and tolerates predictions within a wider plausible range around the most likely enrichment.

We note that the enrichment calculation itself (using the Poisson ratio test) can aggregate over different sets of synthon combinations (e.g., A, B, C, AB, BC, AC, ABC, where A/B/C are monosynthons, AB/BC/AC are disynthons, and ABC is a trisynthon). With the higher counts after aggregation, one would expect and observe reduced uncertainties. Whether this is a ‘better’ treatment or how one might use that information in the surrogate structure-enrichment model is not totally clear. Training on monosynthons alone would not achieve enough chemical diversity (for the DELs in this study, at least) to generalize beyond the ca. hundreds of structures. We could assemble disynthon structures as done by McCloskey et al. and train the regression model on all AB, BC, AC disynthons, but it may not make sense to combine trisynthons, disynthons, and monosynthons into a single surrogate model, particularly because the number of trisynthons far exceeds the number of disynthons or monosynthons in a typical library.

S1.2 Library sizes and total sequencing counts

Table S1: Library sizes and total counts.

dataset	number of compounds	total number of counts in experimental condition (with POI)	total number of counts in beads-only control
DD1S CAIX	108,528	638,831	5,208,230
triazine sEH	5,655,000	5,085,569	5,395,114
triazine SIRT2		3,497,768	

S1.3 Hyperparameter optimization

On the DD1S CAIX dataset, we performed 5 differently seeded runs of 100 iterations of Bayesian hyperparameter optimization (using loss on the validation set as the objective function) for each model type and data split type (random split and the various cycle splits for the regression models; just random split for the binary classifiers), using the Optuna Python package.

On the larger triazine sEH and triazine SIRT2 datasets, we reduced the hyperparameter search space and performed 5 differently seeded runs of 25 iterations of optimization for each FFNN and 4 iterations of optimization for representative D-MPNN(s), due to computational cost. For the binary classifiers, we used one representative D-MPNN for optimization; for the regression models, we used one experimental D-MPNN (trained using NLL) and one baseline D-MPNN pt model (trained using MSE), both on a random split of the data. Specifically for the FFNNs, we increased the smallest possible hidden layer size to ensure adequate model capacity, and decreased the range of values for the initial learning rate based on hyperparameter optimization results for the FFNNs on the DD1S CAIX dataset. For the representative D-MPNNs, we similarly decreased the range of values for the initial learning rate and fixed other hyperparameters based on results for the D-MPNNs on the DD1S CAIX dataset. We used the optimization results to fix the initial learning rate for the other D-MPNNs (separately for the NLL and pt regression models), and performed a total of 3 differently seeded runs of training and evaluation for the D-MPNNs on each data split type used (including the optimization runs for random split). The regression D-MPNNs trained using NLL on the triazine SIRT2 dataset were notably sensitive to the learning rate, and so we re-ran training and evaluation for these models at a lower fixed learning rate.

For the baseline KNN models, the number of neighbors (k) was optimized on the DD1S CAIX dataset.

Table S2: Ranges and value types for hyperparameter optimization on the DD1S CAIX dataset.

DD1S		range of values		
model	hyperparameter	lower bound	upper bound	value type
FFNN	initial learning rate	1e−5	1e−1	continuous (logarithmic scale)
	number of hidden layers	1	3	discrete (step size = 1)
	layer size architecture	N/A	N/A	categorical (flat, pyramid with factor of 2 or 4)
	largest hidden layer size	16	1024	discrete (base 2 logarithmic scale, step size = 1)
	dropout rate	0	0.5	discrete (step size = 0.05)
D-MPNN	initial learning rate	1e−5	2e−3	continuous (logarithmic scale)
	number of message-passing steps	2	6	discrete (step size = 1)
	number of FFN hidden layers	1	3	discrete (step size = 1)
	size of FFN hidden layers	300	2400	discrete (step size = 100)
	dropout rate	0	0.5	discrete (step size = 0.05)
KNN	number of nearest neighbors (k)	1	9	discrete (step size = 2)

Table S3: Ranges and value types for hyperparameter optimization on the triazine datasets.

triazine		range of values		
model	hyperparameter	lower bound	upper bound	value type
FFNN	initial learning rate	1e−5	3e−2	continuous (logarithmic scale)
	number of hidden layers	1	3	discrete (step size = 1)
	layer size architecture	N/A	N/A	categorical (flat, pyramid with factor of 2 or 4)
	smallest hidden layer size (largest possible is 1024)	64	1024	discrete (base 2 logarithmic scale, step size = 1)
	dropout rate	0	0.5	discrete (step size = 0.05)
D-MPNN (random split)	initial learning rate	1e−5	3e−4	categorical (1e−5, 3e−5, 1e−4, 3e−4)

S1.4 Bit and substructure importance

To ensure accurate counting of substructures, we used custom SMARTS patterns for the substructures. These are shown in tables in the Additional Results section.

S1.4.1 Substructure-pair analysis

In this analysis we investigated contributions of pairs of substructures to model predictions. To do this, we took the top substructure a (mapped to bit A) from the single-substructure analysis, and looked just at the molecules with that substructure. For each fingerprint bit B not corresponding to the top substructure, we calculated a bit weight by first calculating molecule-level weights (the model’s prediction on the original molecular fingerprint minus the model’s prediction on same fingerprint but with bits A and B masked). We then averaged over these molecule-level weights to get the final weight for the bit. Afterwards, we analyzed the substructures mapped to the 5 bits with the highest weights (to investigate positive SAR) and the 3 bits with the lowest weights (to investigate negative SAR). To do this, we calculated a weight for each substructure b of interest by averaging the molecule-level weights corresponding to the molecules that have both substructures a and b .

The results for each dataset are shown in the Additional Results section (Figures S38, S40, S42, S44, S46).

We note that since we only considered molecules with the top substructure a from the single-substructure analysis, not all substructures considered for a certain bit in the single-substructure analysis may be included for the same bit in this substructure-pair analysis. For instance, the middle substructure shown for bit 1785 in the DD1S CAIX (seed 1) single-substructure analysis (Figure S30) is not included for the same bit in the substructure-pair analysis on the same dataset (Figure S40), since that substructure corresponds to a cycle-3 building block, and the top substructure from the single-substructure analysis also corresponds to a cycle-3 building block.

We also note that because a given building block or moiety has many atomic neighborhoods of radius 0 to 3, some of the top bits for this analysis may correspond to other atomic neighborhoods of the same moiety that the top substructure corresponds to (e.g., a benzenesulfonamide for the DD1S CAIX dataset).

S1.5 DEL synthesis

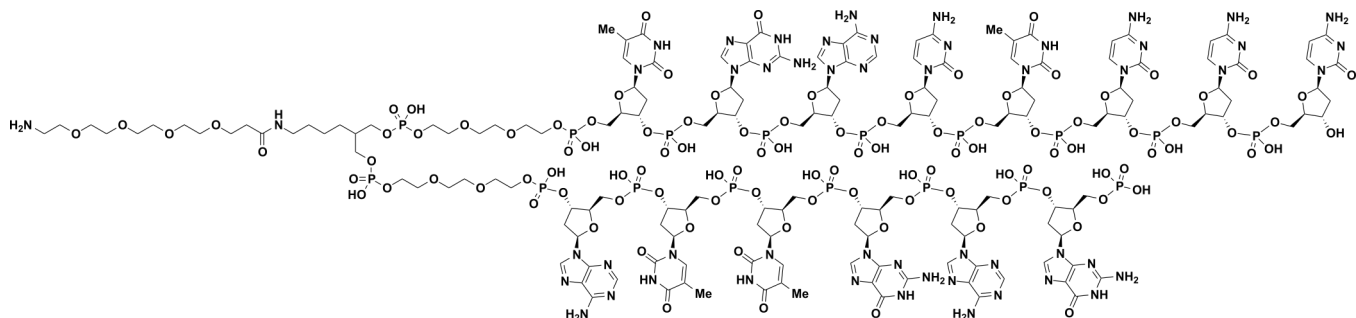


Figure S2: Chemical structure of the “headpiece” with the “AOP-linker.”

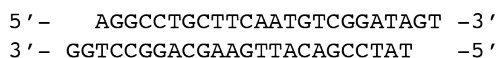


Figure S3: Forward primer binding site duplex.

cycle-1 tags	cycle-2 tags	cycle-3 tags
5' - NNNNNNNCT	NNNNNNNAC	NNNNNNNTT -3'
3' - CANNNNNNN	GANNNNNNN	TGNNNNNNN -5'

Figure S4: Structures of DNA oligonucleotides used as cycle tags.

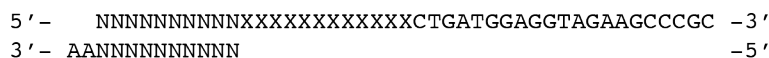


Figure S5: DNA duplex containing the cycle-4 tag (library identifier, designated with N's), unique molecular identifier region (designated with X's), and closing primer binding site.

library	top strand (5' → 3')	bottom strand (5' → 3')
DOS-DEL-1	GTAGTCCTGG	CCAGGACTAC
triazine library	GCTCAACAGC	GCTGTTGAGC

Figure S6: Cycle-4 tag sequences for DOS-DEL-1 and the triazine library.

S1.6 Data processing

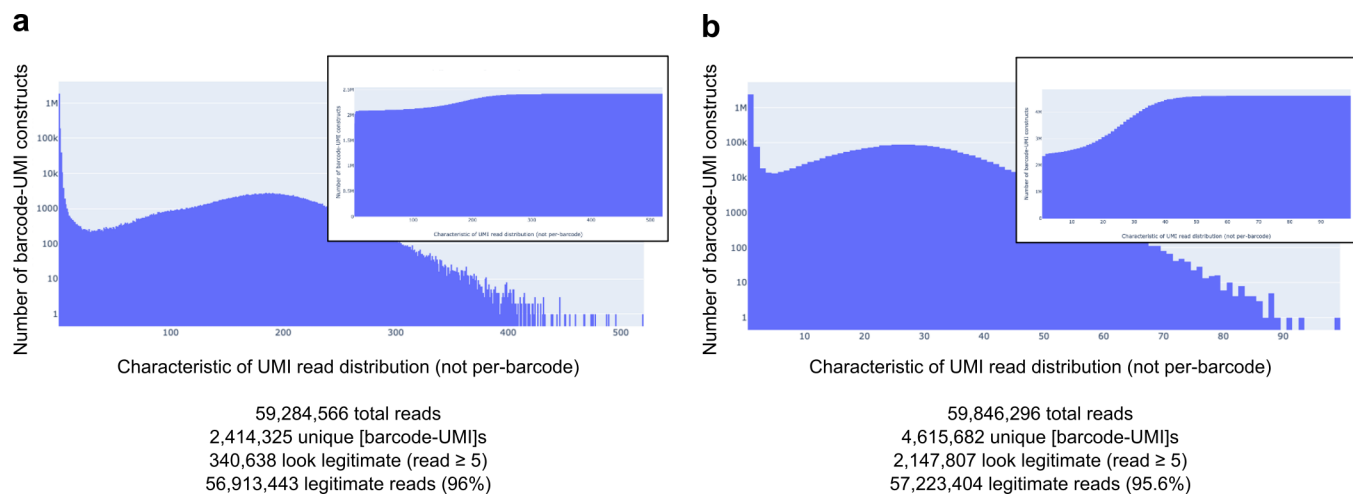


Figure S7: Abundances of UMIs for any ([umi-barcode] construct) for the DD1S CAIX **(a)** experimental (with POI) and **(b)** beads (without POI) data. Insets are cumulative histograms.

S2 Additional Results

S2.1 Hyperparameter optimization

The depth (number of message-passing steps), number of FFN layers, hidden layer size, and dropout rate were fixed for the directed message-passing networks on the triazine datasets, based on the hyperparameter optimization results for the message-passing networks on the DD1S CAIX dataset. For the D-MPNN and D-MPNN pt regression models, we took the mode for the depth (6), number of FFN layers (3), and hidden layer size (1500) based on the aggregated results for the D-MPNN and D-MPNN pt models, and out of the two modes for the dropout rate, we chose 0.05 (Figure S8). For the D-MPNN binary classifiers, we similarly took the mode for the depth (6), number of FFN layers (2), and dropout rate (0), and took the median for the hidden layer size (1500) (Figure S9).

Based on the results from optimization of the number of nearest neighbors (k) for the baseline KNN models on the DD1S CAIX dataset, the k -value was fixed as 9 for all KNN models trained on the triazine datasets.

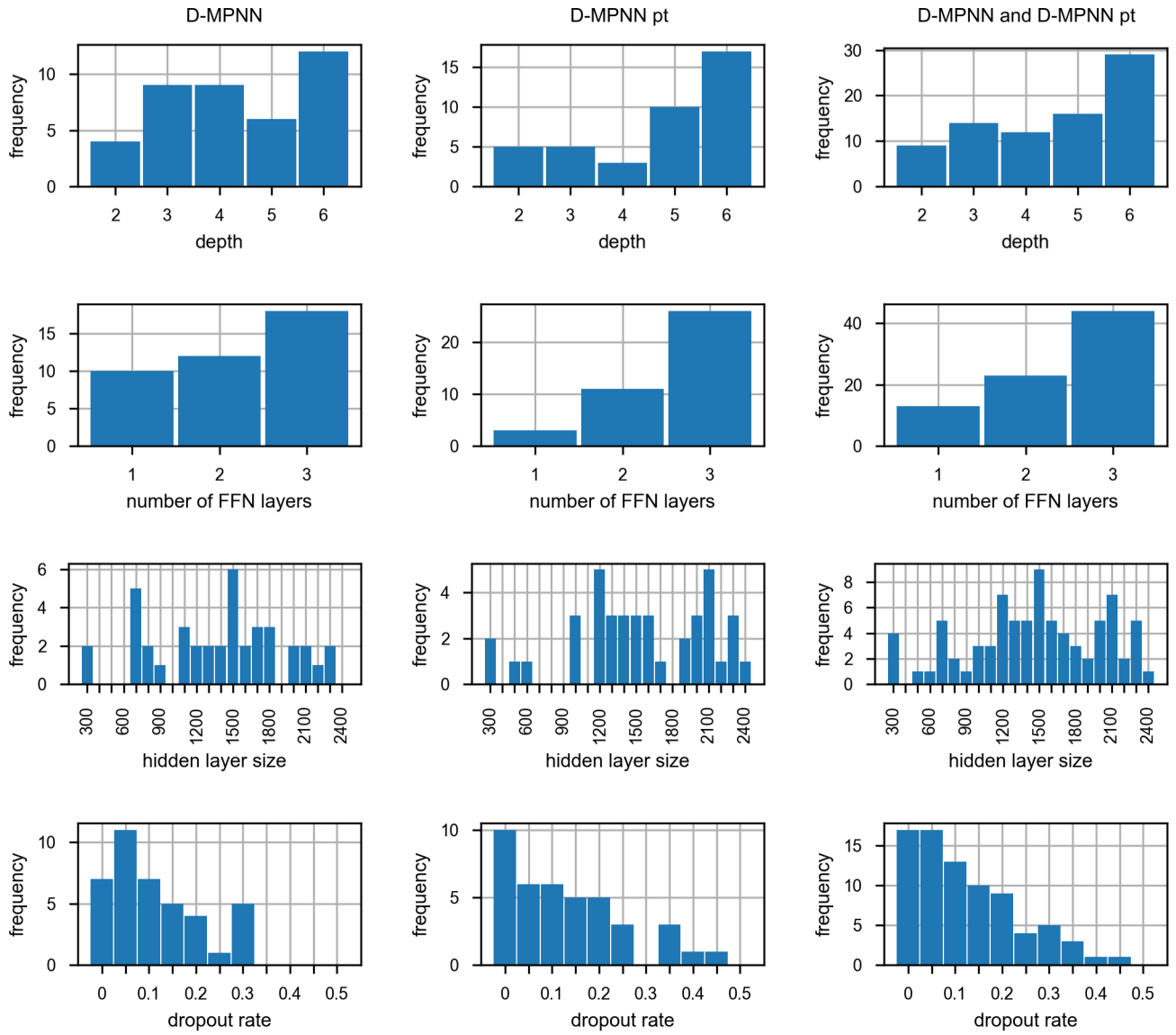


Figure S8: Histograms of optimized hyperparameter values for the D-MPNN and D-MPNN pt regression models (separately and aggregated) on the DD1S CAIX dataset.

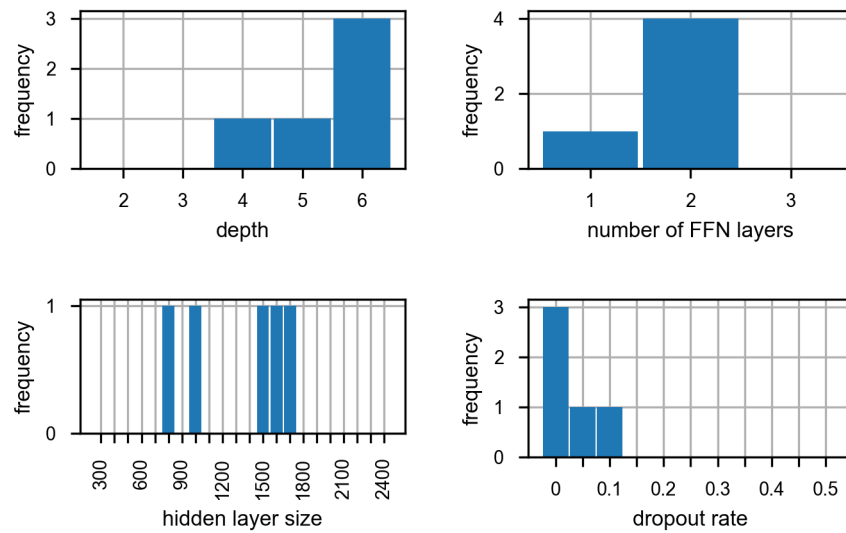


Figure S9: Histograms of optimized hyperparameter values for the D-MPNN binary classifiers on the DD1S CAIX dataset.

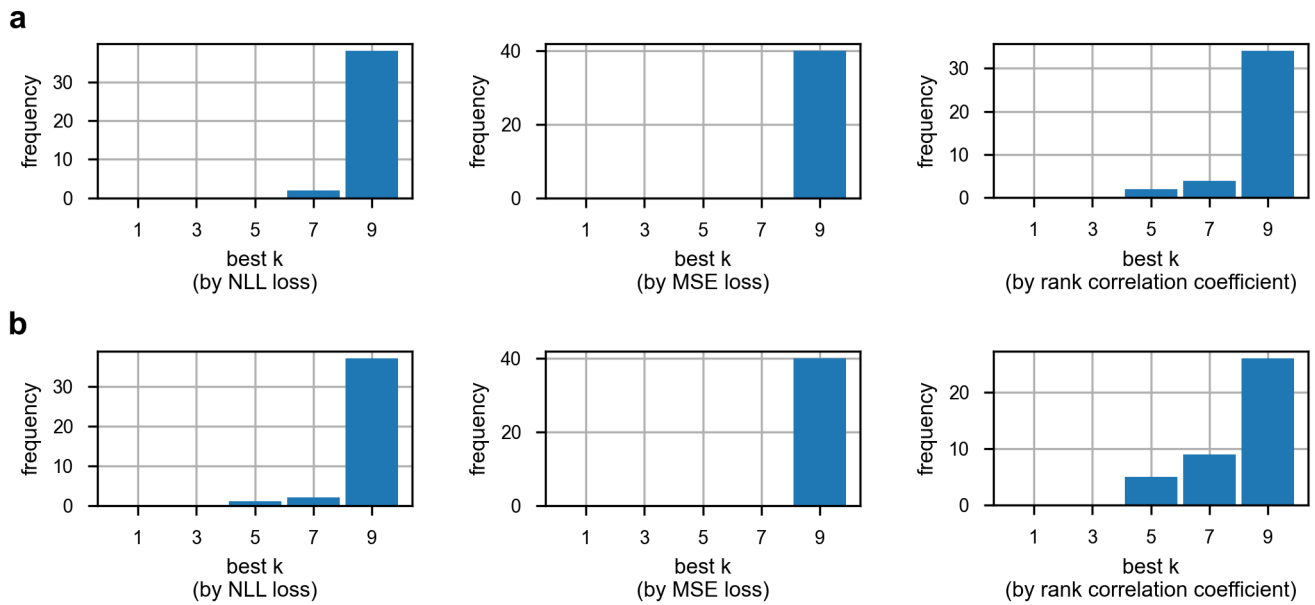


Figure S10: Histograms of optimized k -values for the (a) OH-KNN, (b) FP-KNN baseline models on the DD1S CAIX dataset.

S2.2 Model performance

S2.2.1 NLL test loss

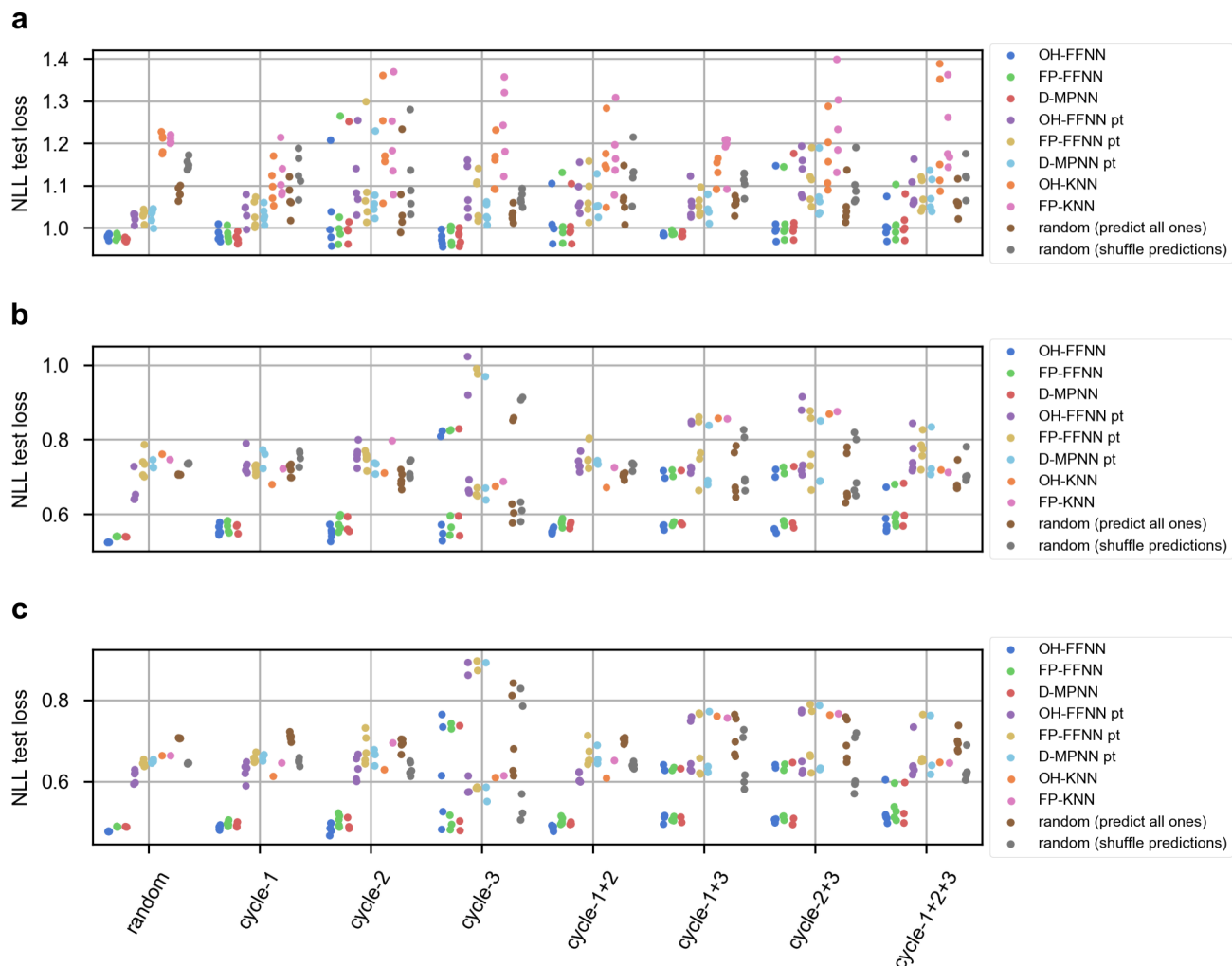


Figure S11: Comparison of model performance, as measured by negative-log likelihood (NLL), for the NLL-trained models (OH-FFNN, FP-FFNN, D-MPNN) versus the baseline point-prediction-trained models (OH-FFNN pt, FP-FFNN pt, D-MPNN pt) for various data splits (*cf.* Figure 2d) on the (a) DD1S CAIX, (b) triazine sEH, (c) triazine SIRT2 datasets. For each dataset, data split type, and model type, the individual test loss for each trial is shown. Five trials were performed for OH-FFNN, FP-FFNN, OH-FFNN pt, FP-FFNN pt, and the random baselines on each dataset; for D-MPNN and D-MPNN pt, five trials were performed on the DD1S CAIX dataset and three trials were performed on the triazine sEH and triazine SIRT2 datasets; for OH-KNN and FP-KNN, five trials were performed on the DD1S CAIX dataset and a single trial (evaluated on a random 10% of the test set) was performed on the triazine sEH and triazine SIRT2 datasets.

Table S4: NLL test losses (mean \pm standard deviation) for regression models and baseline models (KNN and random) on the DD1S CAIX dataset. Results are averaged over five trials.

DD1S CAIX		cycle split		
model	random split	1	2	3
OH-FFNN	0.9791 ± 0.0063	0.9831 ± 0.0163	1.0348 ± 0.1008	0.9730 ± 0.0161
FP-FFNN	0.9795 ± 0.0061	0.9832 ± 0.0145	1.0465 ± 0.1240	0.9845 ± 0.0211
D-MPNN	0.9719 ± 0.0039	0.9735 ± 0.0120	1.0429 ± 0.1179	0.9780 ± 0.0174
OH-FFNN pt	1.0237 ± 0.0116	1.0396 ± 0.0304	1.1146 ± 0.0873	1.0883 ± 0.0607
FP-FFNN pt	1.0295 ± 0.0138	1.0332 ± 0.0322	1.0992 ± 0.1144	1.0793 ± 0.0543
D-MPNN pt	1.0264 ± 0.0186	1.0305 ± 0.0202	1.0856 ± 0.0825	1.0342 ± 0.0232
OH-KNN	1.2018 ± 0.0232	1.1024 ± 0.0463	1.1995 ± 0.1135	1.1486 ± 0.0589
FP-KNN	1.2067 ± 0.0085	1.1233 ± 0.0559	1.2032 ± 0.1126	1.2440 ± 0.0969
random (predict all ones)	1.0828 ± 0.0147	1.0694 ± 0.0385	1.0684 ± 0.0977	1.0318 ± 0.0179
random (shuffle predictions)	1.1511 ± 0.0136	1.1302 ± 0.0477	1.1184 ± 0.0981	1.0694 ± 0.0171

		cycle split		
model	1+2	1+3	2+3	1+2+3
OH-FFNN	1.0140 ± 0.0537	0.9837 ± 0.0025	1.0221 ± 0.0713	1.0063 ± 0.0402
FP-FFNN	1.0171 ± 0.0654	0.9867 ± 0.0044	1.0222 ± 0.0694	1.0150 ± 0.0508
D-MPNN	1.0099 ± 0.0548	0.9822 ± 0.0046	1.0304 ± 0.0826	1.0124 ± 0.0415
OH-FFNN pt	1.0791 ± 0.0482	1.0584 ± 0.0385	1.1282 ± 0.0524	1.0902 ± 0.0455
FP-FFNN pt	1.0739 ± 0.0561	1.0553 ± 0.0266	1.1082 ± 0.0545	1.0772 ± 0.0372
D-MPNN pt	1.0610 ± 0.0389	1.0497 ± 0.0295	1.0781 ± 0.0642	1.0812 ± 0.0421
OH-KNN	1.1589 ± 0.0841	1.1262 ± 0.0344	1.1681 ± 0.0800	1.2174 ± 0.1414
FP-KNN	1.1762 ± 0.0856	1.1794 ± 0.0499	1.2496 ± 0.1044	1.2216 ± 0.0903
random (predict all ones)	1.0676 ± 0.0510	1.0556 ± 0.0178	1.0528 ± 0.0488	1.0620 ± 0.0341
random (shuffle predictions)	1.1293 ± 0.0582	1.1082 ± 0.0246	1.1010 ± 0.0521	1.1199 ± 0.0393

Table S5: NLL test losses (mean \pm standard deviation) for regression models and baseline models on the triazine sEH dataset. OH-FFNN, FP-FFNN, OH-FFNN pt, FP-FFNN pt, random (predict all ones), and random (shuffle predictions) results are averaged over five trials; D-MPNN and D-MPNN pt results are averaged over three trials; OH-KNN and FP-KNN results are single trials evaluated on a random 10% of the test set.

triazine sEH		cycle split		
model	random split	1	2	3
OH-FFNN	0.5240 ± 0.0002	0.5576 ± 0.0139	0.5490 ± 0.0170	0.6556 ± 0.1469
FP-FFNN	0.5400 ± 0.0004	0.5665 ± 0.0146	0.5752 ± 0.0198	0.6705 ± 0.1420
D-MPNN	0.5390 ± 0.0006	0.5619 ± 0.0129	0.5685 ± 0.0213	0.6551 ± 0.1526
OH-FFNN pt	0.6601 ± 0.0381	0.7363 ± 0.0312	0.7594 ± 0.0279	0.7909 ± 0.1688
FP-FFNN pt	0.7331 ± 0.0345	0.7197 ± 0.0117	0.7494 ± 0.0206	0.7874 ± 0.1787
D-MPNN pt	0.7319 ± 0.0120	0.7518 ± 0.0262	0.7263 ± 0.0165	0.7588 ± 0.1827
OH-KNN	0.7622	0.6801	0.7109	0.6759
FP-KNN	0.7463	0.7220	0.7980	0.6879
random (predict all ones)	0.7058 ± 0.0008	0.7156 ± 0.0171	0.6924 ± 0.0211	0.7030 ± 0.1398
random (shuffle predictions)	0.7357 ± 0.0012	0.7466 ± 0.0204	0.7185 ± 0.0228	0.7281 ± 0.1669

	cycle split			
model	1+2	1+3	2+3	1+2+3
OH-FFNN	0.5554 ± 0.0074	0.6218 ± 0.0778	0.6174 ± 0.0846	0.5882 ± 0.0486
FP-FFNN	0.5780 ± 0.0099	0.6284 ± 0.0745	0.6333 ± 0.0770	0.6031 ± 0.0445
D-MPNN	0.5706 ± 0.0085	0.6214 ± 0.0827	0.6219 ± 0.0916	0.6155 ± 0.0598
OH-FFNN pt	0.7361 ± 0.0211	0.7698 ± 0.0695	0.7893 ± 0.0993	0.7595 ± 0.0523
FP-FFNN pt	0.7635 ± 0.0370	0.7768 ± 0.0805	0.7777 ± 0.0890	0.7723 ± 0.0394
D-MPNN pt	0.7380 ± 0.0050	0.7355 ± 0.0888	0.7423 ± 0.0932	0.7538 ± 0.0697
OH-KNN	0.6719	0.8572	0.8686	0.7189
FP-KNN	0.7253	0.8559	0.8756	0.7126
random (predict all ones)	0.7024 ± 0.0077	0.7054 ± 0.0638	0.6951 ± 0.0704	0.6871 ± 0.0329
random (shuffle predictions)	0.7309 ± 0.0090	0.7353 ± 0.0750	0.7233 ± 0.0800	0.7138 ± 0.0378

Table S6: NLL test losses (mean \pm standard deviation) for regression models and baseline models on the triazine SIRT2 dataset. OH-FFNN, FP-FFNN, OH-FFNN pt, FP-FFNN pt, and random baseline results are averaged over five trials; D-MPNN and D-MPNN pt results are averaged over three trials; OH-KNN and FP-KNN results are single trials evaluated on a random 10% of the test set.

triazine SIRT2		cycle split			
model	random split	1	2	3	
OH-FFNN	0.4770 ± 0.0005	0.4858 ± 0.0052	0.4850 ± 0.0131	0.6243 ± 0.1246	
FP-FFNN	0.4884 ± 0.0008	0.4975 ± 0.0067	0.5046 ± 0.0149	0.5930 ± 0.1316	
D-MPNN	0.4882 ± 0.0007	0.4931 ± 0.0063	0.4946 ± 0.0146	0.5730 ± 0.1429	
OH-FFNN pt	0.6122 ± 0.0159	0.6254 ± 0.0225	0.6321 ± 0.0295	0.7034 ± 0.1602	
FP-FFNN pt	0.6433 ± 0.0070	0.6567 ± 0.0097	0.6812 ± 0.0374	0.7049 ± 0.1649	
D-MPNN pt	0.6495 ± 0.0044	0.6594 ± 0.0079	0.6611 ± 0.0204	0.6765 ± 0.1882	
OH-KNN	0.6648	0.6141	0.6304	0.6103	
FP-KNN	0.6638	0.6460	0.6956	0.6142	
random (predict all ones)	0.7065 ± 0.0009	0.7101 ± 0.0095	0.6918 ± 0.0154	0.7152 ± 0.1058	
random (shuffle predictions)	0.6449 ± 0.0009	0.6498 ± 0.0080	0.6315 ± 0.0162	0.6423 ± 0.1533	

model	cycle split			
	1+2	1+3	2+3	1+2+3
OH-FFNN	0.4862 ± 0.0059	0.5583 ± 0.0700	0.5574 ± 0.0733	0.5282 ± 0.0431
FP-FFNN	0.5033 ± 0.0087	0.5569 ± 0.0679	0.5607 ± 0.0683	0.5353 ± 0.0363
D-MPNN	0.4965 ± 0.0031	0.5477 ± 0.0731	0.5499 ± 0.0842	0.5388 ± 0.0521
OH-FFNN pt	0.6096 ± 0.0122	0.6814 ± 0.0667	0.6884 ± 0.0778	0.6507 ± 0.0474
FP-FFNN pt	0.6668 ± 0.0285	0.6863 ± 0.0757	0.7023 ± 0.0746	0.6746 ± 0.0507
D-MPNN pt	0.6625 ± 0.0236	0.6774 ± 0.0826	0.6833 ± 0.0901	0.6735 ± 0.0783
OH-KNN	0.6090	0.7621	0.7646	0.6477
FP-KNN	0.6523	0.7566	0.7682	0.6459
random (predict all ones)	0.7008 ± 0.0065	0.7094 ± 0.0483	0.7011 ± 0.0523	0.6967 ± 0.0255
random (shuffle predictions)	0.6392 ± 0.0071	0.6464 ± 0.0669	0.6385 ± 0.0700	0.6301 ± 0.0340

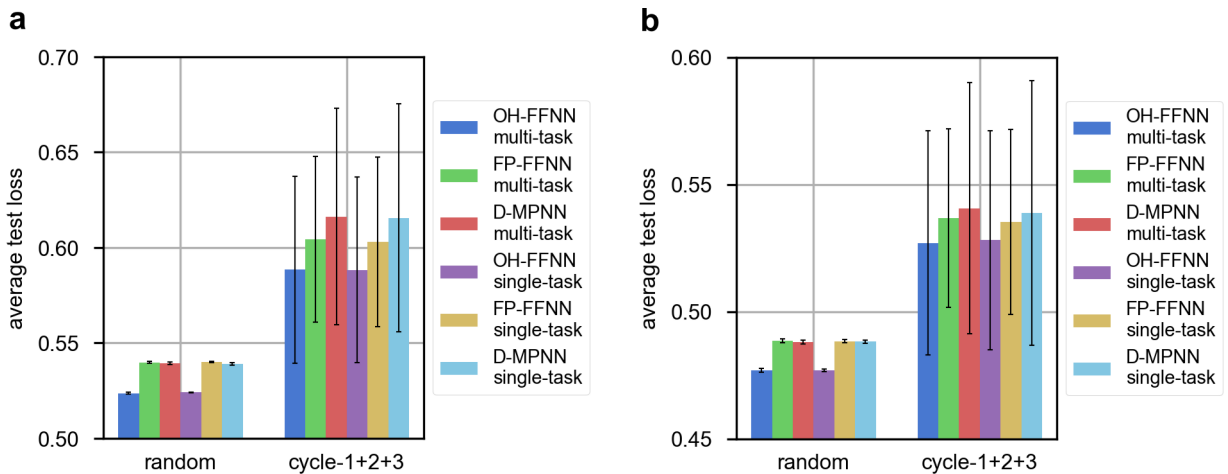


Figure S12: Comparison of model performance, as measured by negative-log likelihood, for the multi-task versus single-task models on the (a) triazine sEH and (b) triazine SIRT2 datasets. Error bars represent \pm one standard deviation. OH-FFNN and FP-FFNN results are averaged over five trials; D-MPNN results are averaged over three trials.

S2.2.2 MSE test loss

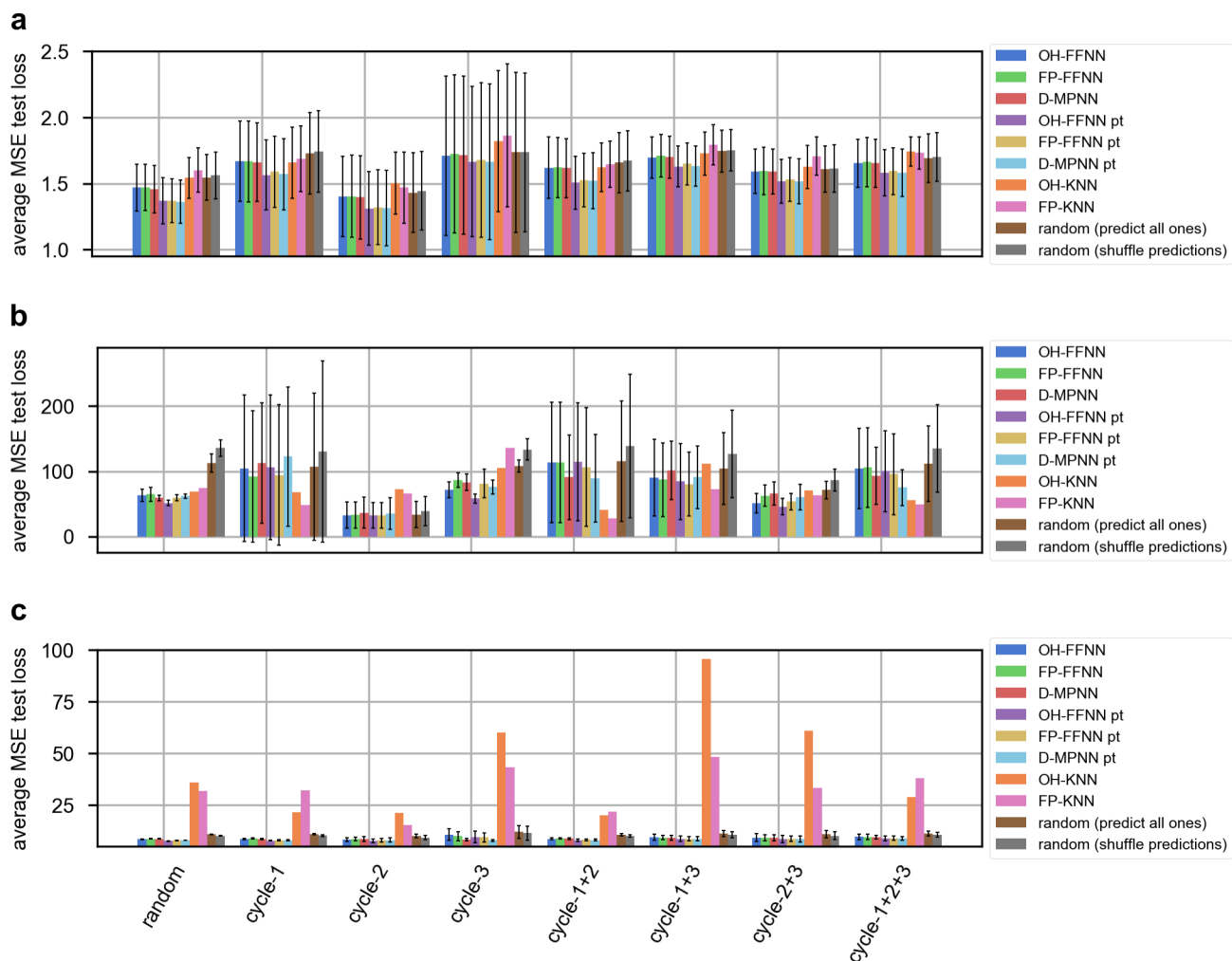


Figure S13: Comparison of model performance, as measured by mean-squared error (MSE). OH: one-hot; FP: fingerprint; FFNN: feed-forward neural network; D-MPNN: directed message-passing neural network; KNN: k-nearest neighbors. The MSE test losses of the negative-log-likelihood-trained models (OH-FFNN, FP-FFNN, D-MPNN) are compared to those of the baseline point-prediction-trained models (OH-FFNN pt, FP-FFNN pt, D-MPNN pt), k-nearest-neighbors models (OH-KNN, FP-KNN), and random models (predict all ones, shuffle predictions), for various data splits (*cf.* Figure 2d) on the (a) DD1S CAIX, (b) triazine sEH, (c) triazine SIRT2 datasets. Error bars represent \pm one standard deviation. OH-FFNN, FP-FFNN, OH-FFNN pt, FP-FFNN pt, random (predict all ones), and random (shuffle predictions) results are averaged over five trials for each dataset; D-MPNN and D-MPNN pt results are averaged over five trials for the DD1S CAIX dataset and over three trials for the triazine sEH and triazine SIRT2 datasets; OH-KNN and FP-KNN results are averaged over five trials for the DD1S CAIX dataset and are single trials (evaluated on a random 10% of the test set) for the triazine sEH and triazine SIRT2 datasets. The result of each trial is shown separately below (Figure S14).

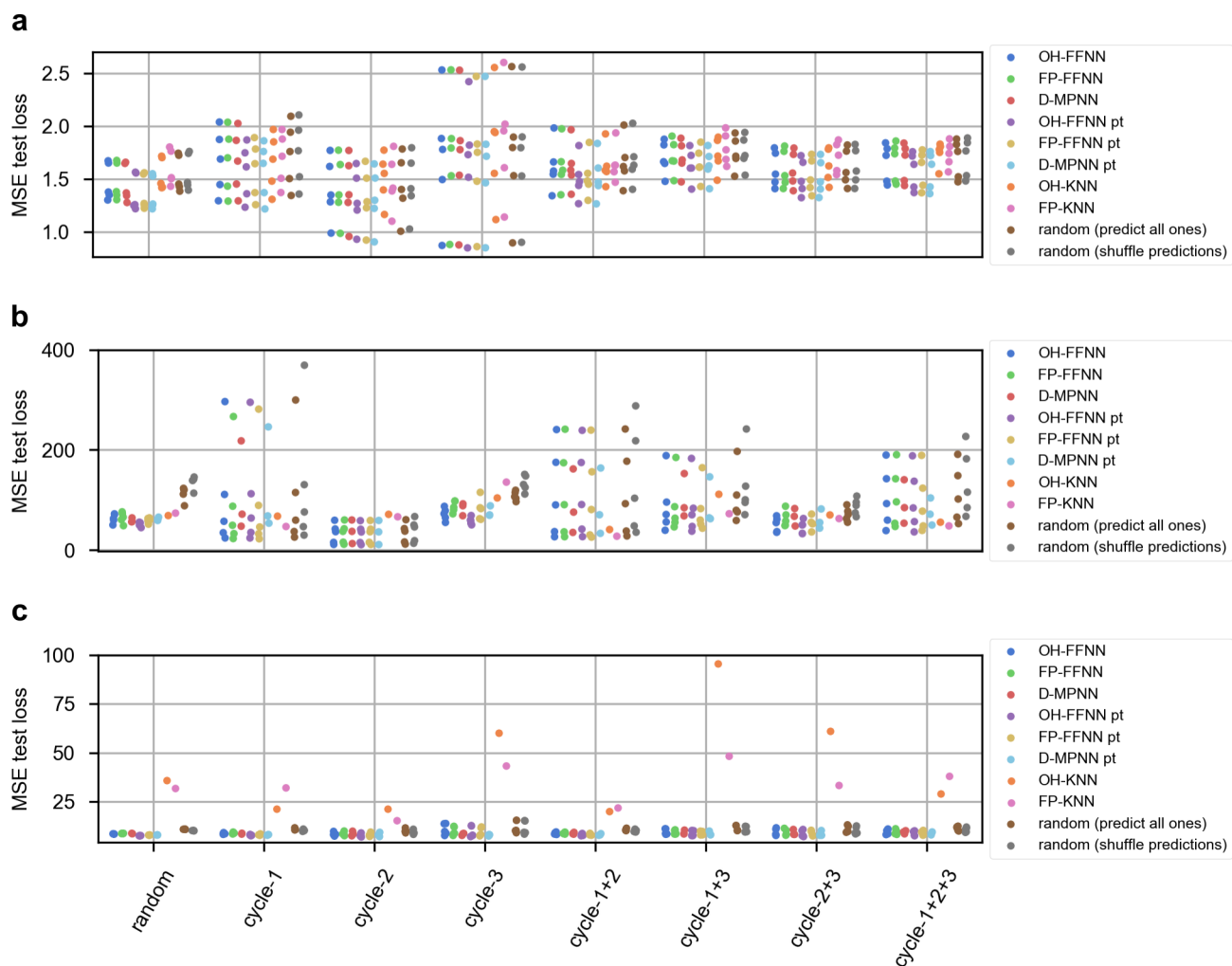


Figure S14: Comparison of model performance, as measured by mean-squared error (MSE), for the negative-log-likelihood-trained models (OH-FFNN, FP-FFNN, D-MPNN) versus the baseline point-prediction-trained models (OH-FFNN pt, FP-FFNN pt, D-MPNN pt) for various data splits (*cf.* Figure 2d) on the **(a)** DD1S CAIX, **(b)** triazine sEH, **(c)** triazine SIRT2 datasets. For each dataset, data split type, and model type, the individual test loss for each trial is shown. Five trials were performed for OH-FFNN, FP-FFNN, OH-FFNN pt, FP-FFNN pt, and the random baselines on each dataset; for D-MPNN and D-MPNN pt, five trials were performed on the DD1S CAIX dataset and three trials were performed on the triazine sEH and triazine SIRT2 datasets; for OH-KNN and FP-KNN, five trials were performed on the DD1S CAIX dataset and a single trial (evaluated on a random 10% of the test set) was performed on the triazine sEH and triazine SIRT2 datasets.

Table S7: MSE test losses (mean \pm standard deviation) for regression models and baseline models on the DD1S CAIX dataset. Results are averaged over five trials.

DD1S CAIX		cycle split		
model	random split	1	2	3
OH-FFNN	1.4690 ± 0.1772	1.6675 ± 0.3039	1.4007 ± 0.3047	1.7111 ± 0.6044
FP-FFNN	1.4707 ± 0.1771	1.6665 ± 0.3078	1.4037 ± 0.3096	1.7228 ± 0.5988
D-MPNN	1.4578 ± 0.1803	1.6602 ± 0.2975	1.3951 ± 0.3172	1.7153 ± 0.5970
OH-FFNN pt	1.3682 ± 0.1753	1.5639 ± 0.2651	1.3107 ± 0.2782	1.6662 ± 0.5680
FP-FFNN pt	1.3693 ± 0.1674	1.5886 ± 0.2696	1.3207 ± 0.2848	1.6775 ± 0.5846
D-MPNN pt	1.3610 ± 0.1626	1.5704 ± 0.2699	1.3143 ± 0.2839	1.6645 ± 0.5886
OH-KNN	1.5420 ± 0.1523	1.6580 ± 0.2689	1.5044 ± 0.2347	1.8214 ± 0.5335
FP-KNN	1.6015 ± 0.1684	1.6870 ± 0.2493	1.4687 ± 0.2694	1.8638 ± 0.5405
random (predict all ones)	1.5452 ± 0.1732	1.7276 ± 0.3077	1.4313 ± 0.3036	1.7359 ± 0.6049
random (shuffle predictions)	1.5606 ± 0.1756	1.7418 ± 0.3075	1.4432 ± 0.2969	1.7356 ± 0.6020

		cycle split		
model	1+2	1+3	2+3	1+2+3
OH-FFNN	1.6202 ± 0.2337	1.6965 ± 0.1580	1.5918 ± 0.1693	1.6539 ± 0.1822
FP-FFNN	1.6221 ± 0.2279	1.7102 ± 0.1625	1.5955 ± 0.1798	1.6635 ± 0.1866
D-MPNN	1.6168 ± 0.2230	1.6996 ± 0.1598	1.5893 ± 0.1697	1.6541 ± 0.1821
OH-FFNN pt	1.5067 ± 0.2005	1.6290 ± 0.1548	1.5166 ± 0.1676	1.5807 ± 0.1744
FP-FFNN pt	1.5249 ± 0.2019	1.6482 ± 0.1582	1.5302 ± 0.1666	1.5926 ± 0.1791
D-MPNN pt	1.5215 ± 0.2131	1.6301 ± 0.1520	1.5165 ± 0.1712	1.5804 ± 0.1785
OH-KNN	1.6243 ± 0.1839	1.7265 ± 0.1643	1.6260 ± 0.1639	1.7424 ± 0.1125
FP-KNN	1.6456 ± 0.1746	1.7935 ± 0.1512	1.7069 ± 0.1454	1.7312 ± 0.1222
random (predict all ones)	1.6585 ± 0.2275	1.7451 ± 0.1585	1.6086 ± 0.1767	1.6910 ± 0.1836
random (shuffle predictions)	1.6714 ± 0.2285	1.7514 ± 0.1580	1.6133 ± 0.1784	1.7011 ± 0.1846

Table S8: MSE test losses (mean \pm standard deviation) for regression models and baseline models on the triazine sEH dataset. OH-FFNN, FP-FFNN, OH-FFNN pt, FP-FFNN pt, random (predict all ones), and random (shuffle predictions) results are averaged over five trials; D-MPNN and D-MPNN pt results are averaged over three trials; OH-KNN and FP-KNN results are single trials evaluated on a random 10% of the test set.

triazine sEH		cycle split		
model	random split	1	2	3
OH-FFNN	63.1165 \pm 9.1153	104.6138 \pm 112.4744	32.6997 \pm 19.9417	71.4771 \pm 12.4136
FP-FFNN	64.6382 \pm 10.9077	91.7278 \pm 100.8977	33.1806 \pm 20.0352	86.6032 \pm 11.1850
D-MPNN	59.0148 \pm 4.4403	112.3067 \pm 92.4066	36.5230 \pm 23.5934	82.9586 \pm 12.7764
OH-FFNN pt	51.3925 \pm 4.4271	105.9992 \pm 111.1797	32.1739 \pm 19.7865	58.0676 \pm 7.1649
FP-FFNN pt	59.3360 \pm 4.9986	94.1664 \pm 107.8041	32.5065 \pm 19.7674	81.0961 \pm 21.9021
D-MPNN pt	62.1430 \pm 3.3269	122.5217 \pm 107.2855	35.2012 \pm 24.1319	75.8201 \pm 10.7562
OH-KNN	68.8859	67.8826	72.0830	105.1172
FP-KNN	73.9428	47.8342	66.3675	136.0269
random (predict all ones)	112.7630 \pm 14.3542	107.2573 \pm 112.9778	33.5890 \pm 20.0749	108.0191 \pm 9.1461
random (shuffle predictions)	135.7934 \pm 12.7459	130.3497 \pm 139.0098	38.8306 \pm 22.4695	133.3429 \pm 16.3413
	cycle split			
model	1+2	1+3	2+3	1+2+3
OH-FFNN	113.7291 \pm 92.2577	90.0097 \pm 58.8666	51.1786 \pm 14.8026	104.5738 \pm 61.6597
FP-FFNN	113.7116 \pm 92.3884	87.1879 \pm 56.6259	62.6018 \pm 16.3096	105.7660 \pm 60.8721
D-MPNN	90.8070 \pm 64.8965	101.6983 \pm 44.9100	65.8889 \pm 17.5284	92.7588 \pm 44.0416
OH-FFNN pt	114.5469 \pm 90.5483	84.1884 \pm 58.1733	45.7241 \pm 12.8903	100.4466 \pm 62.0703
FP-FFNN pt	106.4167 \pm 91.1926	80.3312 \pm 49.2571	53.4952 \pm 12.6520	95.4048 \pm 61.8960
D-MPNN pt	89.0670 \pm 67.3121	90.8949 \pm 47.8299	60.0897 \pm 19.7125	74.9849 \pm 27.3220
OH-KNN	40.8193	112.1089	70.5626	55.3985
FP-KNN	27.5076	72.3482	63.1585	48.6848
random (predict all ones)	115.4427 \pm 92.2479	104.1369 \pm 55.0694	71.2054 \pm 13.5378	111.8880 \pm 57.8742
random (shuffle predictions)	138.5909 \pm 110.4645	126.9835 \pm 67.2980	86.4051 \pm 16.5700	135.2677 \pm 67.4508

Table S9: MSE test losses (mean \pm standard deviation) for regression models and baseline models on the triazine SIRT2 dataset. OH-FFNN, FP-FFNN, OH-FFNN pt, FP-FFNN pt, random (predict all ones), and random (shuffle predictions) results are averaged over five trials; D-MPNN and D-MPNN pt results are averaged over three trials; OH-KNN and FP-KNN results are single trials evaluated on a random 10% of the test set.

triazine SIRT2		cycle split		
model	random split	1	2	3
OH-FFNN	0.4770 ± 0.0005	0.4858 ± 0.0052	0.4850 ± 0.0131	0.6243 ± 0.1246
FP-FFNN	0.4884 ± 0.0008	0.4975 ± 0.0067	0.5046 ± 0.0149	0.5930 ± 0.1316
D-MPNN	0.4882 ± 0.0007	0.4931 ± 0.0063	0.4946 ± 0.0146	0.5730 ± 0.1429
OH-FFNN pt	0.6122 ± 0.0159	0.6254 ± 0.0225	0.6321 ± 0.0295	0.7034 ± 0.1602
FP-FFNN pt	0.6433 ± 0.0070	0.6567 ± 0.0097	0.6812 ± 0.0374	0.7049 ± 0.1649
D-MPNN pt	0.6495 ± 0.0044	0.6594 ± 0.0079	0.6611 ± 0.0204	0.6765 ± 0.1882
OH-KNN	0.6648	0.6141	0.6304	0.6103
FP-KNN	0.6638	0.6460	0.6956	0.6142
random (predict all ones)	0.7065 ± 0.0009	0.7101 ± 0.0095	0.6918 ± 0.0154	0.7152 ± 0.1058
random (shuffle predictions)	0.6449 ± 0.0009	0.6498 ± 0.0080	0.6315 ± 0.0162	0.6423 ± 0.1533

	cycle split			
model	1+2	1+3	2+3	1+2+3
OH-FFNN	0.4862 ± 0.0059	0.5583 ± 0.0700	0.5574 ± 0.0733	0.5282 ± 0.0431
FP-FFNN	0.5033 ± 0.0087	0.5569 ± 0.0679	0.5607 ± 0.0683	0.5353 ± 0.0363
D-MPNN	0.4965 ± 0.0031	0.5477 ± 0.0731	0.5499 ± 0.0842	0.5388 ± 0.0521
OH-FFNN pt	0.6096 ± 0.0122	0.6814 ± 0.0667	0.6884 ± 0.0778	0.6507 ± 0.0474
FP-FFNN pt	0.6668 ± 0.0285	0.6863 ± 0.0757	0.7023 ± 0.0746	0.6746 ± 0.0507
D-MPNN pt	0.6625 ± 0.0236	0.6774 ± 0.0826	0.6833 ± 0.0901	0.6735 ± 0.0783
OH-KNN	0.6090	0.7621	0.7646	0.6477
FP-KNN	0.6523	0.7566	0.7682	0.6459
random (predict all ones)	0.7008 ± 0.0065	0.7094 ± 0.0483	0.7011 ± 0.0523	0.6967 ± 0.0255
random (shuffle predictions)	0.6392 ± 0.0071	0.6464 ± 0.0669	0.6385 ± 0.0700	0.6301 ± 0.0340

S2.2.3 Rank correlation coefficient

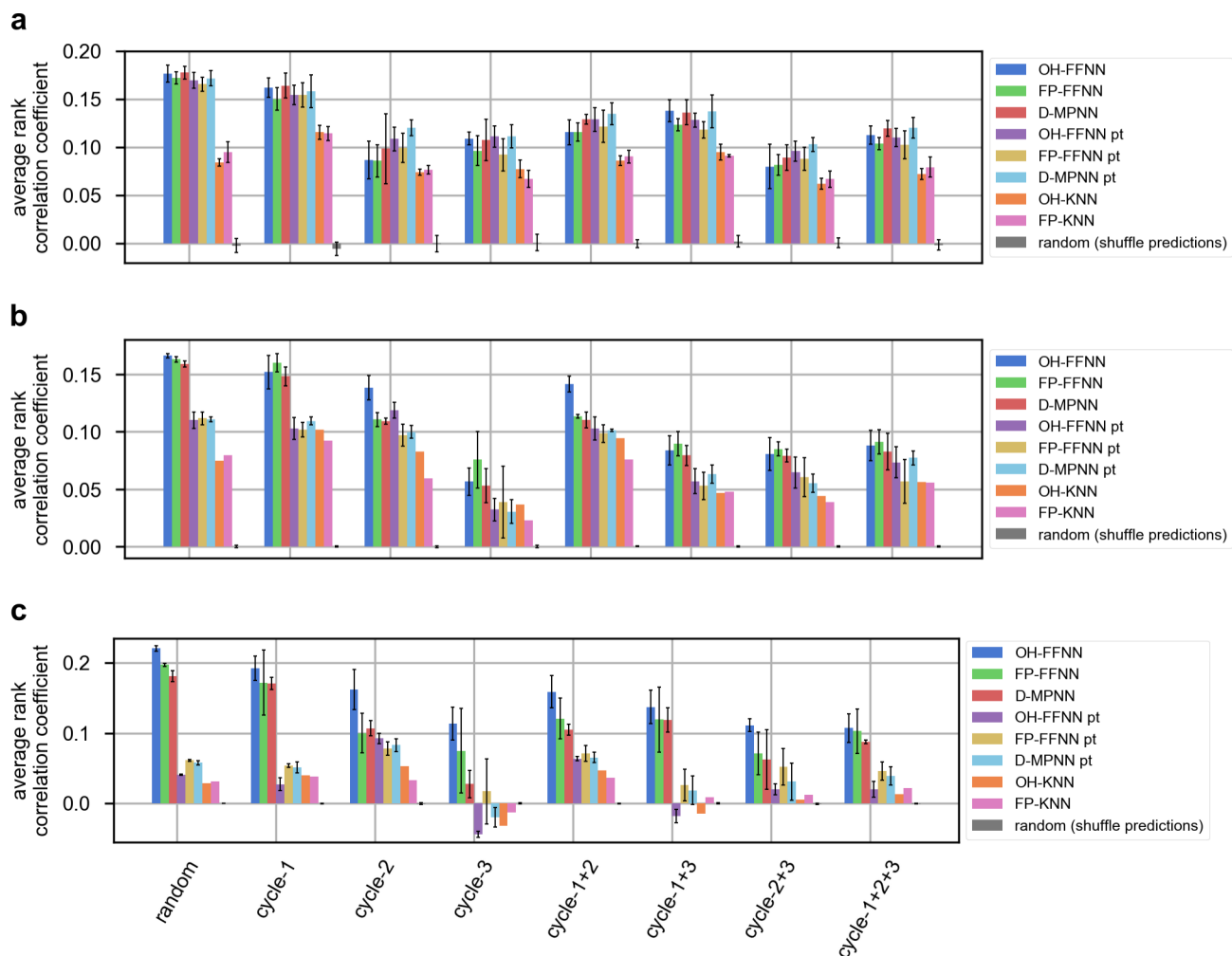


Figure S15: Comparison of model performance, as measured by rank correlation coefficient. OH: one-hot; FP: fingerprint; FFNN: feed-forward neural network; D-MPNN: directed message-passing neural network; KNN: k-nearest neighbors. The rank correlation coefficients of the negative-log-likelihood-trained models (OH-FFNN, FP-FFNN, D-MPNN) are compared to the baseline point-prediction-trained models (OH-FFNN pt, FP-FFNN pt, D-MPNN pt), k-nearest-neighbors models (OH-KNN, FP-KNN), and random models (predict all ones, shuffle predictions), for various data splits (*cf.* Figure 2d) on the (a) DD1S CAIX, (b) triazine sEH, (c) triazine SIRT2 datasets. Error bars represent \pm one standard deviation. OH-FFNN, FP-FFNN, OH-FFNN pt, FP-FFNN pt, random (predict all ones), and random (shuffle predictions) results are averaged over five trials for each dataset; D-MPNN and D-MPNN pt results are averaged over five trials for the DD1S CAIX dataset and over three trials for the triazine sEH and triazine SIRT2 datasets; OH-KNN and FP-KNN results are averaged over five trials for the DD1S CAIX dataset and are single trials (evaluated on a random 10% of the test set) for the triazine sEH and triazine SIRT2 datasets. The result of each trial is shown separately below (Figure S16).

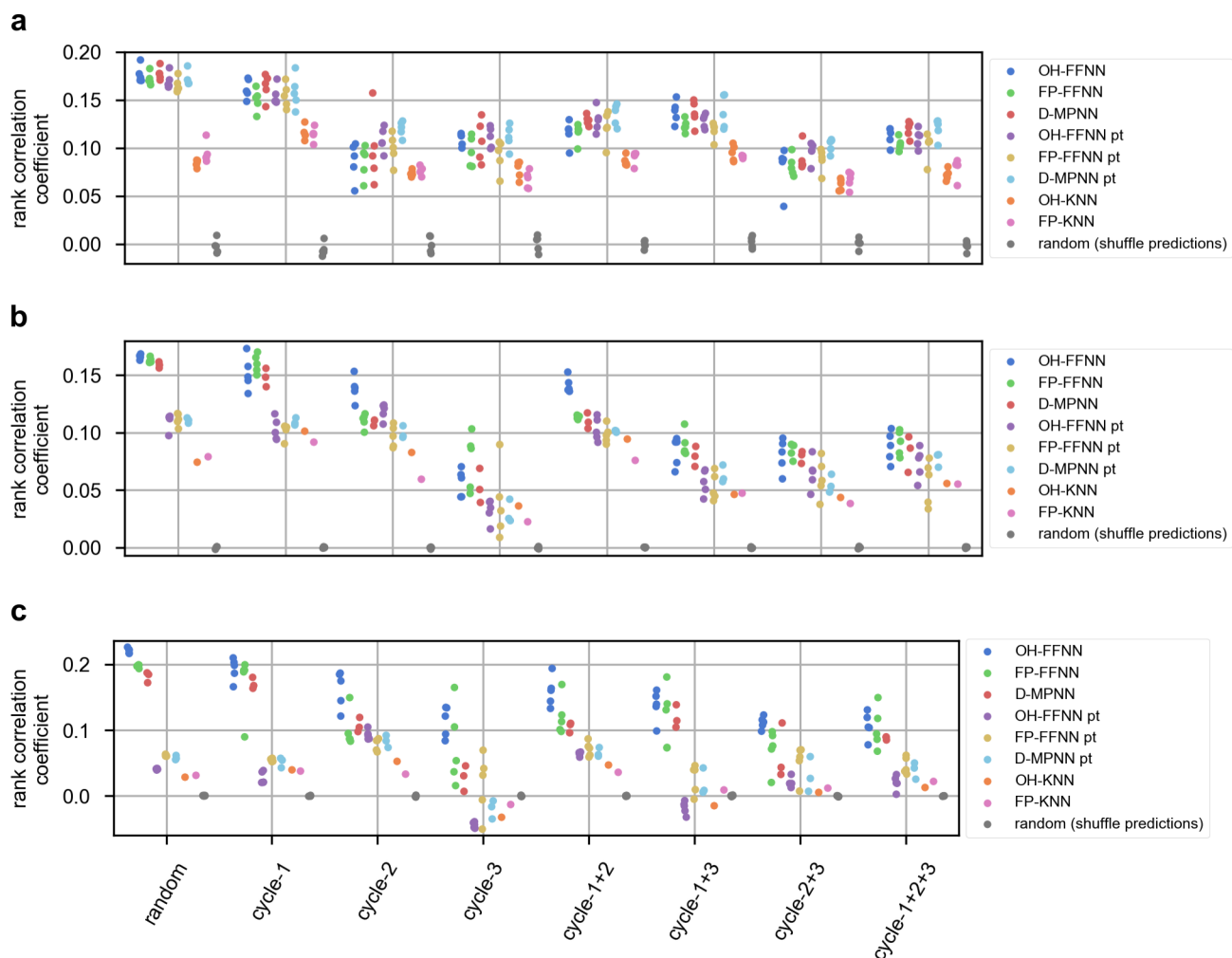


Figure S16: Comparison of model performance, as measured by rank correlation coefficient, for the negative-log-likelihood-trained models (OH-FFNN, FP-FFNN, D-MPNN) versus the baseline point-prediction-trained models (OH-FFNN pt, FP-FFNN pt, D-MPNN pt), k-nearest-neighbors models (OH-KNN, FP-KNN), and random models (predict all ones, shuffle predictions), for various data splits (*cf.* Figure 2d) on the (a) DD1S CAIX, (b) triazine sEH, (c) triazine SIRT2 datasets. For each dataset, data split type, and model type, the individual rank correlation coefficient for each trial is shown. Five trials were performed for OH-FFNN, FP-FFNN, OH-FFNN pt, FP-FFNN pt, and the random baselines (predict all ones, shuffle predictions) on each dataset; for D-MPNN and D-MPNN pt, five trials were performed on the DD1S CAIX dataset and three trials were performed on the triazine sEH and triazine SIRT2 datasets; for OH-KNN and FP-KNN, five trials were performed on the DD1S CAIX dataset and one trial (evaluated on a random 10% of the test set) was performed on the triazine sEH and triazine SIRT2 datasets.

Table S10: Rank correlation coefficients (mean \pm standard deviation) for regression models and baseline models on the DD1S CAIX dataset. Results are averaged over five trials.

DD1S CAIX		cycle split		
model	random split	1	2	3
OH-FFNN	0.1767 ± 0.0089	0.1619 ± 0.0102	0.0867 ± 0.0197	0.1093 ± 0.0067
FP-FFNN	0.1720 ± 0.0064	0.1503 ± 0.0115	0.0859 ± 0.0167	0.0965 ± 0.0155
D-MPNN	0.1776 ± 0.0065	0.1641 ± 0.0131	0.0986 ± 0.0362	0.1076 ± 0.0216
OH-FFNN pt	0.1699 ± 0.0082	0.1547 ± 0.0102	0.1088 ± 0.0123	0.1112 ± 0.0108
FP-FFNN pt	0.1655 ± 0.0074	0.1546 ± 0.0124	0.0996 ± 0.0153	0.0923 ± 0.0167
D-MPNN pt	0.1718 ± 0.0078	0.1584 ± 0.0171	0.1203 ± 0.0080	0.1116 ± 0.0122
OH-KNN	0.0844 ± 0.0037	0.1157 ± 0.0071	0.0739 ± 0.0032	0.0777 ± 0.0091
FP-KNN	0.0949 ± 0.0108	0.1144 ± 0.0071	0.0766 ± 0.0045	0.0673 ± 0.0088
random (shuffle predictions)	-0.0021 ± 0.0072	-0.0054 ± 0.0069	-0.0001 ± 0.0085	0.0011 ± 0.0084

		cycle split		
model	1+2	1+3	2+3	1+2+3
OH-FFNN	0.1157 ± 0.0128	0.1380 ± 0.0115	0.0801 ± 0.0231	0.1126 ± 0.0093
FP-FFNN	0.1159 ± 0.0097	0.1233 ± 0.0064	0.0817 ± 0.0108	0.1041 ± 0.0064
D-MPNN	0.1290 ± 0.0051	0.1364 ± 0.0128	0.0893 ± 0.0133	0.1197 ± 0.0083
OH-FFNN pt	0.1290 ± 0.0123	0.1284 ± 0.0072	0.0962 ± 0.0103	0.1103 ± 0.0097
FP-FFNN pt	0.1219 ± 0.0166	0.1182 ± 0.0087	0.0882 ± 0.0118	0.1027 ± 0.0143
D-MPNN pt	0.1350 ± 0.0113	0.1376 ± 0.0172	0.1030 ± 0.0073	0.1205 ± 0.0106
OH-KNN	0.0863 ± 0.0051	0.0951 ± 0.0083	0.0622 ± 0.0060	0.0723 ± 0.0056
FP-KNN	0.0905 ± 0.0066	0.0912 ± 0.0014	0.0671 ± 0.0084	0.0794 ± 0.0104
random (shuffle predictions)	-0.0001 ± 0.0040	0.0023 ± 0.0059	0.0009 ± 0.0053	-0.0014 ± 0.0052

Table S11: Rank correlation coefficients (mean \pm standard deviation) for regression models and baseline models on the triazine sEH dataset. OH-FFNN, FP-FFNN, OH-FFNN pt, FP-FFNN pt, random (predict all ones), and random (shuffle predictions) results are averaged over five trials; D-MPNN and D-MPNN pt results are averaged over three trials; OH-KNN and FP-KNN results are single trials evaluated on a random 10% of the test set.

triazine sEH		cycle split		
model	random split	1	2	3
OH-FFNN	0.1660 ± 0.0020	0.1517 ± 0.0146	0.1384 ± 0.0106	0.0566 ± 0.0119
FP-FFNN	0.1629 ± 0.0022	0.1600 ± 0.0080	0.1104 ± 0.0062	0.0755 ± 0.0244
D-MPNN	0.1589 ± 0.0027	0.1480 ± 0.0080	0.1091 ± 0.0028	0.0529 ± 0.0149
OH-FFNN pt	0.1101 ± 0.0071	0.1028 ± 0.0096	0.1185 ± 0.0069	0.0322 ± 0.0098
FP-FFNN pt	0.1115 ± 0.0054	0.1016 ± 0.0064	0.0969 ± 0.0094	0.0387 ± 0.0314
D-MPNN pt	0.1106 ± 0.0023	0.1092 ± 0.0033	0.0996 ± 0.0055	0.0303 ± 0.0103
OH-KNN	0.0747	0.1017	0.0828	0.0365
FP-KNN	0.0795	0.0919	0.0595	0.0229
random (shuffle predictions)	0.0001 ± 0.0010	$6e-5 \pm 0.0005$	-0.0002 ± 0.0007	$-6e-5 \pm 0.0009$
		cycle split		
model	1+2	1+3	2+3	1+2+3
OH-FFNN	0.1414 ± 0.0069	0.0837 ± 0.0129	0.0805 ± 0.0141	0.0878 ± 0.0133
FP-FFNN	0.1134 ± 0.0015	0.0895 ± 0.0106	0.0850 ± 0.0063	0.0911 ± 0.0107
D-MPNN	0.1100 ± 0.0068	0.0793 ± 0.0087	0.0791 ± 0.0053	0.0828 ± 0.0158
OH-FFNN pt	0.1029 ± 0.0101	0.0569 ± 0.0107	0.0645 ± 0.0135	0.0733 ± 0.0135
FP-FFNN pt	0.0983 ± 0.0077	0.0527 ± 0.0120	0.0605 ± 0.0168	0.0567 ± 0.0192
D-MPNN pt	0.1012 ± 0.0009	0.0630 ± 0.0077	0.0551 ± 0.0079	0.0771 ± 0.0062
OH-KNN	0.0945	0.0467	0.0437	0.0559
FP-KNN	0.0759	0.0477	0.0386	0.0554
random (shuffle predictions)	0.0001 ± 0.0002	-0.0002 ± 0.0006	$5e-5 \pm 0.0007$	0.0002 ± 0.0005

Table S12: Rank correlation coefficients (mean \pm standard deviation) for regression models and baseline models on the triazine SIRT2 dataset. OH-FFNN, FP-FFNN, OH-FFNN pt, FP-FFNN pt, random (predict all ones), and random (shuffle predictions) results are averaged over five trials; D-MPNN and D-MPNN pt results are averaged over three trials; OH-KNN and FP-KNN results are single trials evaluated on a random 10% of the test set.

triazine SIRT2		cycle split		
model	random split	1	2	3
OH-FFNN	0.2207 ± 0.0040	0.1928 ± 0.0172	0.1625 ± 0.0284	0.1136 ± 0.0233
FP-FFNN	0.1974 ± 0.0023	0.1720 ± 0.0461	0.1002 ± 0.0279	0.0752 ± 0.0600
D-MPNN	0.1813 ± 0.0081	0.1706 ± 0.0087	0.1072 ± 0.0110	0.0278 ± 0.0195
OH-FFNN pt	0.0409 ± 0.0010	0.0275 ± 0.0093	0.0929 ± 0.0074	-0.0440 ± 0.0044
FP-FFNN pt	0.0616 ± 0.0012	0.0541 ± 0.0024	0.0785 ± 0.0094	0.0174 ± 0.0465
D-MPNN pt	0.0580 ± 0.0033	0.0515 ± 0.0076	0.0832 ± 0.0093	-0.0195 ± 0.0140
OH-KNN	0.0292	0.0399	0.0534	-0.0315
FP-KNN	0.0318	0.0384	0.0332	-0.0129
random (shuffle predictions)	0.0004 ± 0.0004	$1e-5 \pm 0.0005$	-0.0004 ± 0.0013	$8e-5 \pm 0.0009$
		cycle split		
model	1+2	1+3	2+3	1+2+3
OH-FFNN	0.1590 ± 0.0231	0.1373 ± 0.0237	0.1115 ± 0.0092	0.1073 ± 0.0199
FP-FFNN	0.1209 ± 0.0289	0.1197 ± 0.0462	0.0715 ± 0.0305	0.1032 ± 0.0315
D-MPNN	0.1051 ± 0.0078	0.1192 ± 0.0175	0.0624 ± 0.0424	0.0880 ± 0.0025
OH-FFNN pt	0.0639 ± 0.0030	-0.0179 ± 0.0097	0.0204 ± 0.0075	0.0201 ± 0.0112
FP-FFNN pt	0.0713 ± 0.0111	0.0261 ± 0.0224	0.0521 ± 0.0259	0.0460 ± 0.0128
D-MPNN pt	0.0657 ± 0.0070	0.0190 ± 0.0205	0.0312 ± 0.0266	0.0394 ± 0.0126
OH-KNN	0.0472	-0.0142	0.0057	0.0132
FP-KNN	0.0367	0.0094	0.0123	0.0224
random (shuffle predictions)	0.0002 ± 0.0006	0.0003 ± 0.0009	-0.0005 ± 0.0008	$-7e-5 \pm 0.0004$

S2.3 Comparison of predicted enrichments to 95% confidence intervals for the FP-FFNNs on all random splits of the DD1S CAIX dataset

Table S13: Comparison of test-set predicted enrichments to 95% confidence intervals (estimated from the count data) for the FP-FFNNs on all random splits of the DD1S CAIX dataset.

DD1S CAIX (random split)	
random seed	percentage of test-set predicted enrichments within 95% confidence interval
0	93.02%
1	92.82%
2	92.91%
3	92.93%
4	93.03%

S2.4 Parity plots to evaluate correlation between predicted and calculated enrichments

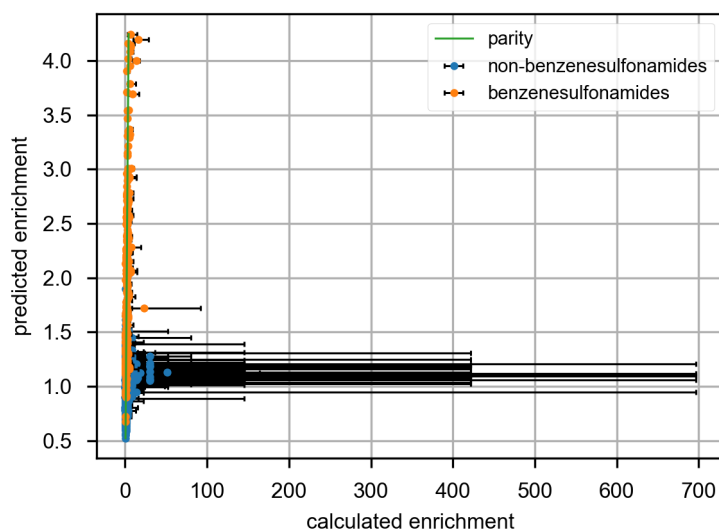


Figure S17: Full scatter plot of predicted and calculated enrichments for the test-set compounds of a FP-FFNN on a random split (*cf.* Figure 2d) of the DD1S CAIX dataset (as shown zoomed-in in Figure 4a). The green parity line is the identity function, for reference. Error bars represent 95% confidence intervals for calculated enrichments.

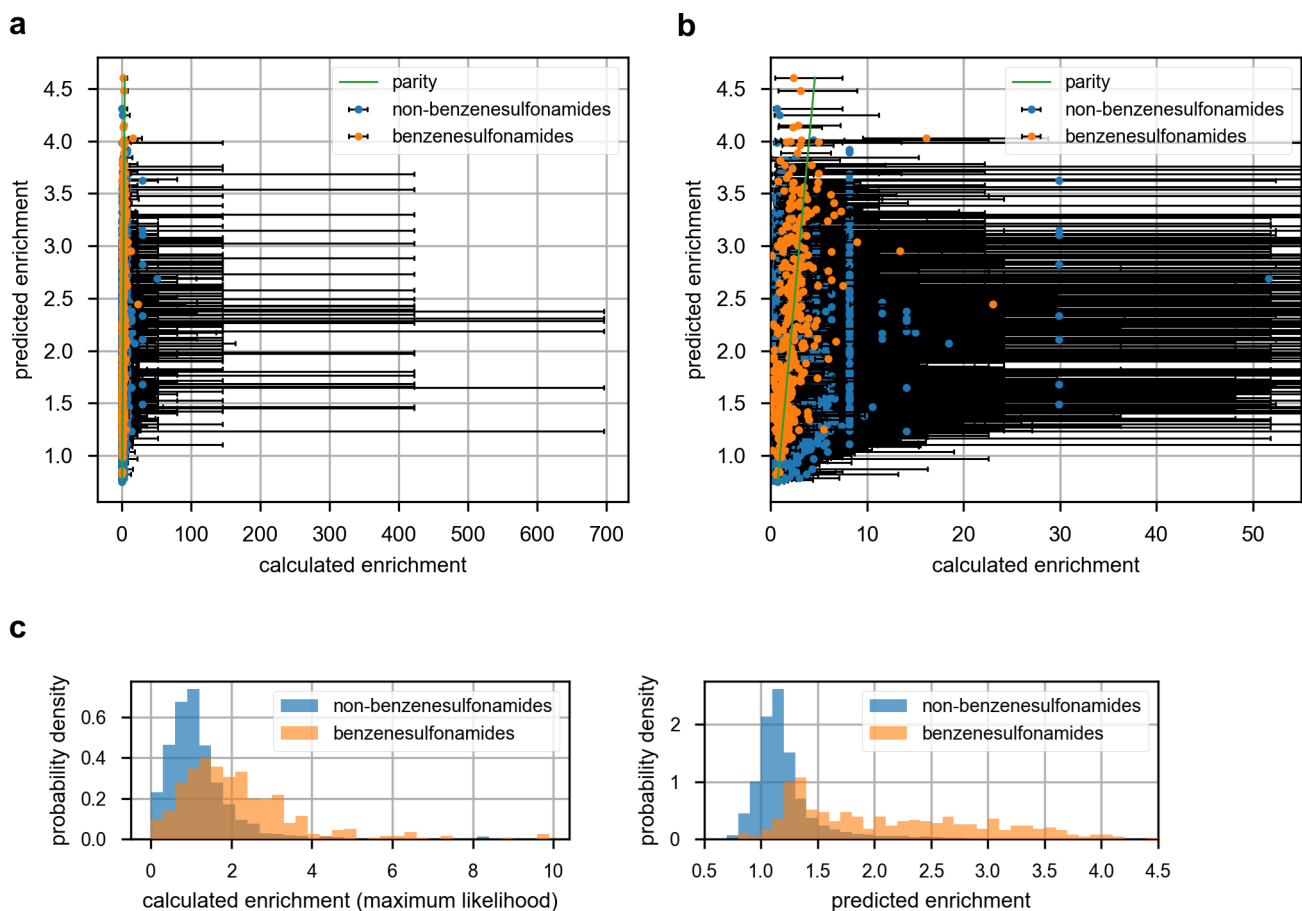


Figure S18: **(a)** Full and **(b)** zoomed-in scatter plot of predicted and calculated enrichments for the test-set compounds of a FP-FFNN pt model (trained using MSE loss) on a random split (*cf.* Figure 2d) of the DD1S CAIX dataset. The green parity line is the identity function, for reference. Error bars represent 95% confidence intervals for calculated enrichments. **(c)** Histograms of calculated and predicted enrichments for the test-set compounds of a FP-FFNN pt model on a random split (*cf.* Figure 2d) of the DD1S CAIX dataset. The horizontal axis cutoff of 10 in the histogram of calculated enrichments is arbitrary, for the sake of legibility.

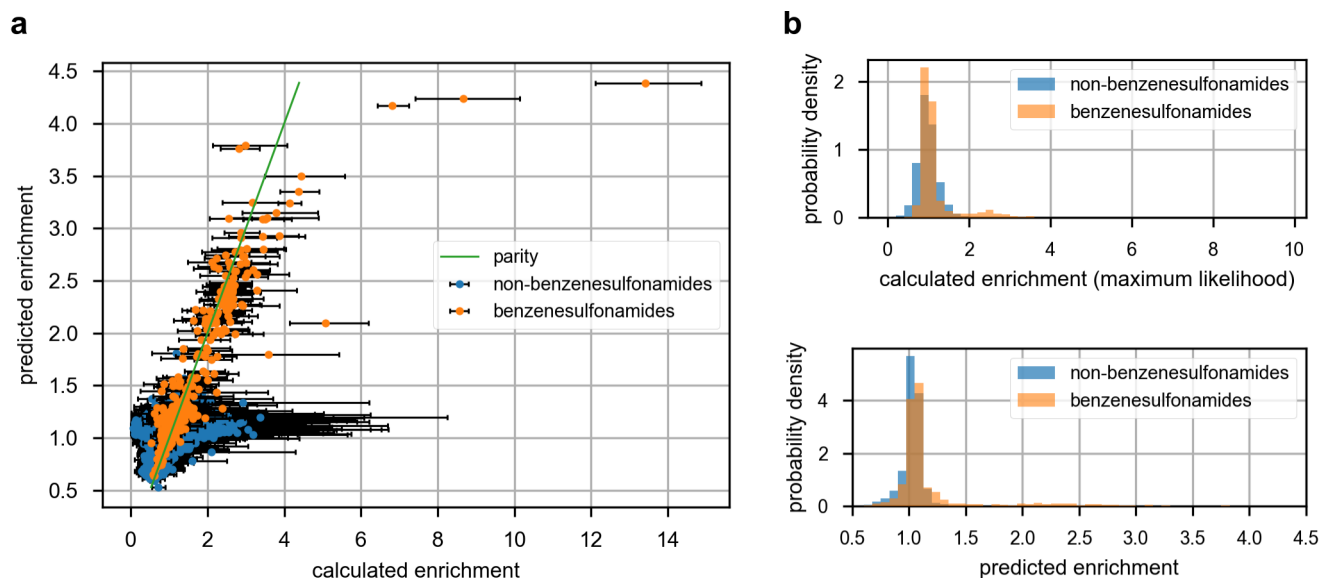


Figure S19: **(a)** Scatter plot of predicted and calculated enrichments for all disynths in the DD1S CAIX dataset, using the predictions of a FP-FFNN on a random split (*cf.* Figure 2d) of the DD1S CAIX dataset. **(b)** Histograms of calculated and predicted enrichments for all disynths in the DD1S CAIX dataset, using the predictions of a FP-FFNN on a random split (*cf.* Figure 2d) of the DD1S CAIX dataset.

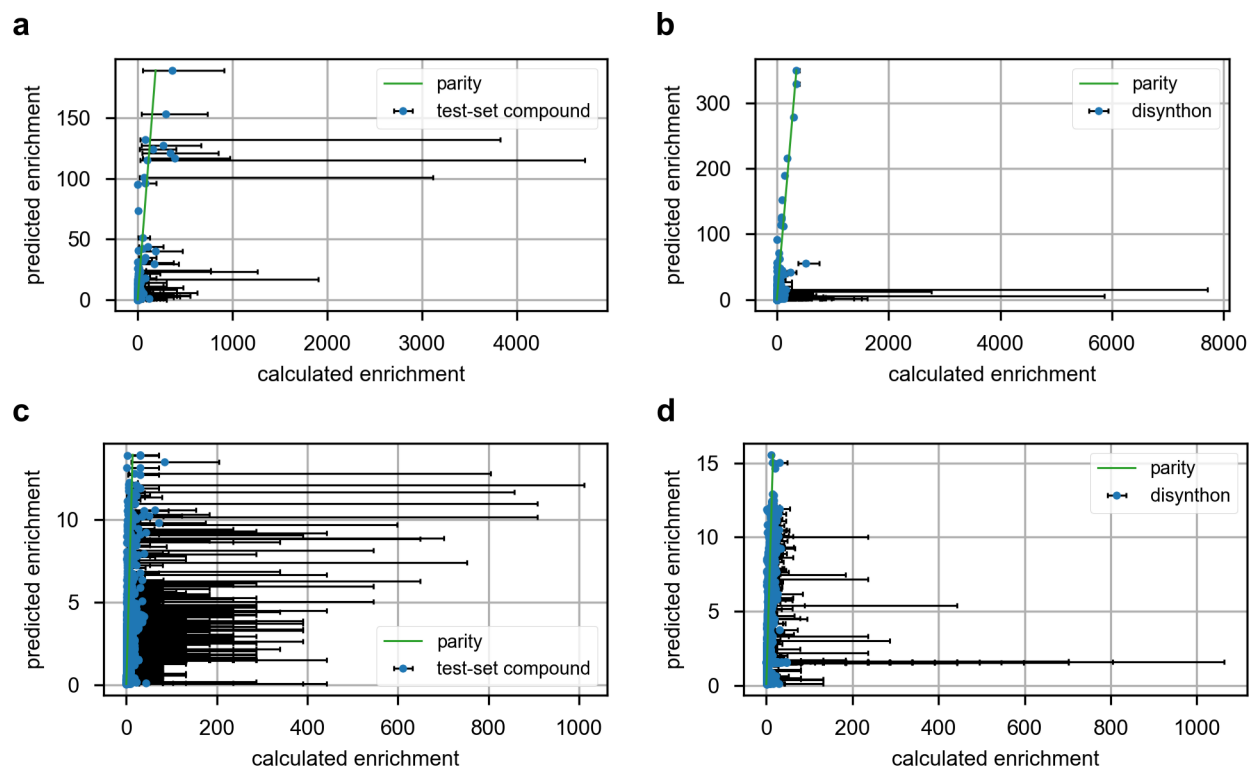


Figure S20: Full scatter plot of predicted and calculated enrichments for a subset (20,000 compounds) of the test set of a FP-FFNN on a random split (*cf.* Figure 2d) of the **(a)** triazine sEH, **(c)** triazine SIRT2 dataset, and for all disynths in the **(b)** triazine sEH, **(d)** triazine SIRT2 dataset (as shown zoomed-in in Figure 5). The green parity line is the identity function, for reference. Error bars represent 95% confidence intervals for calculated enrichments.

S2.5 Distributional shift in calculated enrichment for the DD1S CAIX dataset (cycle-2 split, seed 4)

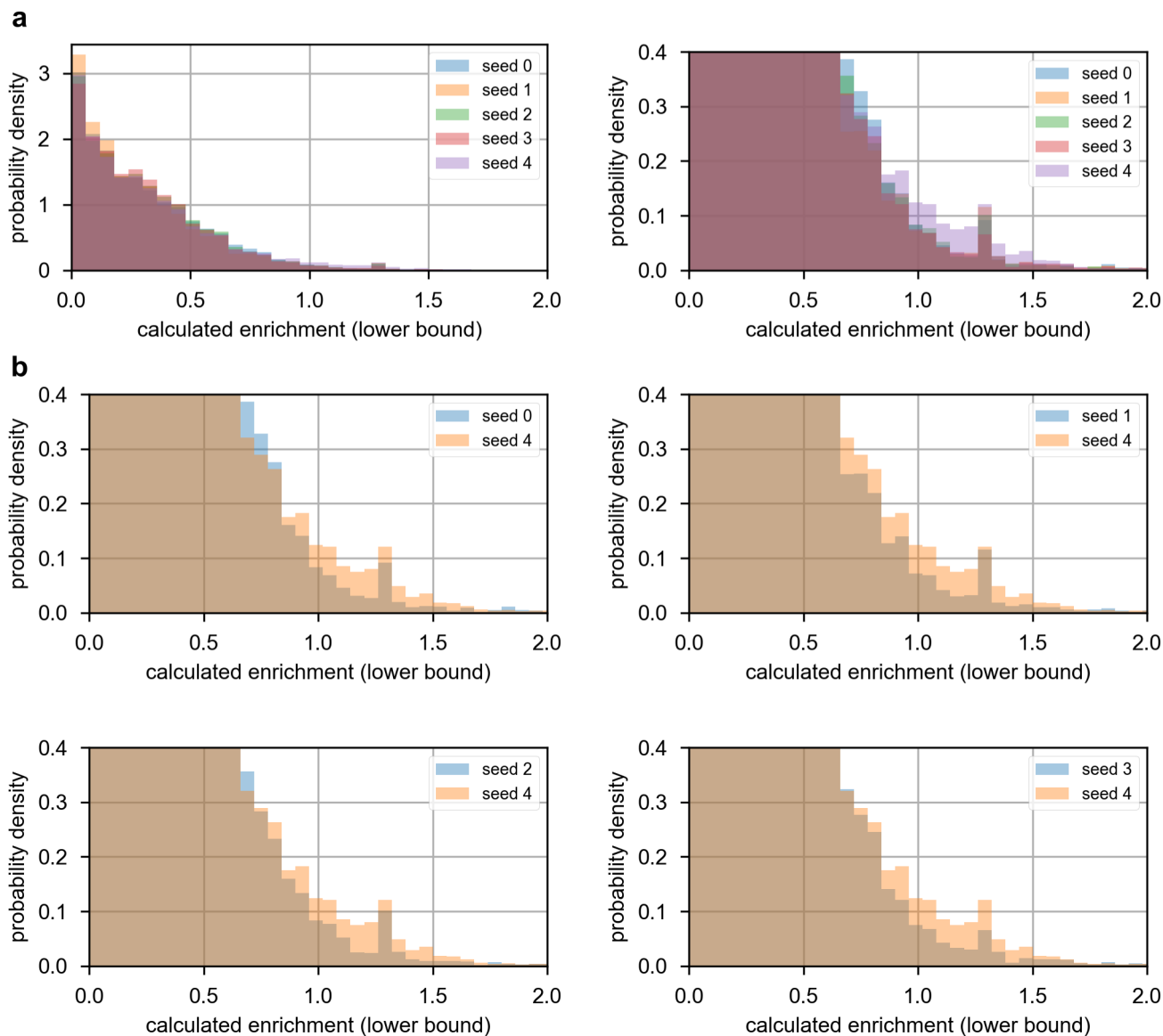


Figure S21: Histograms (full and zoomed-in) of the lower bound of calculated enrichment for the test set of the DD1S CAIX dataset split along cycle 2 (*cf.* Figure 2d). Each seed represents a cycle-2 split using a different random seed. (a) shows the overlaid distributions for all five splits; (b) shows individual comparisons of the distribution for the seed-4 split with the distribution for each of the other splits.

S2.6 Binary classification baseline comparisons (fixed threshold)

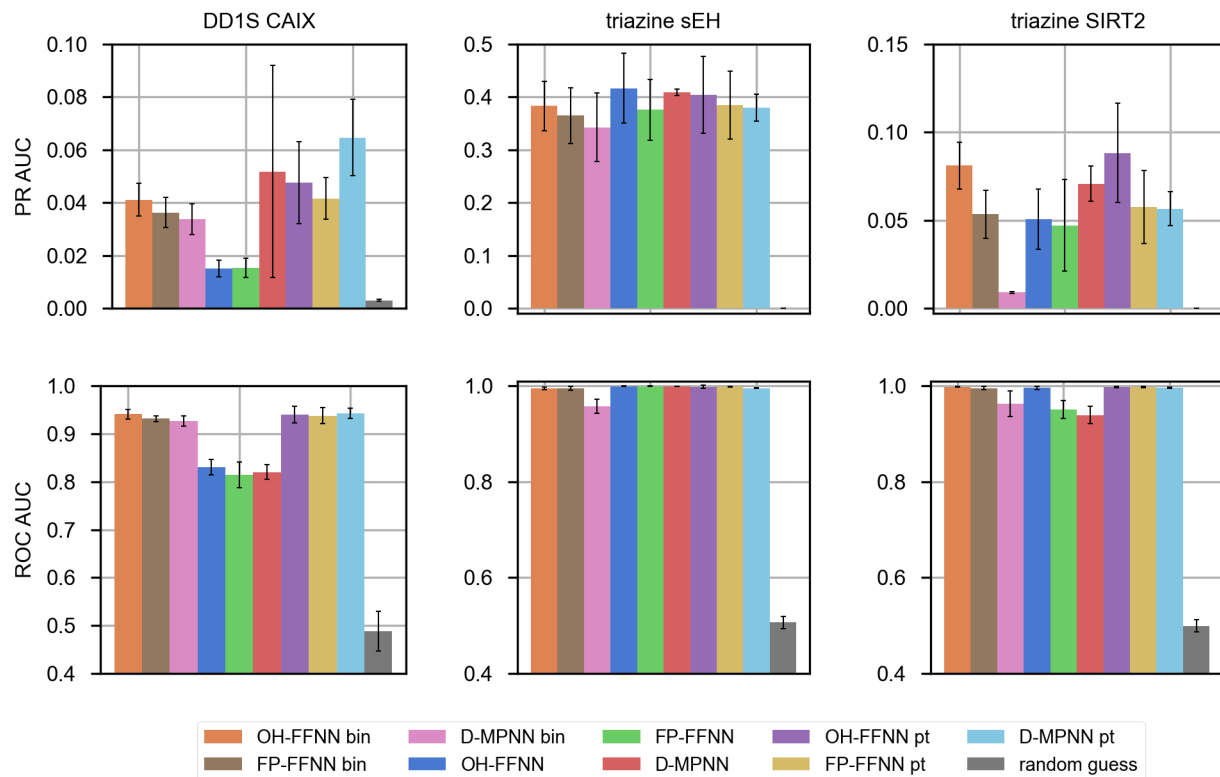


Figure S22: PR and ROC AUC scores (mean \pm standard deviation) for the binary classifiers ("bin") and regression models evaluated as classifiers, at fixed thresholds. The top 0.5% and 0.01% of compounds in the training set were defined as enriched for the DD1S CAIX and triazine datasets, respectively. OH-FFNN bin, FP-FFNN bin, OH-FFNN, FP-FFNN, OH-FFNN pt, FP-FFNN pt, and random guess results are averaged over five trials for each dataset; D-MPNN bin, D-MPNN, and D-MPNN pt results are averaged over five trials for the DD1S CAIX dataset and over three trials for the triazine sEH and triazine SIRT2 datasets. For each trial, the random-guess baseline was generated by randomly shuffling the predictions of the FP-FFNN for that trial.

Table S14: PR and ROC AUCs (mean \pm standard deviation) for the regression models, binary classifiers ("bin"), and baseline random-guess (random shuffling of the predictions of the FP-FFNNs) on the DD1S CAIX dataset. The top 0.5% of compounds in the training set were defined as enriched. Results are averaged over five trials.

DD1S CAIX (random split)		
model	PR AUC	ROC AUC
OH-FFNN	0.0150 ± 0.0032	0.8304 ± 0.0160
FP-FFNN	0.0153 ± 0.0036	0.8137 ± 0.0268
D-MPNN	0.0517 ± 0.0402	0.8202 ± 0.0155
OH-FFNN pt	0.0475 ± 0.0155	0.9401 ± 0.0170
FP-FFNN pt	0.0416 ± 0.0079	0.9375 ± 0.0170
D-MPNN pt	0.0646 ± 0.0144	0.9428 ± 0.0106
OH-FFNN bin	0.0411 ± 0.0062	0.9409 ± 0.0101
FP-FFNN bin	0.0362 ± 0.0058	0.9312 ± 0.0064
D-MPNN bin	0.0337 ± 0.0058	0.9264 ± 0.0105
random guess	0.0030 ± 0.0003	0.4878 ± 0.0413

Table S15: PR and ROC AUCs (mean \pm standard deviation) for the regression models, binary classifiers (“bin”), and baseline random-guess (random shuffling of the predictions of the FP-FFNNs) on the triazine sEH dataset. The top 0.01% of compounds in the training set were defined as enriched. OH-FFNN bin, FP-FFNN bin, OH-FFNN, FP-FFNN, OH-FFNN pt, FP-FFNN pt, and random guess results are averaged over five trials; D-MPNN bin, D-MPNN, and D-MPNN pt results are averaged over three trials.

triazine sEH (random split)		
model	PR AUC	ROC AUC
OH-FFNN	0.4168 ± 0.0660	0.9997 ± 0.0003
FP-FFNN	0.3757 ± 0.0581	0.9997 ± 0.0003
D-MPNN	0.4087 ± 0.0058	$0.9998 \pm 4e-5$
OH-FFNN pt	0.4042 ± 0.0729	0.9981 ± 0.0031
FP-FFNN pt	0.3845 ± 0.0641	0.9990 ± 0.0007
D-MPNN pt	0.3800 ± 0.0258	0.9956 ± 0.0007
OH-FFNN bin	0.3832 ± 0.0471	0.9952 ± 0.0030
FP-FFNN bin	0.3649 ± 0.0531	0.9953 ± 0.0036
D-MPNN bin	0.3426 ± 0.0649	0.9578 ± 0.0144
random guess	$0.0001 \pm 2e-5$	0.5065 ± 0.0125

Table S16: PR and ROC AUCs (mean \pm standard deviation) for the regression models, binary classifiers (“bin”), and baseline random-guess (random shuffling of the predictions of the FP-FFNNs) on the triazine SIRT2 dataset. The top 0.01% of compounds in the training set were defined as enriched. OH-FFNN bin, FP-FFNN bin, OH-FFNN, FP-FFNN, OH-FFNN pt, FP-FFNN pt, and random guess results are averaged over five trials; D-MPNN bin, D-MPNN, and D-MPNN pt results are averaged over three trials.

triazine SIRT2 (random split)		
model	PR AUC	ROC AUC
OH-FFNN	0.0506 ± 0.0172	0.9965 ± 0.0033
FP-FFNN	0.0471 ± 0.0260	0.9509 ± 0.0187
D-MPNN	0.0708 ± 0.0099	0.9393 ± 0.0180
OH-FFNN pt	0.0883 ± 0.0283	0.9984 ± 0.0012
FP-FFNN pt	0.0575 ± 0.0207	0.9977 ± 0.0010
D-MPNN pt	0.0566 ± 0.0096	0.9966 ± 0.0014
OH-FFNN bin	0.0811 ± 0.0134	0.9985 ± 0.0008
FP-FFNN bin	0.0535 ± 0.0136	0.9956 ± 0.0032
D-MPNN bin	0.0090 ± 0.0006	0.9629 ± 0.0263
random guess	$8e-5 \pm 1e-5$	0.4991 ± 0.0127

S2.7 Binary classification baseline comparisons (multiple thresholds)

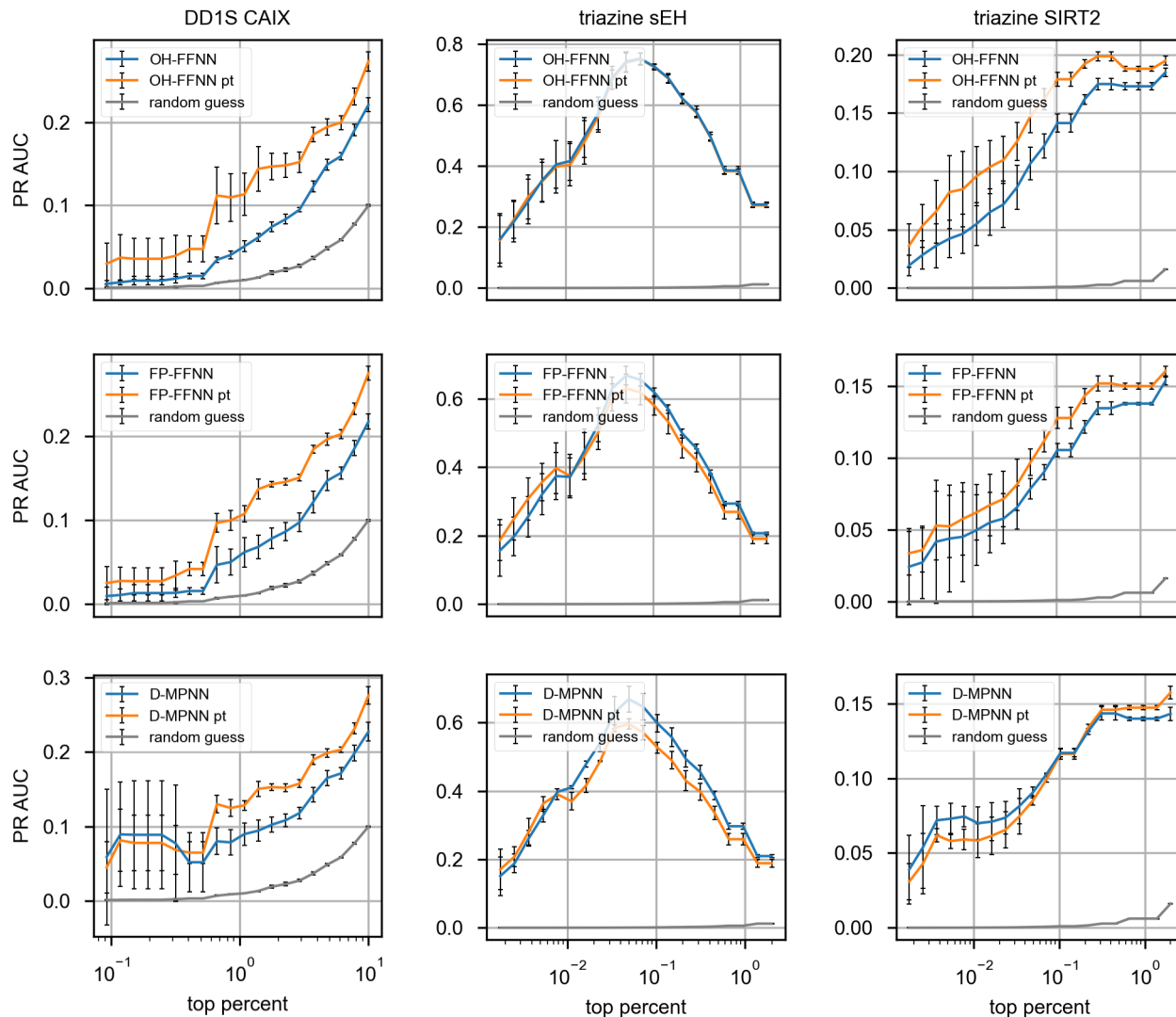


Figure S23: PR AUC scores (mean \pm standard deviation) for the regression models evaluated as classifiers, at various thresholds defined by the percentage of compounds in the training set considered to be enriched. OH-FFNN, FP-FFNN, OH-FFNN pt, FP-FFNN pt, and random guess results are averaged over five trials for each dataset; D-MPNN and D-MPNN pt results are averaged over five trials for the DD1S CAIX dataset and over three trials for the triazine sEH and triazine SIRT2 datasets. For each trial, the random-guess baseline was generated by randomly shuffling the predictions of the FP-FFNN for that trial.

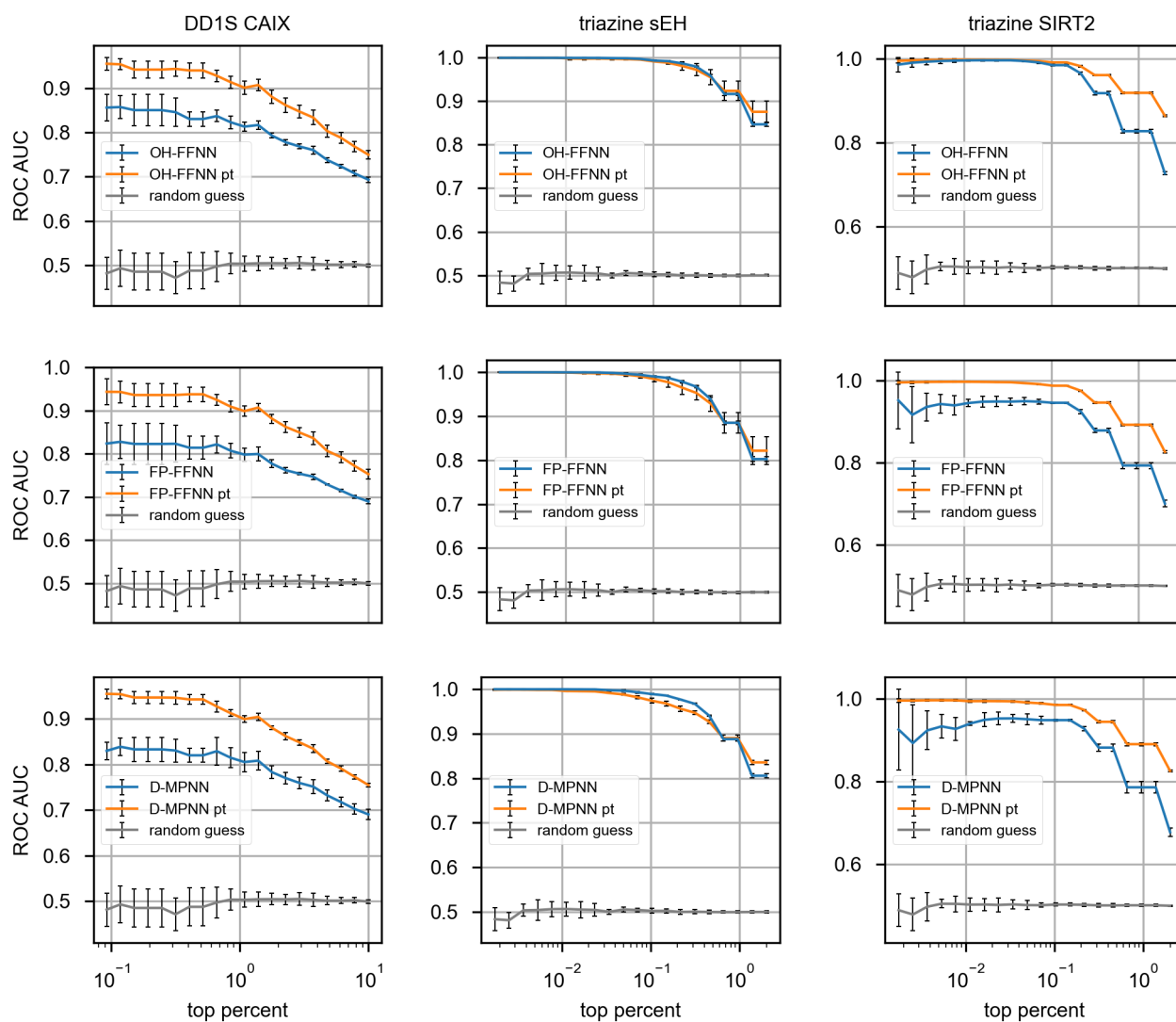


Figure S24: ROC AUC scores (mean \pm standard deviation) for the regression models evaluated as classifiers, at various thresholds defined by the percentage of compounds in the training set considered to be enriched. OH-FFNN, FP-FFNN, OH-FFNN pt, FP-FFNN pt, and random guess results are averaged over five trials for each dataset; D-MPNN and D-MPNN pt results are averaged over five trials for the DD1S CAIX dataset and over three trials for the triazine sEH and triazine SIRT2 datasets. For each trial, the random-guess baseline was generated by randomly shuffling the predictions of the FP-FFNN for that trial.

S2.8 2D histograms of predicted vs. calculated enrichment

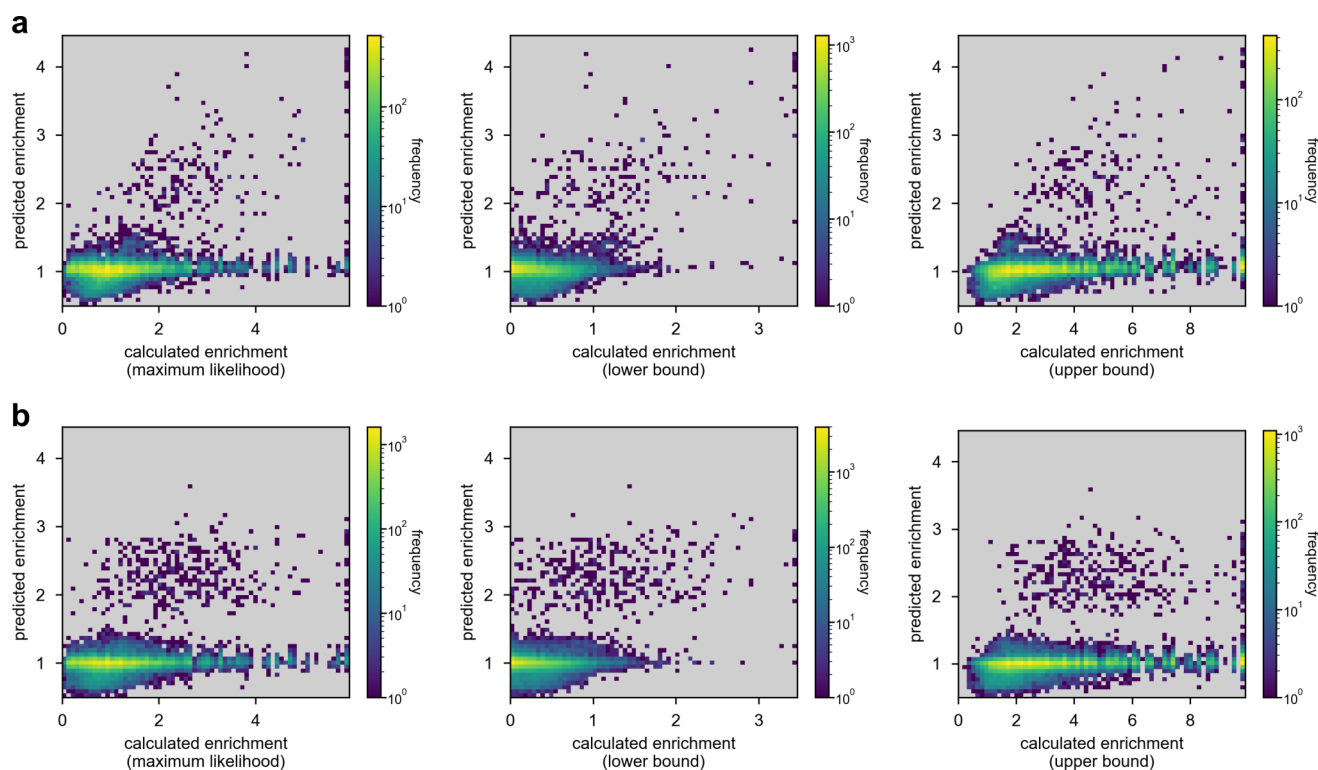


Figure S25: Histograms of calculated and predicted enrichments for the test-set compounds of a FP-FFNN on a (a) random split and (b) cycle-1+2 split (*cf.* Figure 2d) of the DD1S CAIX dataset, excluding compounds for which the sum of the experimental and beads counts is less than 3.

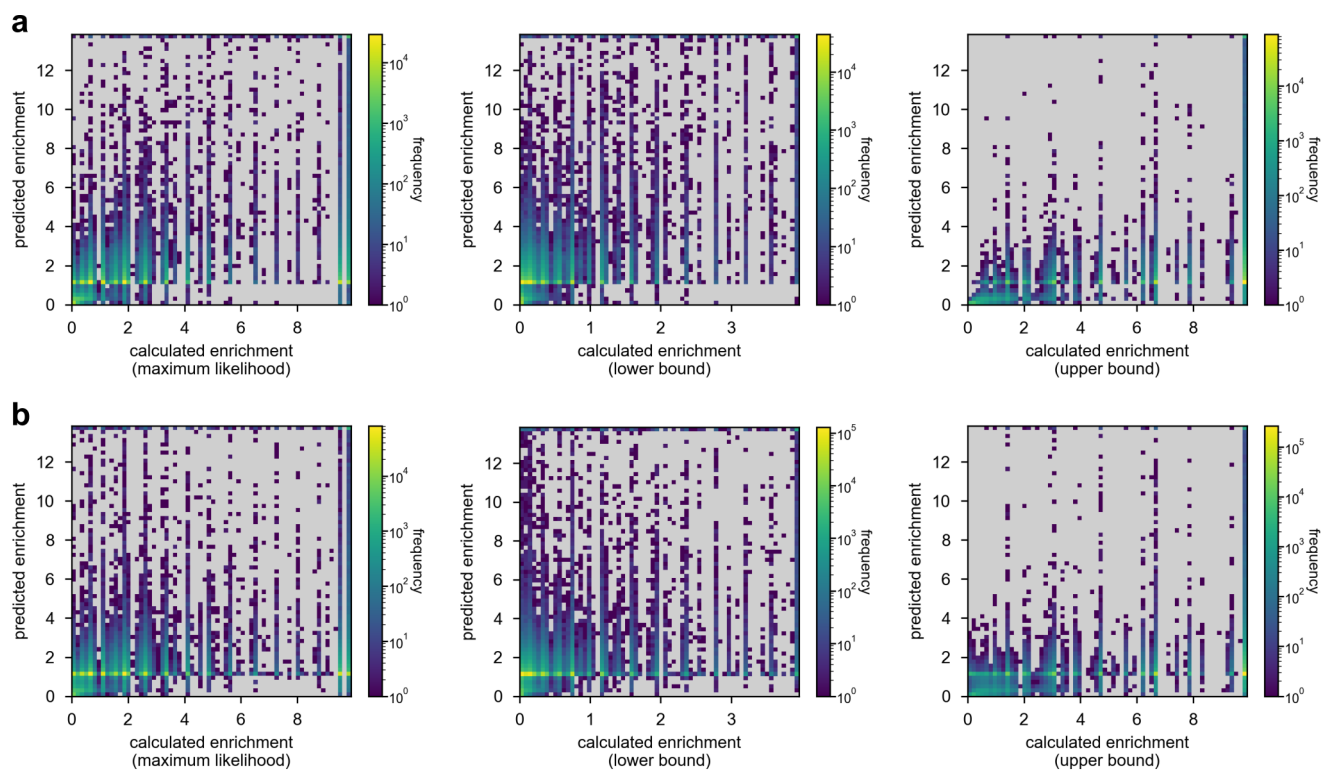


Figure S26: Histograms of calculated and predicted enrichments for the test-set compounds of a FP-FFNN on a **(a)** random split and **(b)** cycle-1+2+3 split (*cf.* Figure 2d) of the triazine sEH dataset, excluding compounds for which the sum of the experimental and beads counts is less than 3.

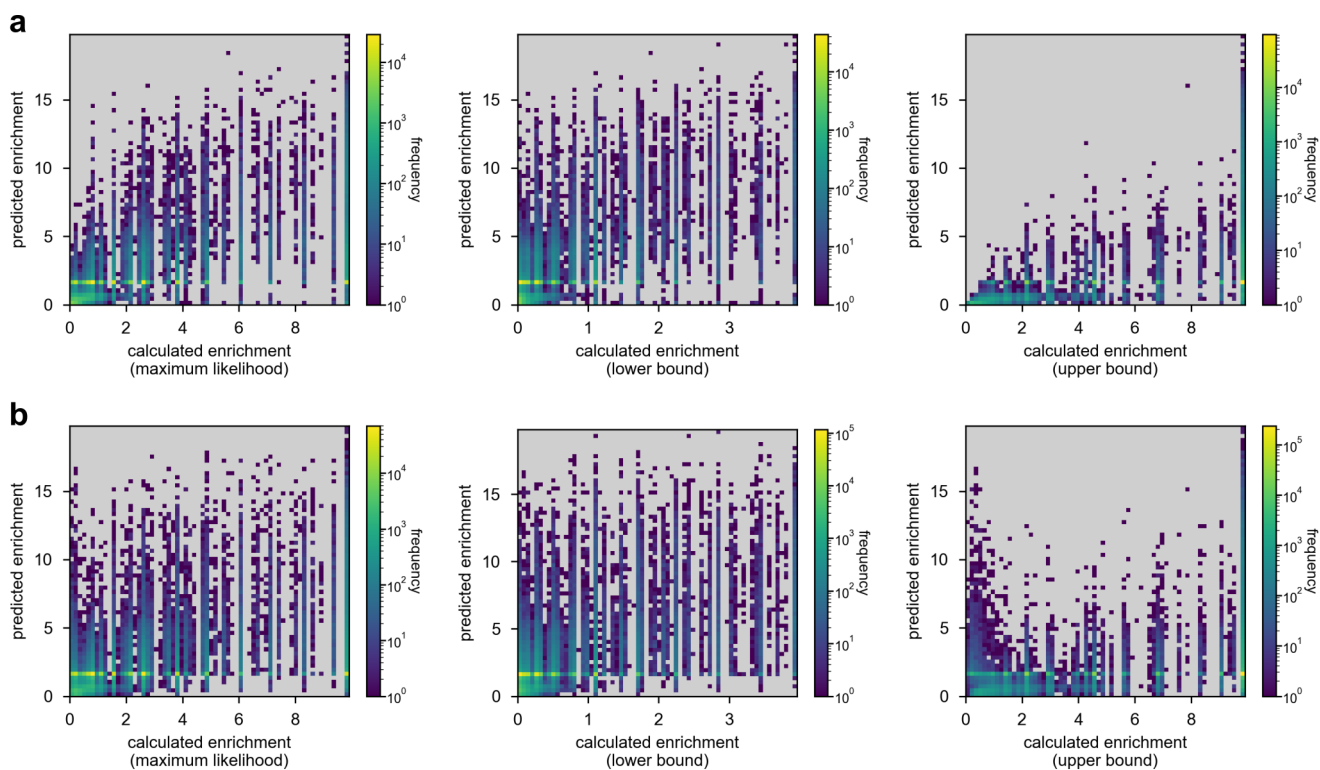


Figure S27: Histograms of calculated and predicted enrichments for the test-set compounds of a FP-FFNN on a **(a)** random split and **(b)** cycle-1+2+3 split (*cf.* Figure 2d) of the triazine SIRT2 dataset, excluding compounds for which the sum of the experimental and beads counts is less than 3.

In the above histograms, one would expect linear correlation between the predicted and calculated enrichments, with better correlation for the models trained on a random split (evaluating interpolation) than for models trained on a cycle split (evaluating generalization). However, such a trend is not apparent in the plots. One possibility is that a linear correlation is present but obscured by noise, for instance due to compounds with relatively low counts. For example, in each of the plots for the DD1S CAIX dataset (Figure S25), the mass of datapoints at a predicted enrichment of about 1 may be attributed to noise. However, it is difficult to validate this hypothesis in the absence of ground truth enrichment values (these would come from experimental validation of the compounds). For the plot of predicted enrichment versus upper bound of calculated enrichment for a random split of the triazine SIRT2 dataset (Figure S27a), the fact that most of the datapoints fall below the parity line indicates that the model is not grossly overestimating enrichment.

S2.9 Bit and substructure importance

S2.9.1 Single-substructure analysis

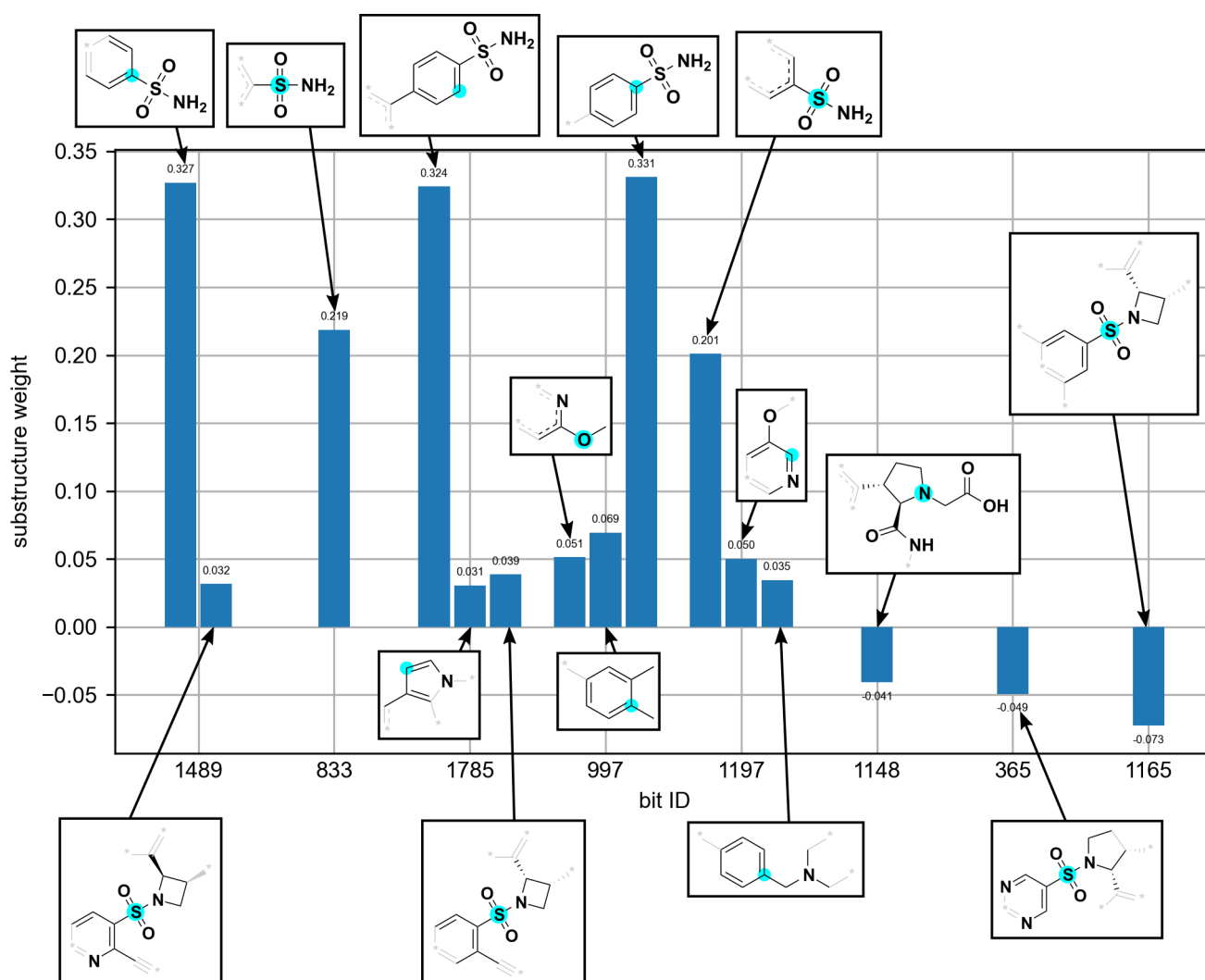
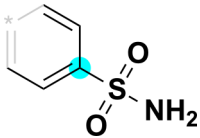
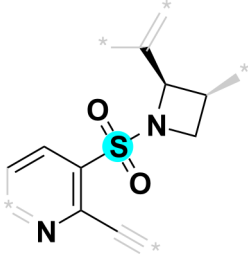
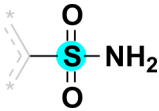
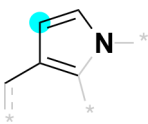
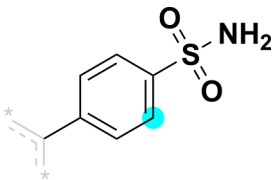


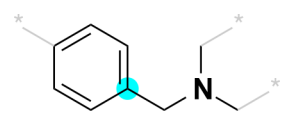
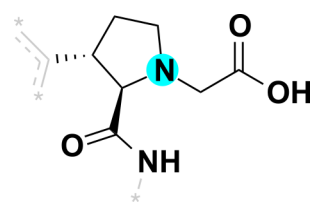
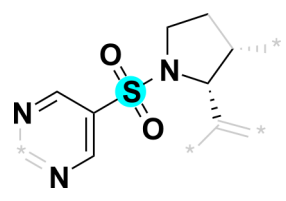
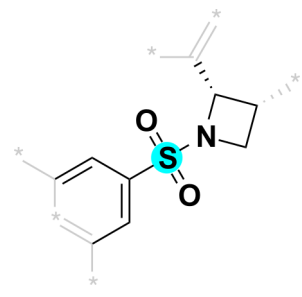
Figure S28: Single-substructure analysis on the DD1S CAIX dataset (random split, seed 0; *cf.* Figure 2d), including substructures mapped to the top 5 and bottom 3 bits.

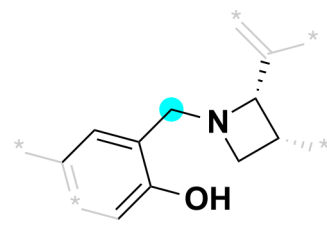
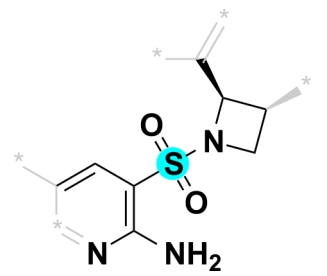
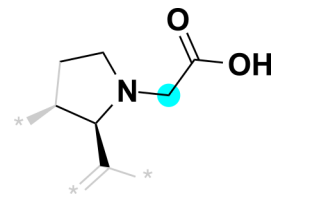
Table S17: SMARTS for single-substructure analysis on the DD1S CAIX dataset (random split; seeds 0, 1, 2). The substructures for the different replicates differ only in the ones mapped to a few of the bottom bits; all substructures across all replicates are included below.

bit ID	substructure example	SMARTS
--------	----------------------	--------

1489		$[\#6;D2;H1;R1;+0]:[\#6;D2;H1;R1;+0]:$ $[\#6;D3;H0;R1;+0](:[\#6;D2;H1;R1;+0]:$ $[\#6;D2;H1;R1;+0])-[\#16;D4;H0;R0;+0]$ $(-[\#7;D1;H2;R0;+0])(=[\#8;D1;H0;R0;+0])$ $=[\#8;D1;H0;R0;+0]$
1489		$[\#6;D2;H0;R0;+0]-[\#6;D3;H0;R1;+0]$ $(:[\#7;D2;H0;R1;+0]):[\#6;D3;H0;R1;+0]$ $(:[\#6;D2;H1;R1;+0]:[\#6;D2;H1;R1;+0])-$ $[\#16;D4;H0;R0;+0](=[\#8;D1;H0;R0;+0])$ $(=[\#8;D1;H0;R0;+0])-[\#7;D3;H0;R1;+0]1-$ $[\#6;D2;H2;R1;+0]-[\#6;D3;H1;R1;+0]-$ $[\#6;D3;H1;R1;+0]1-[\#6;D3;H0;R0;+0]$
833		$[\#6;D3;H0;R1;+0]-[\#16;D4;H0;R0;+0](-$ $[\#7;D1;H2;R0;+0])(=[\#8;D1;H0;R0;+0])$ $=[\#8;D1;H0;R0;+0]$
1785		$[\#6;D2;H1;R1;+0]:[\#6;D3;H0;R2;+0]$ $(:[\#6;D3;H0;R2;+0]):[\#6;D2;H1;R1;+0]:$ $[\#6;D2;H1;R1;+0]:[\#7;D3;H0;R1;+0]$
1785		$[\#6;D3;H0;R1;+0]-[\#6;D3;H0;R1;+0]1:$ $[\#6;D2;H1;R1;+0]:[\#6;D2;H1;R1;+0]:$ $[\#6;D3;H0;R1;+0](-[\#16;D4;H0;R0;+0](-$ $[\#7;D1;H2;R0;+0])(=[\#8;D1;H0;R0;+0])$ $=[\#8;D1;H0;R0;+0]):[\#6;D2;H1;R1;+0]:$ $[\#6;D2;H1;R1;+0]:1$

1785		$[#6;D2;H0;R0;+0]-[#6;D3;H0;R1;+0]$ $(:[#6;D2;H1;R1;+0]):[#6;D3;H0;R1;+0]$ $(:[#6;D2;H1;R1;+0]:[#6;D2;H1;R1;+0])-$ $[#16;D4;H0;R0;+0](=[#8;D1;H0;R0;+0])$ $(=[#8;D1;H0;R0;+0])-[#7;D3;H0;R1;+0]1-$ $[#6;D2;H2;R1;+0]-[#6;D3;H1;R1;+0]-$ $[#6;D3;H1;R1;+0]1-[#6;D3;H0;R0;+0]$
997		$[#6;D1;H3;R0;+0]-[#6;D3;H0;R1;+0]1:$ $[#6;D2;H1;R1;+0]:[#6;D2;H1;R1;+0]:$ $[#6;D3;H0;R1;+0]:[#6;D2;H1;R1;+0]:$ $[#6;D3;H0;R1;+0]:1-[#6;D1;H3;R0;+0]$
997		$[#6;D1;H3;R0;+0]-[#8;D2;H0;R0;+0]-$ $[#6;D3;H0;R1;+0]([#6;D2;H1;R1;+0]):$ $[#7;D2;H0;R1;+0]$
997		$[#7;D1;H2;R0;+0]-[#16;D4;H0;R0;+0]$ $(=[#8;D1;H0;R0;+0])(=[#8;D1;H0;R0;+0])-$ $[#6;D3;H0;R1;+0]1:[#6;D2;H1;R1;+0]:$ $[#6;D2;H1;R1;+0]:[#6;D3;H0;R1;+0]:$ $[#6;D2;H1;R1;+0]:[#6;D2;H1;R1;+0]:1$
1197		$[#6;D2;H1;R1;+0]:[#6;D3;H0;R1;+0]$ $(:[#6;D2;H1;R1;+0])-[#16;D4;H0;R0;+0]$ $(-[#7;D1;H2;R0;+0])(=[#8;D1;H0;R0;+0])$ $=[#8;D1;H0;R0;+0]$
1197		$[#6;D2;H1;R1;+0]:[#7;D2;H0;R1;+0]:$ $[#6;D2;H1;R1;+0]:[#6;D3;H0;R1;+0]$ $(:[#6;D2;H1;R1;+0])-[#8;D2;H0;R0;+0]$

1197		$[\#6;D2;H2;R0;+0]-[\#7;D3;H0;R0;+0]$ $(-[\#6;D2;H2;R0;+0])-[\#6;D2;H2;R0;+0]-$ $[\#6;D3;H0;R1;+0]1:[\#6;D2;H1;R1;+0]:$ $[\#6;D2;H1;R1;+0]:[\#6;D3;H0;R1;+0]:$ $[\#6;D2;H1;R1;+0]:[\#6;D2;H1;R1;+0]:1$
1148		$[\#6;D3;H0;R1;+0]-[\#6;D3;H1;R1;+0]1-$ $[\#6;D2;H2;R1;+0]-[\#6;D2;H2;R1;+0]-$ $[\#7;D3;H0;R1;+0](-[\#6;D2;H2;R0;+0]-$ $[\#6;D3;H0;R0;+0](=[\#8;D1;H0;R0;+0])-$ $[\#8;D1;H1;R0;+0])-[\#6;D3;H1;R1;+0]-1-$ $[\#6;D3;H0;R0;+0](-[\#7;D2;H1;R0;+0])=$ $[\#8;D1;H0;R0;+0]$
365		$[\#6;D2;H2;R1;+0]-[\#6;D2;H2;R1;+0]-$ $[\#7;D3;H0;R1;+0](-[\#6;D3;H1;R1;+0](-$ $[\#6;D3;H0;R0;+0])-[\#6;D3;H1;R1;+0])-$ $[\#16;D4;H0;R0;+0](=[\#8;D1;H0;R0;+0])$ $(=[\#8;D1;H0;R0;+0])-[\#6;D3;H0;R1;+0](:$ $[\#6;D2;H1;R1;+0]:[\#7;D2;H0;R1;+0]):$ $[\#6;D2;H1;R1;+0]:[\#7;D2;H0;R1;+0]$
1165		$[\#6;D3;H0;R0;+0]-[\#6;D3;H1;R1;+0]1-$ $[\#6;D3;H1;R1;+0]-[\#6;D2;H2;R1;+0]-$ $[\#7;D3;H0;R1;+0]-1-[\#16;D4;H0;R0;+0](=$ $[\#8;D1;H0;R0;+0])(=[\#8;D1;H0;R0;+0])-$ $[\#6;D3;H0;R1;+0](:[\#6;D2;H1;R1;+0]:$ $[\#6;D3;H0;R1;+0]):[\#6;D2;H1;R1;+0]:$ $[\#6;D3;H0;R1;+0]$

1736		[#6;D2;H1;R1;+0]:[#6;D3;H0;R1;+0](- [#8;D1;H1;R0;+0]):[#6;D3;H0;R1;+0]([#6;D2;H1;R1;+0]:[#6;D3;H0;R1;+0])- [#6;D2;H2;R0;+0]-[#7;D3;H0;R1;+0]1- [#6;D2;H2;R1;+0]-[#6;D3;H1;R1;+0]- [#6;D3;H1;R1;+0]-1-[#6;D3;H0;R0;+0]
258		[#6;D3;H0;R0;+0]-[#6;D3;H1;R1;+0]1- [#6;D3;H1;R1;+0]-[#6;D2;H2;R1;+0]- [#7;D3;H0;R1;+0]-1-[#16;D4;H0;R0;+0](= [#8;D1;H0;R0;+0])(=[#8;D1;H0;R0;+0])- [#6;D3;H0;R1;+0](:[#6;D2;H1;R1;+0]: [#6;D3;H0;R1;+0]):[#6;D3;H0;R1;+0](- [#7;D1;H2;R0;+0]):[#7;D2;H0;R1;+0]
1844		[#6;D2;H2;R1;+0]-[#6;D2;H2;R1;+0]- [#7;D3;H0;R1;+0](-[#6;D2;H2;R0;+0]- [#6;D3;H0;R0;+0])(=[#8;D1;H0;R0;+0])- [#8;D1;H1;R0;+0]-[#6;D3;H1;R1;+0](- [#6;D3;H0;R0;+0])-[#6;D3;H1;R1;+0]

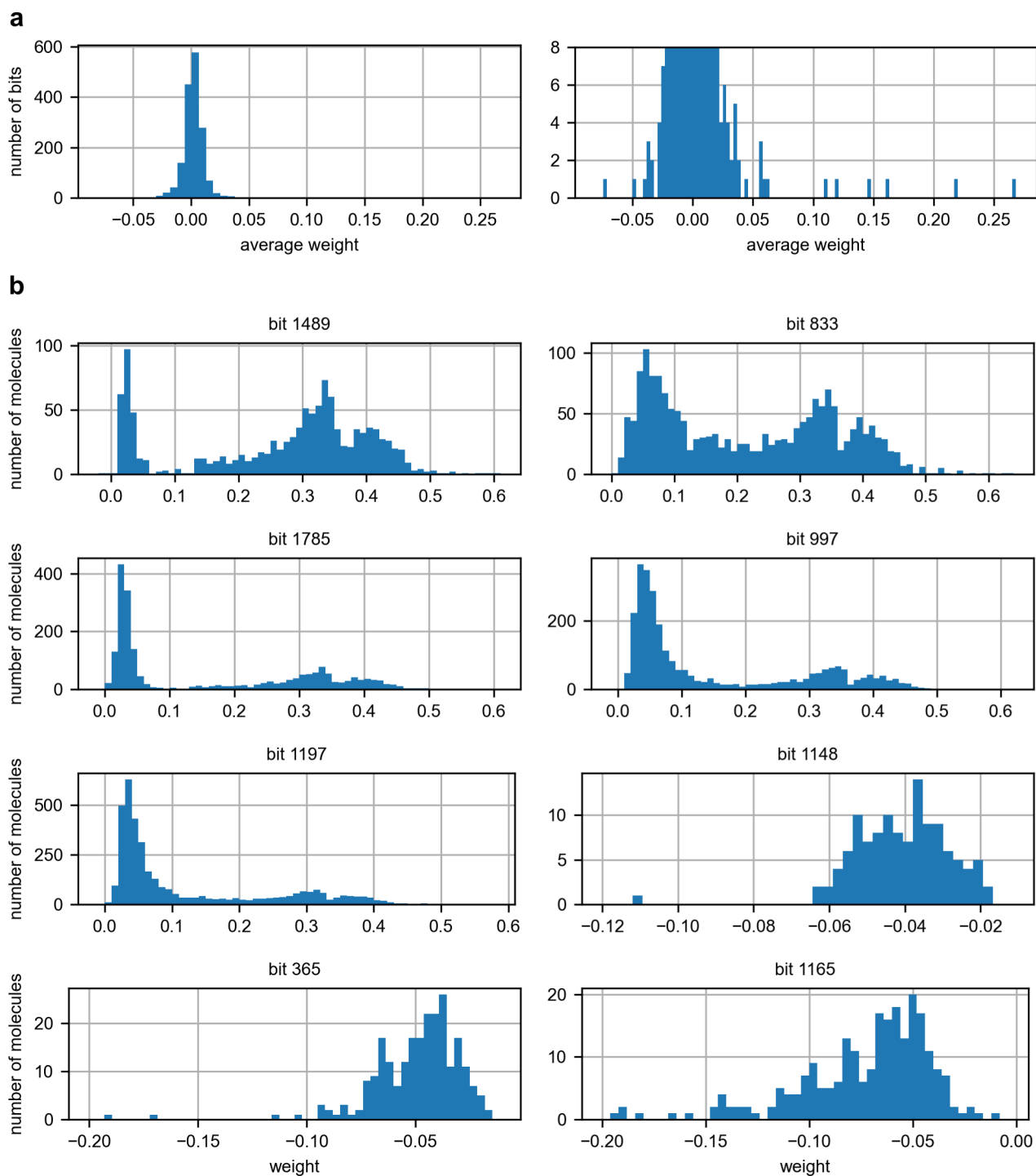


Figure S29: Histograms of **(a)** bit weights (only including bits set by at least one molecule in the dataset; plot shown in full and zoomed in) and **(b)** molecule-level bit weights for single-substructure analysis on the DD1S CAIX dataset (random split, seed 0; cf. Figure 2d), including the top 5 and bottom 3 bits.

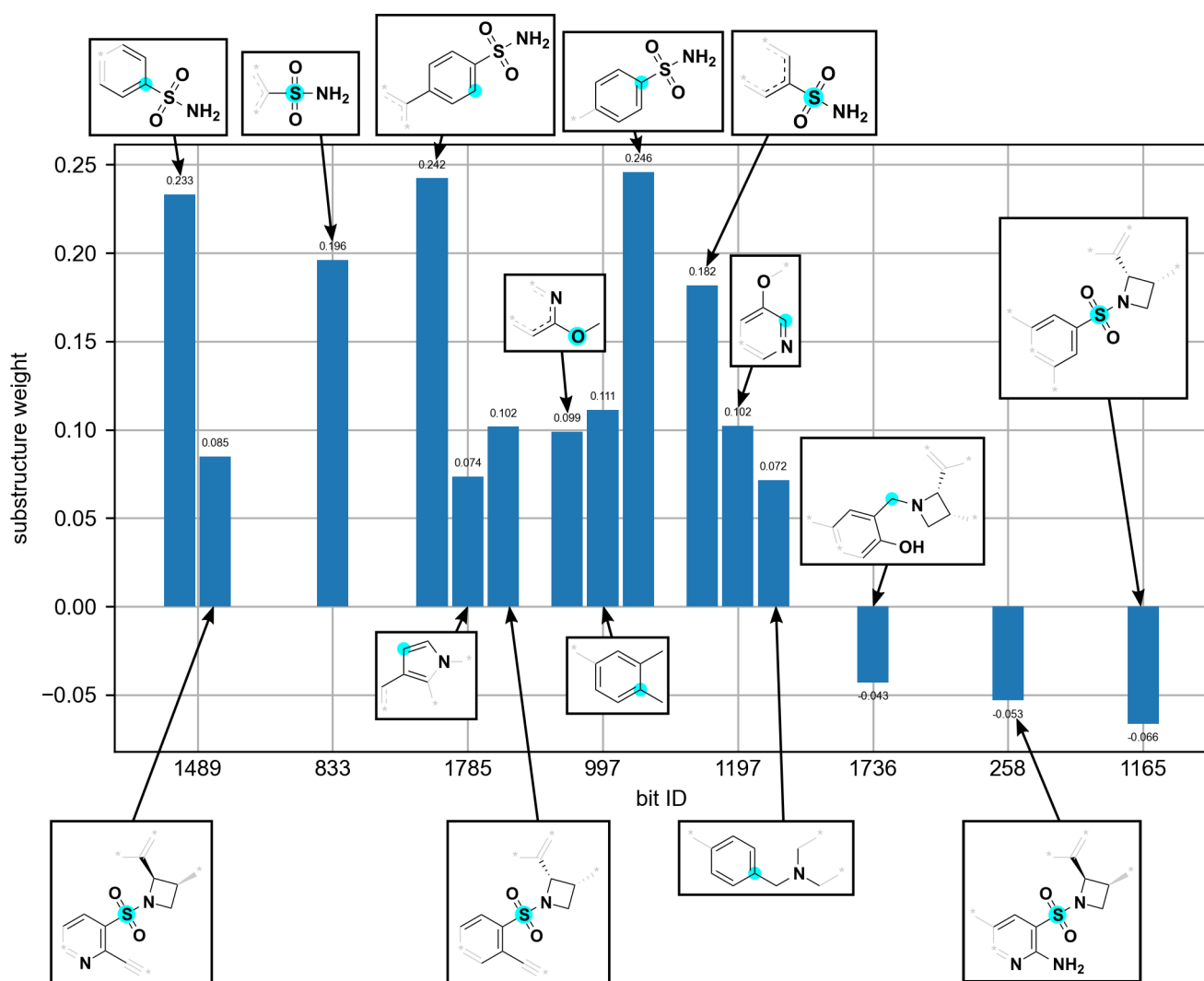


Figure S30: Single-substructure analysis on the DD1S CAIX dataset (random split, seed 1; *cf.* Figure 2d), including substructures mapped to the top 5 and bottom 3 bits.

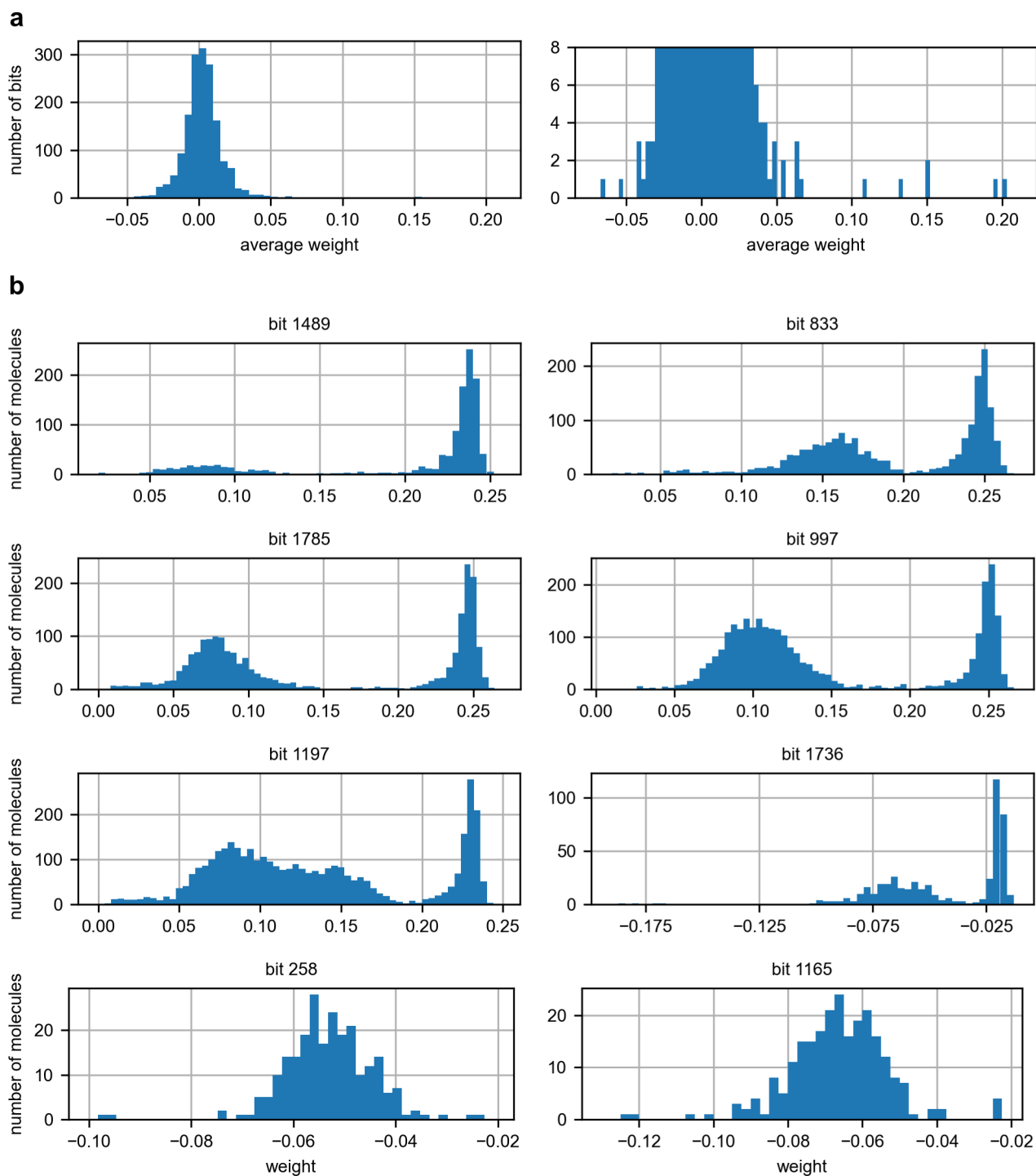


Figure S31: Histograms of **(a)** bit weights (only including bits set by at least one molecule in the dataset; plot shown in full and zoomed in) and **(b)** molecule-level bit weights for single-substructure analysis on the DD1S CAIX dataset (random split, seed 1; *cf.* Figure 2d), including the top 5 and bottom 3 bits.

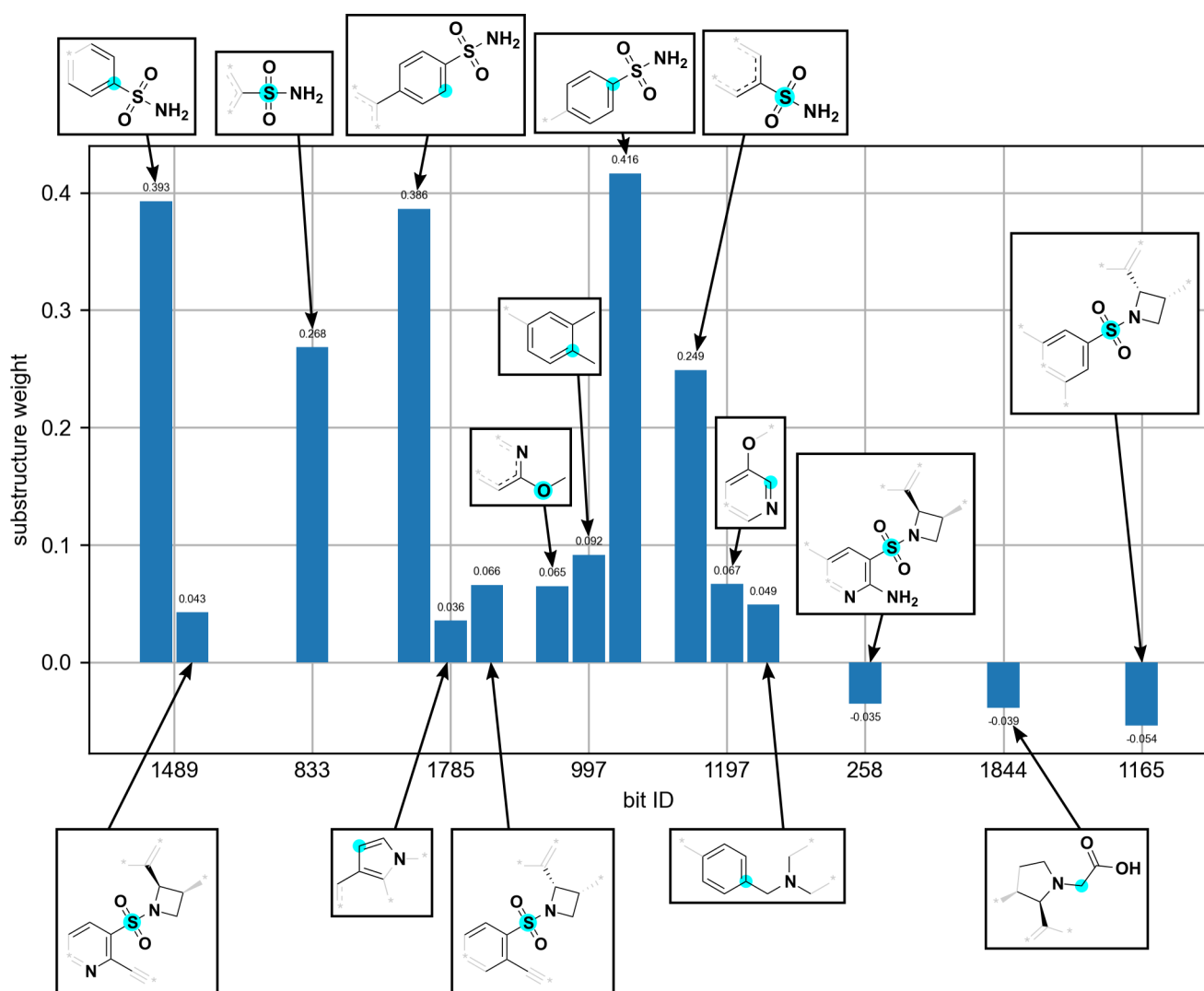


Figure S32: Single-substructure analysis on the DD1S CAIX dataset (random split, seed 2; *cf.* Figure 2d), including substructures mapped to the top 5 and bottom 3 bits.

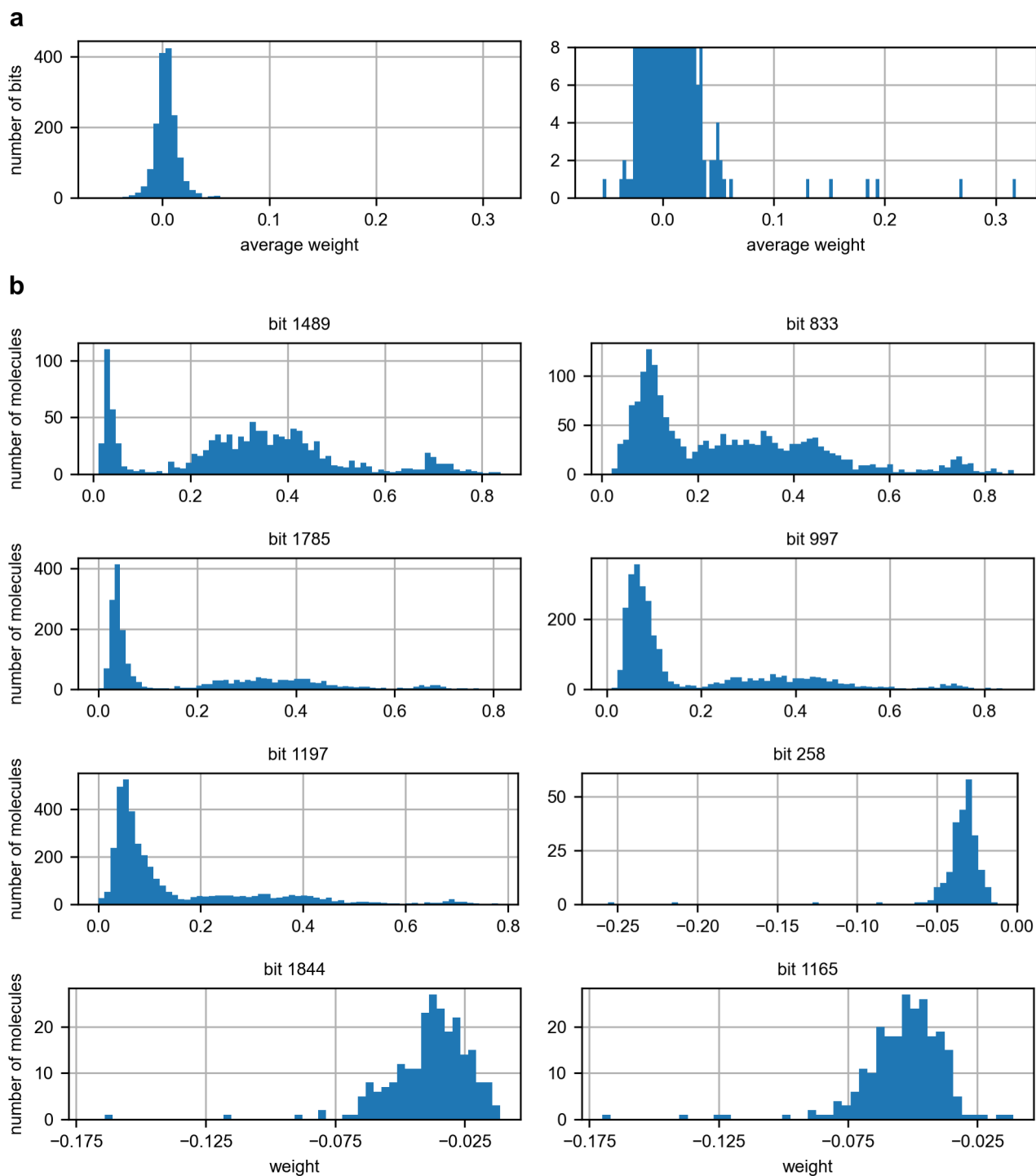


Figure S33: Histograms of **(a)** bit weights (only including bits set by at least one molecule in the dataset; plot shown in full and zoomed in) and **(b)** molecule-level bit weights for single-substructure analysis on the DD1S CAIX dataset (random split, seed 2; *cf.* Figure 2d), including the top 5 and bottom 3 bits.

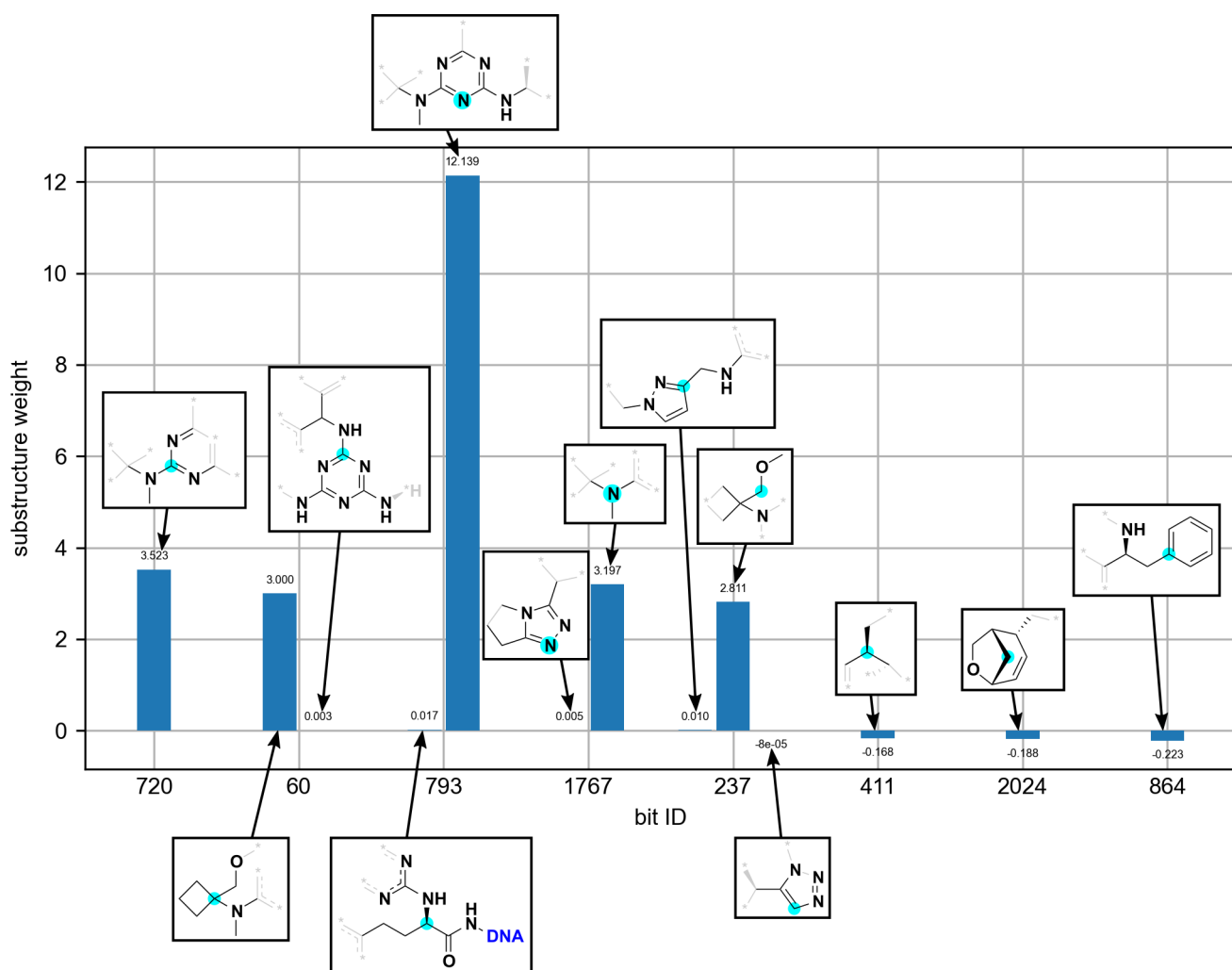
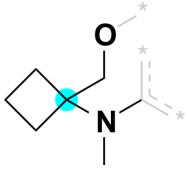
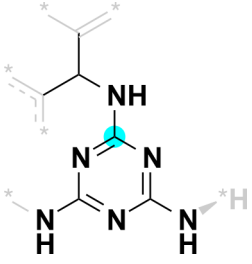
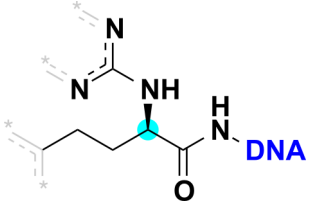
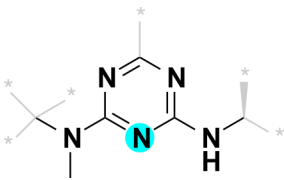
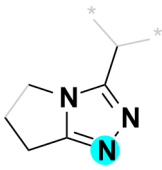
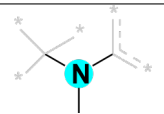
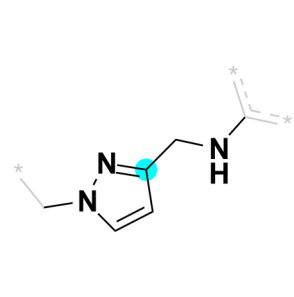
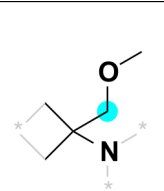
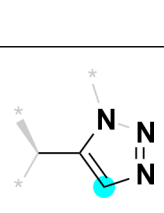
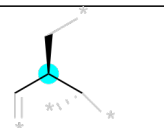

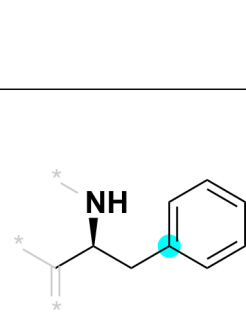


Figure S34: Single-substructure analysis on the triazine sEH dataset (random split, seed 0; *cf.* Figure 2d), including substructures mapped to the top 5 and bottom 3 bits.

Table S18: SMARTS for single-substructure analysis on the triazine sEH dataset (random split, seed 0).

bit ID	substructure example	SMARTS
720		[#6;D1;H3;R0;+0]-[#7;D3;H0;R0;+0](- [#6;D4;H0;R1;+0])-[#6;D3;H0;R1;+0](: [#7;D2;H0;R1;+0]:[#6;D3;H0;R1;+0]): [#7;D2;H0;R1;+0]:[#6;D3;H0;R1;+0]

60		[#6;D1;H3;R0;+0]-[#7;D3;H0;R0;+0](- [#6;D3;H0;R1;+0])-[#6;D4;H0;R1;+0]1(- [#6;D2;H2;R0;+0]-[#8;D2;H0;R0;+0])- [#6;D2;H2;R1;+0]-[#6;D2;H2;R1;+0]- [#6;D2;H2;R1;+0]-1
60		[#6;D3;H0;R0;+0]-[#6;D3;H1;R0;+0](- [#6;D3;H0;R1;+0])-[#7;D2;H1;R0;+0]- [#6;D3;H0;R1;+0]1:[#7;D2;H0;R1;+0]: [#6;D3;H0;R1;+0](-[#7;D2;H1;R0;+0]): [#7;D2;H0;R1;+0]:[#6;D3;H0;R1;+0](- [#7;D2;H1;R0;+0]):[#7;D2;H0;R1;+0]:1
793		[#102;D1;H0;R0;+0]-[#7;D2;H1;R0;+0]- [#6;D3;H0;R0;+0](=[#8;D1;H0;R0;+0])- [#6;D3;H1;R0;+0](-[#6;D2;H2;R0;+0]- [#6;D2;H2;R0;+0]-[#6;D3;H0;R1;+0])- [#7;D2;H1;R0;+0]-[#6;D3;H0;R1;+0](: [#7;D2;H0;R1;+0]):[#7;D2;H0;R1;+0]
793		[#6;D1;H3;R0;+0]-[#7;D3;H0;R0;+0](- [#6;D4;H0;R1;+0])-[#6;D3;H0;R1;+0]1: [#7;D2;H0;R1;+0]:[#6;D3;H0;R1;+0]: [#7;D2;H0;R1;+0]:[#6;D3;H0;R1;+0](- [#7;D2;H1;R0;+0]-[#6;D3;H1;R0;+0]): [#7;D2;H0;R1;+0]:1
1767		[#6;D2;H2;R1;+0]-[#6;D2;H2;R1;+0]- [#6;D3;H0;R2;+0]1:[#7;D2;H0;R1;+0]: [#7;D2;H0;R1;+0]:[#6;D3;H0;R1;+0](- [#6;D3;H1;R0;+0]):[#7;D3;H0;R2;+0]:1- [#6;D2;H2;R1;+0]

1767		[#6;D1;H3;R0;+0]-[#7;D3;H0;R0;+0](- [#6;D3;H0;R1;+0])-[#6;D4;H0;R1;+0]
237		[#6;D2;H2;R0;+0]-[#7;D3;H0;R1;+0]1: [#6;D2;H1;R1;+0]:[#6;D2;H1;R1;+0]: [#6;D3;H0;R1;+0](-[#6;D2;H2;R0;+0]- [#7;D2;H1;R0;+0]-[#6;D3;H0;R1;+0]): [#7;D2;H0;R1;+0]:1
237		[#6;D1;H3;R0;+0]-[#8;D2;H0;R0;+0]- [#6;D2;H2;R0;+0]-[#6;D4;H0;R1;+0](- [#6;D2;H2;R1;+0])(-[#6;D2;H2;R1;+0])- [#7;D3;H0;R0;+0]
237		[#6;D3;H1;R0;+0]-[#6;D3;H0;R1;+0](: [#7;D3;H0;R1;+0]):[#6;D2;H1;R1;+0]: [#7;D2;H0;R1;+0]:[#7;D2;H0;R1;+0]
411		[#6;D2;H1;R1;+0]-[#6;D3;H1;R1;+0](- [#6;D2;H2;R0;+0])-[#6;D3;H1;R2;+0]
2024		[#6;D2;H2;R0;+0]-[#6;D3;H1;R1;+0]1- [#6;D2;H1;R1;+0]=[#6;D2;H1;R1;+0]- [#6;D3;H1;R2;+0]2-[#6;D2;H2;R2;+0]- [#6;D3;H1;R2;+0]-1-[#6;D2;H2;R1;+0]- [#8;D2;H0;R1;+0]-2
864		[#6;D3;H0;R0;+0]-[#6;D3;H1;R0;+0](- [#7;D2;H1;R0;+0])-[#6;D2;H2;R0;+0]- [#6;D3;H0;R1;+0]1:[#6;D2;H1;R1;+0]: [#6;D2;H1;R1;+0]:[#6;D2;H1;R1;+0]: [#6;D2;H1;R1;+0]:[#6;D2;H1;R1;+0]:1

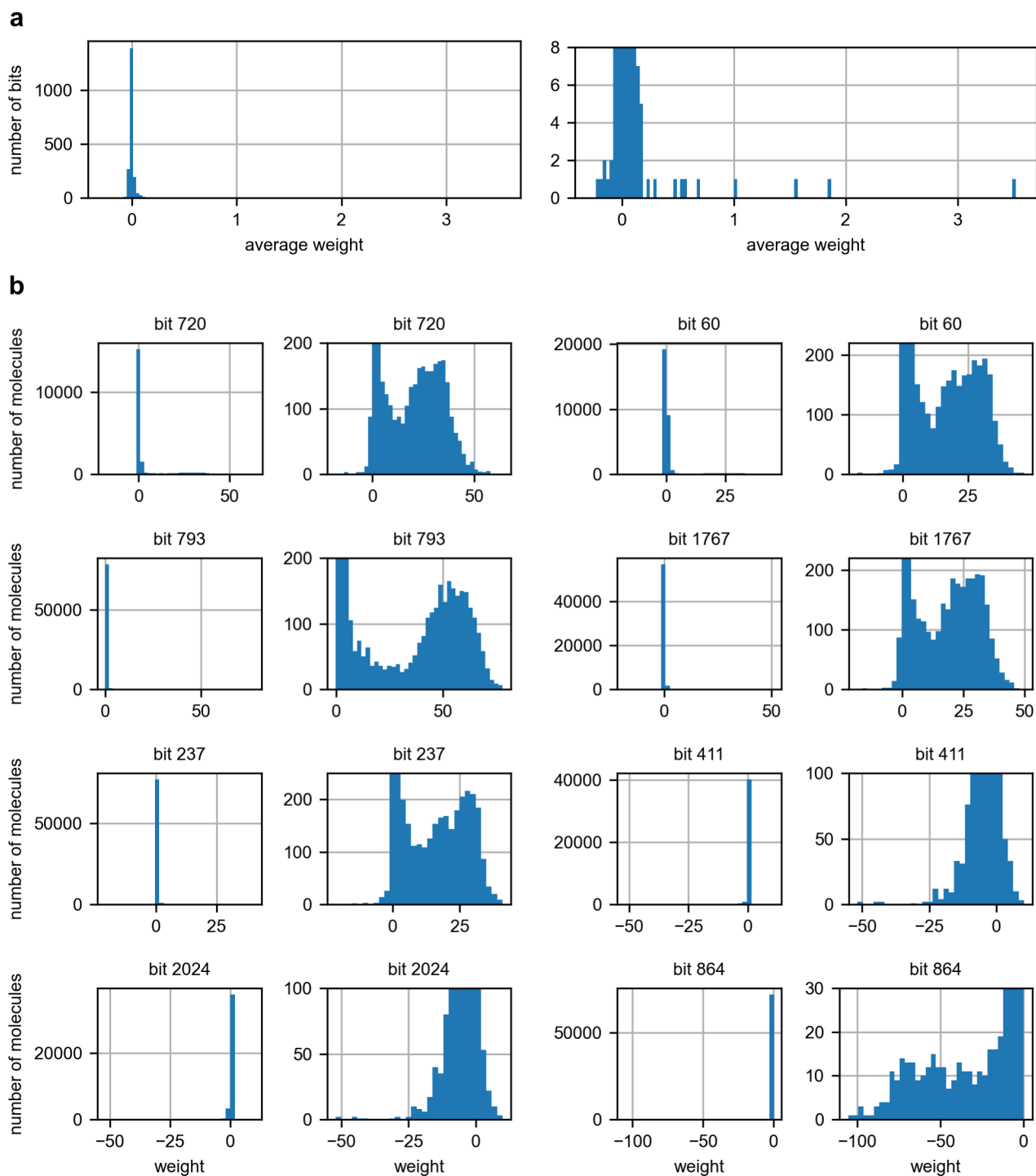


Figure S35: Histograms of **(a)** bit weights (only including bits set by at least one molecule in the dataset) and **(b)** molecule-level bit weights for single-substructure analysis on the triazine sEH dataset (random split, seed 0; cf. Figure 2d), including the top 5 and bottom 3 bits. Plots are shown in full and zoomed in.

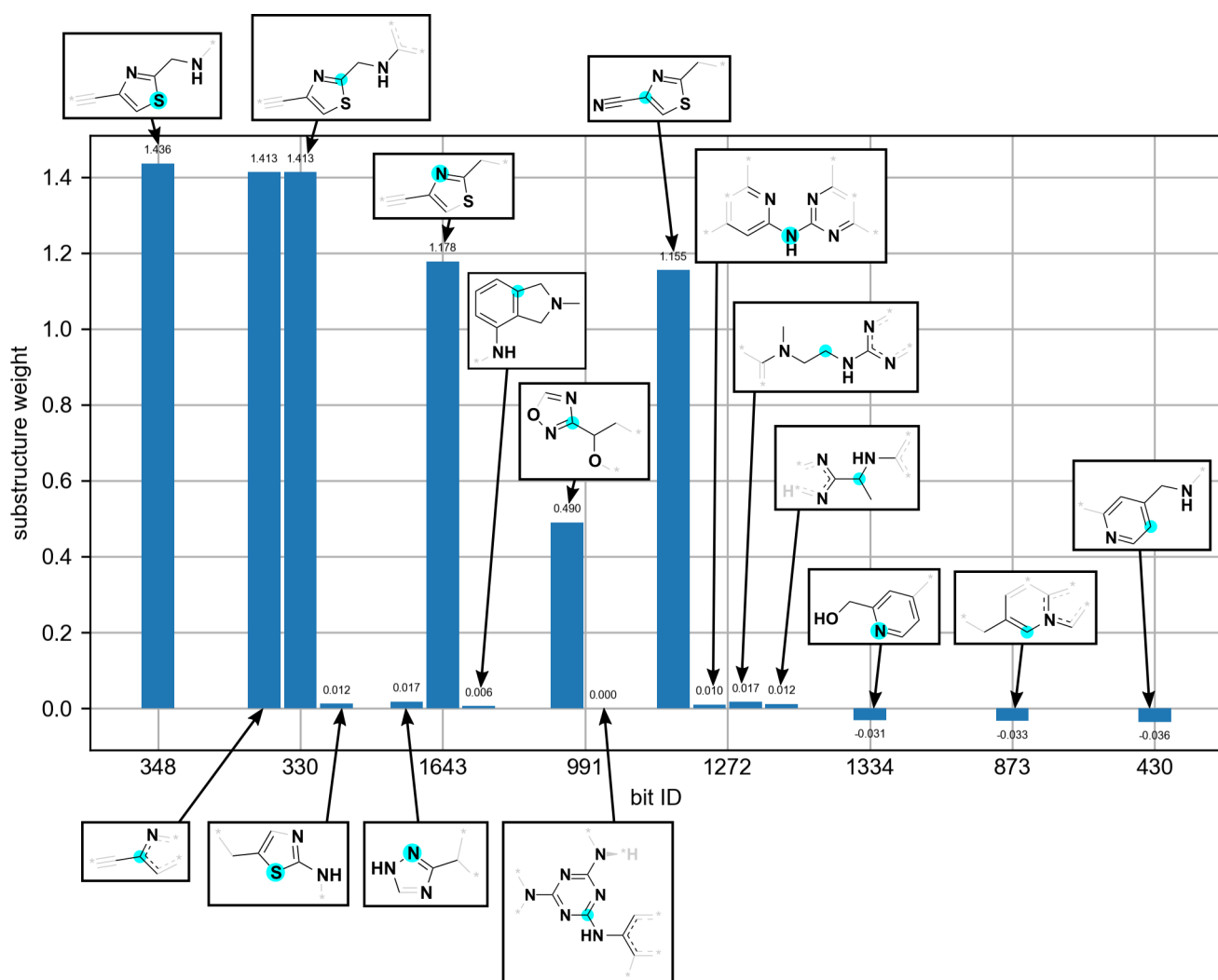
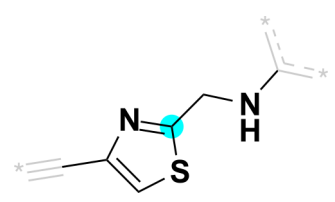
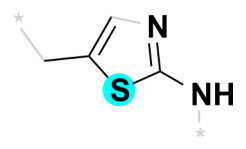
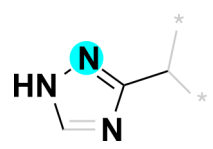
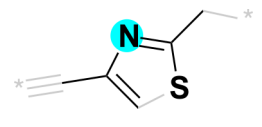
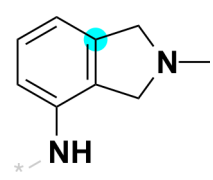

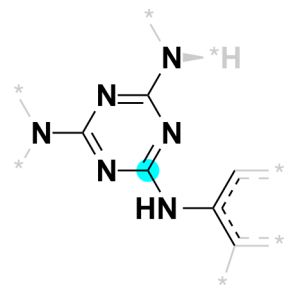
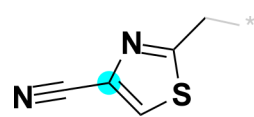
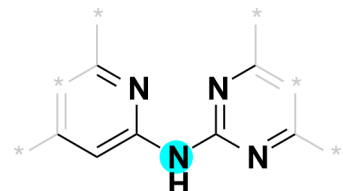
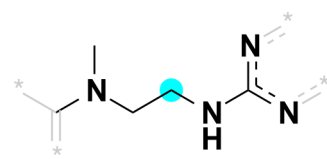
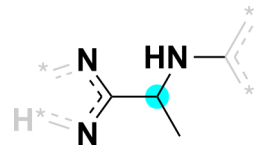


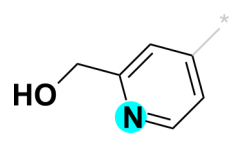
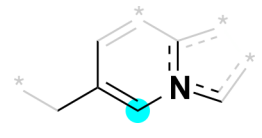
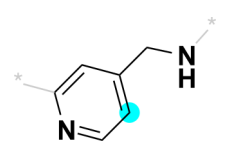
Figure S36: Single-substructure analysis on the triazine SIRT2 dataset (random split, seed 0; *cf.* Figure 2d), including substructures mapped to the top 5 and bottom 3 bits.

Table S19: SMARTS for single-substructure analysis on the triazine SIRT2 dataset (random split, seed 0).

bit ID	substructure example	SMARTS
348		[#6;D2;H0;R0;+0]-[#6;D3;H0;R1;+0]1: [#6;D2;H1;R1;+0]:[#16;D2;H0;R1;+0]: [#6;D3;H0;R1;+0](-[#6;D2;H2;R0;+0]- [#7;D2;H1;R0;+0]):[#7;D2;H0;R1;+0]:1
330		[#6;D2;H0;R0;+0]-[#6;D3;H0;R1;+0](: [#6;D2;H1;R1;+0]):[#7;D2;H0;R1;+0]

330		$[#6;D2;H0;R0;+0]-[#6;D3;H0;R1;+0]1:$ $[#6;D2;H1;R1;+0]:[#16;D2;H0;R1;+0]:$ $[#6;D3;H0;R1;+0](-[#6;D2;H2;R0;+0]-$ $[#7;D2;H1;R0;+0]-[#6;D3;H0;R1;+0]):$ $[#7;D2;H0;R1;+0]:1$
330		$[#6;D2;H1;R1;+0]:[#6;D3;H0;R1;+0](-$ $[#6;D2;H2;R0;+0]):[#16;D2;H0;R1;+0]:$ $[#6;D3;H0;R1;+0]([#7;D2;H0;R1;+0])-$ $[#7;D2;H1;R0;+0]$
1643		$[#6;D2;H1;R1;+0]:[#7;D2;H1;R1;+0]:$ $[#7;D2;H0;R1;+0]:[#6;D3;H0;R1;+0](-$ $[#6;D3;H1;R0;+0]):[#7;D2;H0;R1;+0]$
1643		$[#16;D2;H0;R1;+0]:[#6;D3;H0;R1;+0](-$ $[#6;D2;H2;R0;+0]):[#7;D2;H0;R1;+0]:$ $[#6;D3;H0;R1;+0](-[#6;D2;H0;R0;+0]):$ $[#6;D2;H1;R1;+0]$
1643		$[#6;D1;H3;R0;+0]-[#7;D3;H0;R1;+0]1-$ $[#6;D2;H2;R1;+0]-[#6;D3;H0;R2;+0]2:$ $[#6;D2;H1;R1;+0]:[#6;D2;H1;R1;+0]:$ $[#6;D2;H1;R1;+0]:[#6;D3;H0;R1;+0](-$ $[#7;D2;H1;R0;+0]):[#6;D3;H0;R2;+0]:2-$ $[#6;D2;H2;R1;+0]-1$
991		$[#6;D2;H1;R1;+0]:[#7;D2;H0;R1;+0]:$ $[#6;D3;H0;R1;+0]([#7;D2;H0;R1;+0]:$ $[#8;D2;H0;R1;+0])-[#6;D3;H1;R1;+0](-$ $[#6;D2;H2;R1;+0])-[#8;D2;H0;R1;+0]$

991		[#6;D2;H1;R1;+0]:[#6;D3;H0;R1;+0]([#6;D3;H0;R2;+0])-[#7;D2;H1;R0;+0]- [#6;D3;H0;R1;+0]1:[#7;D2;H0;R1;+0]: [#6;D3;H0;R1;+0](-[#7;D3;H0;R0;+0]): [#7;D2;H0;R1;+0]:[#6;D3;H0;R1;+0](- [#7;D3;H0;R0;+0]):[#7;D2;H0;R1;+0]:1
1272		[#6;D2;H2;R0;+0]-[#6;D3;H0;R1;+0]1: [#16;D2;H0;R1;+0]:[#6;D2;H1;R1;+0]: [#6;D3;H0;R1;+0](-[#6;D2;H0;R0;+0])# [#7;D1;H0;R0;+0]):[#7;D2;H0;R1;+0]:1
1272		[#6;D3;H0;R1;+0]:[#6;D2;H1;R1;+0]: [#6;D3;H0;R1;+0]([#7;D2;H0;R1;+0]: [#6;D3;H0;R1;+0])-[#7;D2;H1;R0;+0]- [#6;D3;H0;R1;+0]([#7;D2;H0;R1;+0]: [#6;D3;H0;R1;+0]):[#7;D2;H0;R1;+0]: [#6;D3;H0;R1;+0]
1272		[#6;D1;H3;R0;+0]-[#7;D3;H0;R0;+0](- [#6;D3;H0;R0;+0])-[#6;D2;H2;R0;+0]- [#6;D2;H2;R0;+0]-[#7;D2;H1;R0;+0]- [#6;D3;H0;R1;+0]([#7;D2;H0;R1;+0]): [#7;D2;H0;R1;+0]
1272		[#6;D1;H3;R0;+0]-[#6;D3;H1;R0;+0](- [#7;D2;H1;R0;+0]-[#6;D3;H0;R1;+0])- [#6;D3;H0;R1;+0]([#7;D2;H0;R1;+0]): [#7;D2;H0;R1;+0]

1334		$[\#8;D1;H1;R0;+0]-[\#6;D2;H2;R0;+0]-$ $[\#6;D3;H0;R1;+0]1:[\#6;D2;H1;R1;+0]:$ $[\#6;D3;H0;R1;+0]:[\#6;D2;H1;R1;+0]:$ $[\#6;D2;H1;R1;+0]:[\#7;D2;H0;R1;+0]:1$
873		$[\#6;D2;H1;R1;+0]:[\#6;D3;H0;R1;+0](-$ $[\#6;D2;H2;R0;+0]):[\#6;D2;H1;R1;+0]:$ $[\#7;D3;H0;R2;+0](:[\#6;D2;H1;R1;+0]):$ $[\#6;D3;H0;R2;+0]$
430		$[\#7;D2;H1;R0;+0]-[\#6;D2;H2;R0;+0]-$ $[\#6;D3;H0;R1;+0]1:[\#6;D2;H1;R1;+0]:$ $[\#6;D2;H1;R1;+0]:[\#7;D2;H0;R1;+0]:$ $[\#6;D3;H0;R1;+0]:[\#6;D2;H1;R1;+0]:1$

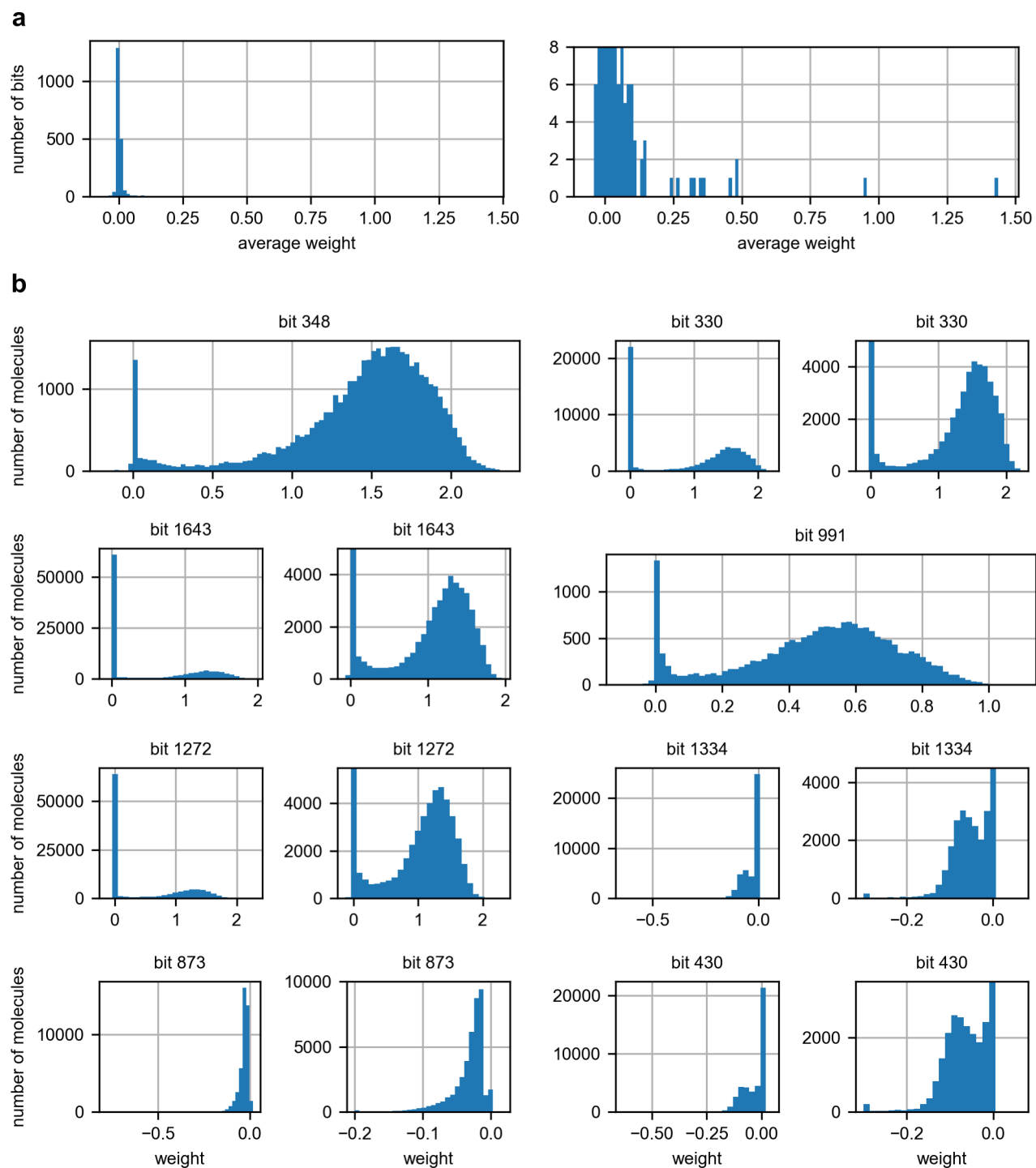


Figure S37: Histograms of **(a)** bit weights (only including bits set by at least one molecule in the dataset) and **(b)** molecule-level bit weights for single-substructure analysis on the triazine SIRT2 dataset (random split, seed 0; *cf.* Figure 2d), including the top 5 and bottom 3 bits. Plots are shown in full and zoomed in.

S2.9.2 Substructure-pair analysis

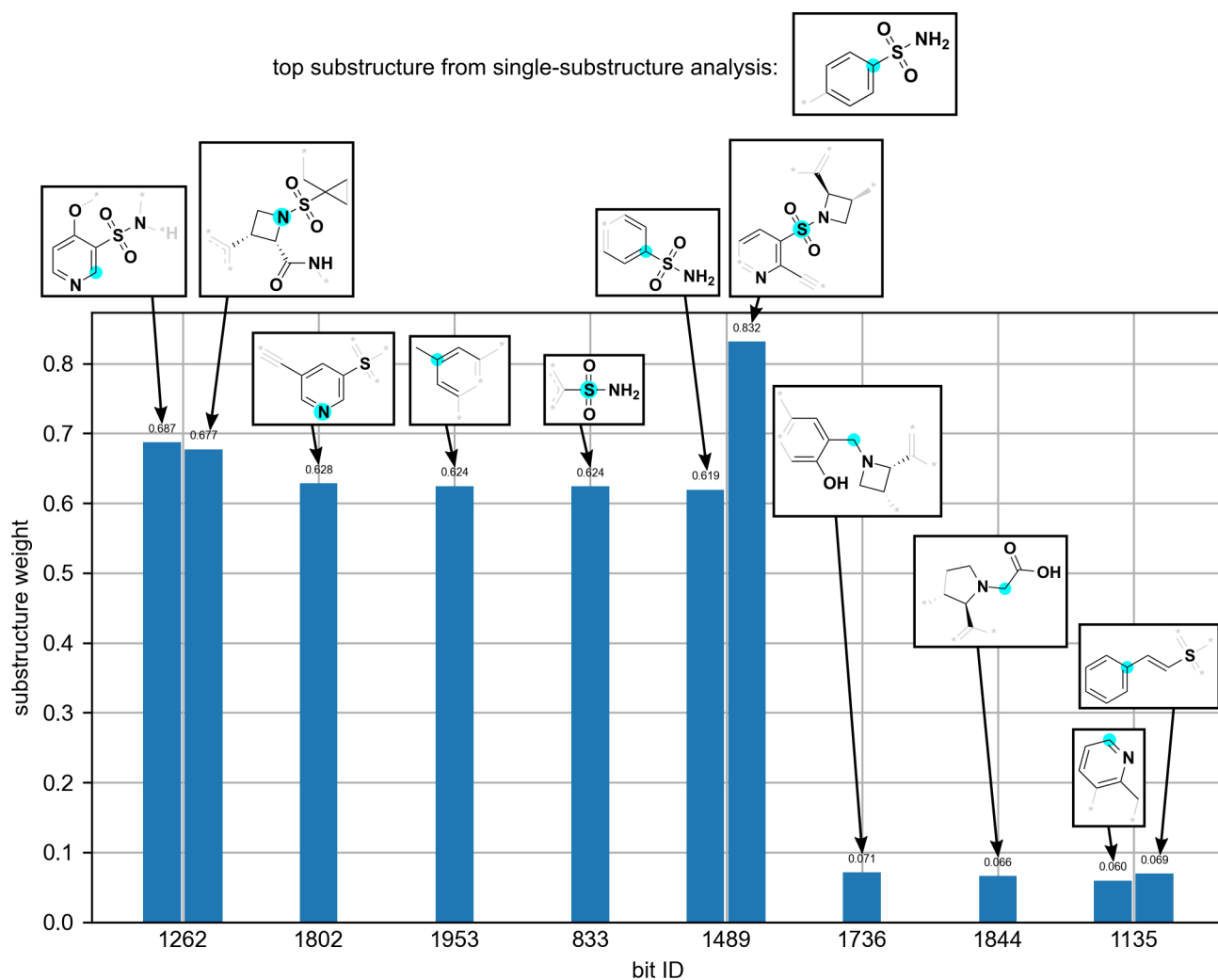
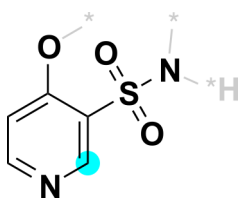
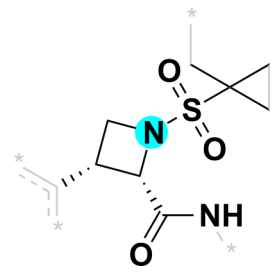
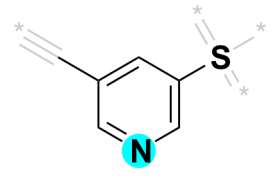
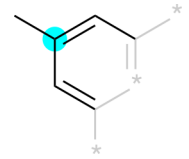
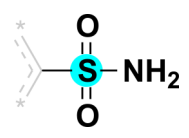
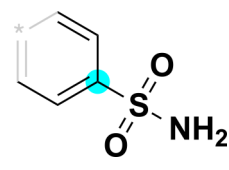
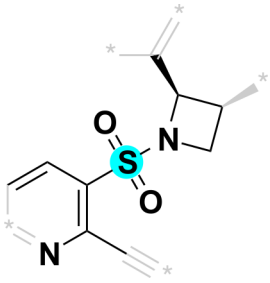
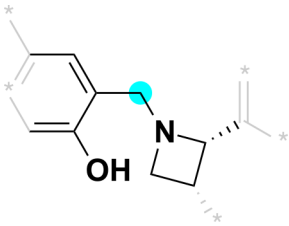
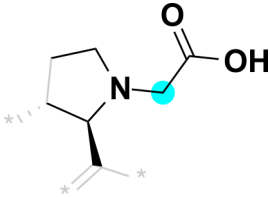
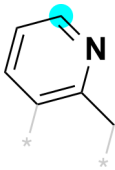
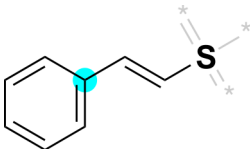


Figure S38: Substructure-pair analysis on the DD1S CAIX dataset (random split, seed 0; *cf.* Figure 2d), based on the top substructure from the single-substructure analysis.

Table S20: SMARTS for substructure-pair analysis on the DD1S CAIX dataset (random split, seed 0).

bit ID	substructure example	SMARTS
1262		<chem>[*]7D3H0R1+0[*]-[*]16D4H0R0+0[*](=[*]8D1H0R0+0[*])(=[*]8D1H0R0+0[*])-[*]6D3H0R1+0[*]1:[*]6D2H1R1+0[*]:[*]7D2H0R1+0[*]:[*]6D2H1R1+0[*]:[*]6D2H1R1+0[*]:[*]6D3H0R1+0[*]:1-[*]8D2H0R0+0[*]</chem>

1262		$[\#6;D2;H2;R0;+0]-[\#6;D4;H0;R1;+0](-[\#6;D2;H2;R1;+0])(-[\#16;D4;H0;R0;+0])(=[\#8;D1;H0;R0;+0])(=[\#8;D1;H0;R0;+0])-[\#7;D3;H0;R1;+0]1-[\#6;D2;H2;R1;+0]-[\#6;D3;H1;R1;+0](-[\#6;D3;H0;R1;+0])-[\#6;D3;H1;R1;+0]1-[\#6;D3;H0;R0;+0](-[\#7;D2;H1;R0;+0])=[\#8;D1;H0;R0;+0]$
1802		$[\#16;D4;H0;R0;+0]-[\#6;D3;H0;R1;+0]1: [\#6;D2;H1;R1;+0]:[\#7;D2;H0;R1;+0]: [\#6;D2;H1;R1;+0]:[\#6;D3;H0;R1;+0](-[\#6;D2;H0;R0;+0]):[\#6;D2;H1;R1;+0]:1$
1953		$[\#6;D1;H3;R0;+0]-[\#6;D3;H0;R1;+0](:[\#6;D2;H1;R1;+0]:[\#6;D3;H0;R1;+0]): [\#6;D2;H1;R1;+0]:[\#6;D3;H0;R1;+0]$
833		$[\#6;D3;H0;R1;+0]-[\#16;D4;H0;R0;+0](-[\#7;D1;H2;R0;+0])(=[\#8;D1;H0;R0;+0])=[\#8;D1;H0;R0;+0]$
1489		$[\#6;D2;H1;R1;+0]:[\#6;D2;H1;R1;+0]: [\#6;D3;H0;R1;+0](:[\#6;D2;H1;R1;+0]: [\#6;D2;H1;R1;+0])-[\#16;D4;H0;R0;+0](-[\#7;D1;H2;R0;+0])(=[\#8;D1;H0;R0;+0])=[\#8;D1;H0;R0;+0]$

1489		$[\#6;D2;H0;R0;+0]-[\#6;D3;H0;R1;+0](\colon$ $[\#7;D2;H0;R1;+0]):[\#6;D3;H0;R1;+0](\colon$ $[\#6;D2;H1;R1;+0]:[\#6;D2;H1;R1;+0])-$ $[\#16;D4;H0;R0;+0](=[\#8;D1;H0;R0;+0])(=$ $[\#8;D1;H0;R0;+0])-[\#7;D3;H0;R1;+0]1-$ $[\#6;D2;H2;R1;+0]-[\#6;D3;H1;R1;+0]-$ $[\#6;D3;H1;R1;+0]1-[\#6;D3;H0;R0;+0]$
1736		$[\#6;D2;H1;R1;+0]:[\#6;D3;H0;R1;+0](-$ $[\#8;D1;H1;R0;+0]):[\#6;D3;H0;R1;+0](\colon$ $[\#6;D2;H1;R1;+0]:[\#6;D3;H0;R1;+0])-$ $[\#6;D2;H2;R0;+0]-[\#7;D3;H0;R1;+0]1-$ $[\#6;D2;H2;R1;+0]-[\#6;D3;H1;R1;+0]-$ $[\#6;D3;H1;R1;+0]1-[\#6;D3;H0;R0;+0]$
1844		$[\#6;D2;H2;R1;+0]-[\#6;D2;H2;R1;+0]-$ $[\#7;D3;H0;R1;+0](=[\#6;D2;H2;R0;+0]-$ $[\#6;D3;H0;R0;+0])(=[\#8;D1;H0;R0;+0])-$ $[\#8;D1;H1;R0;+0])-[\#6;D3;H1;R1;+0](-$ $[\#6;D3;H0;R0;+0])-[\#6;D3;H1;R1;+0]$
1135		$[\#6;D2;H2;R0;+0]-[\#6;D3;H0;R1;+0]1:$ $[\#6;D3;H0;R1;+0]:[\#6;D2;H1;R1;+0]:$ $[\#6;D2;H1;R1;+0]:[\#6;D2;H1;R1;+0]:$ $[\#7;D2;H0;R1;+0]:1$
1135		$[\#16;D4;H0;R0;+0]-[\#6;D2;H1;R0;+0]=$ $[\#6;D2;H1;R0;+0]-[\#6;D3;H0;R1;+0]1:$ $[\#6;D2;H1;R1;+0]:[\#6;D2;H1;R1;+0]:$ $[\#6;D2;H1;R1;+0]:[\#6;D2;H1;R1;+0]:$ $[\#6;D2;H1;R1;+0]:1$

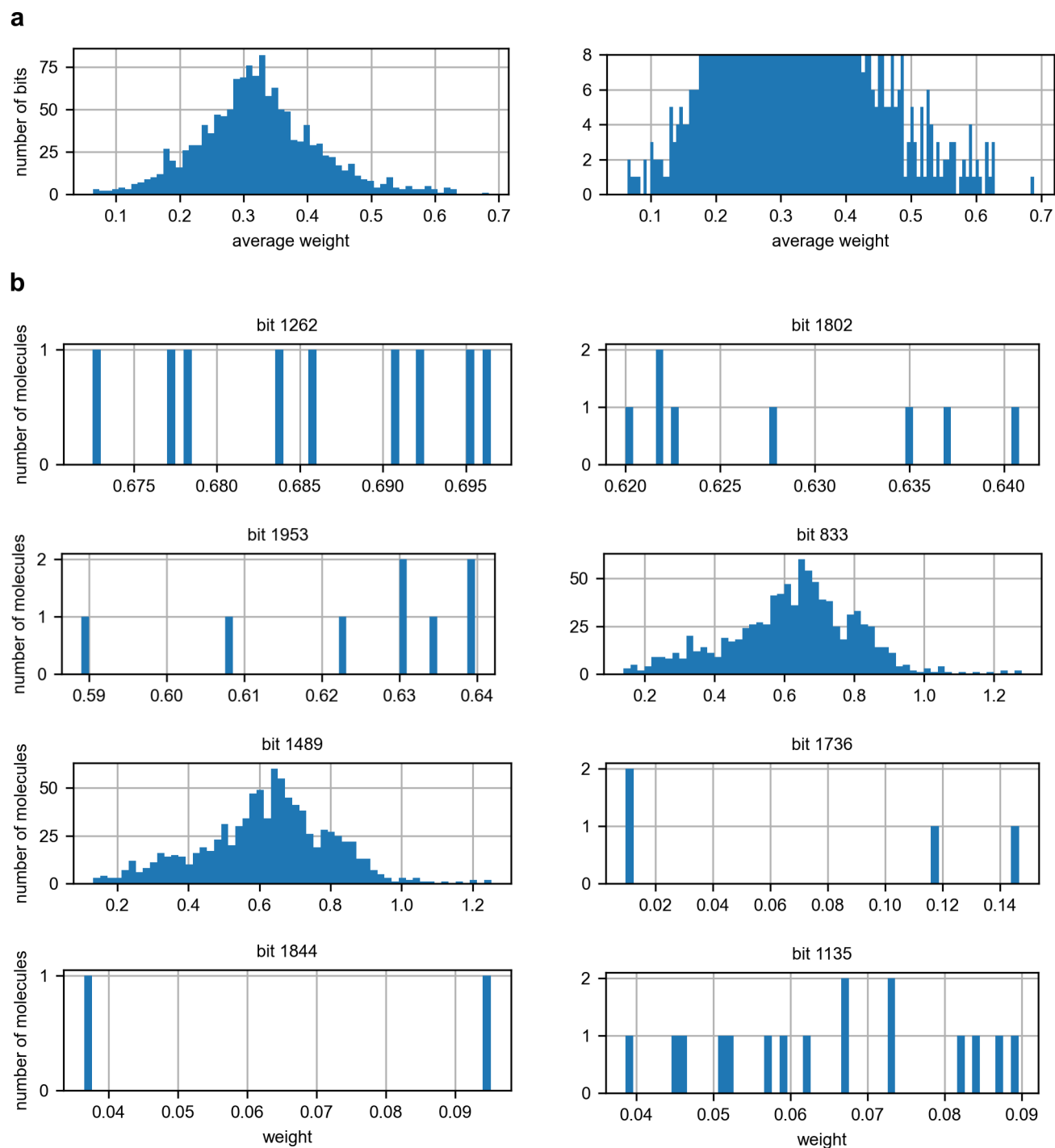


Figure S39: Histograms of **(a)** bit weights (only including bits set by at least one molecule in the dataset; plot shown in full and zoomed in) and **(b)** molecule-level bit weights for substructure-pair analysis on the DD1S CAIX dataset (random split, seed 0; *cf.* Figure 2d), including the top 5 and bottom 3 bits.

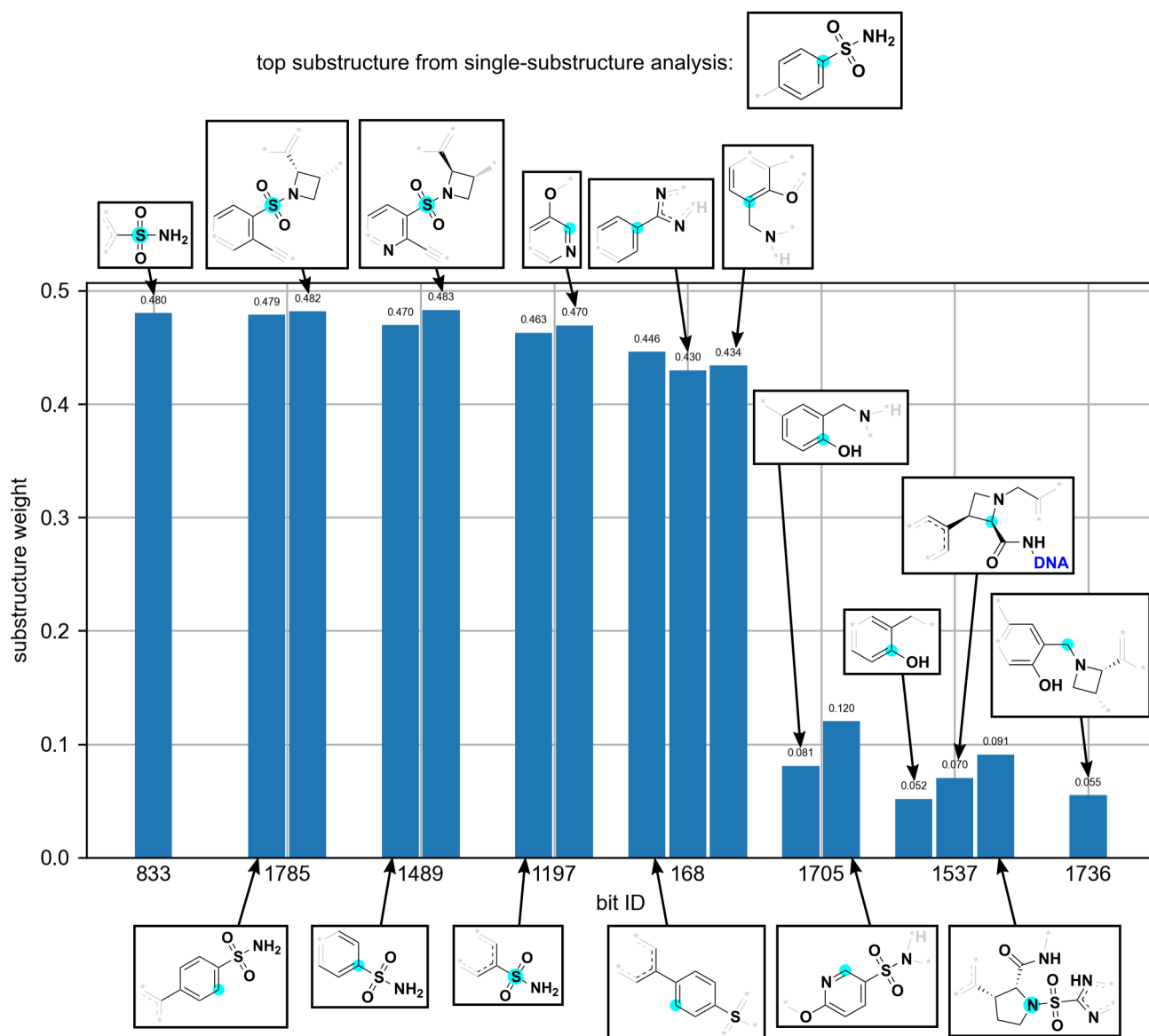
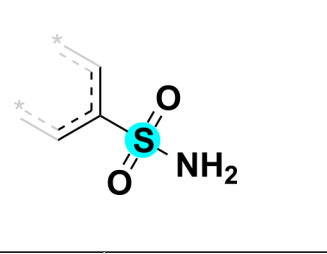
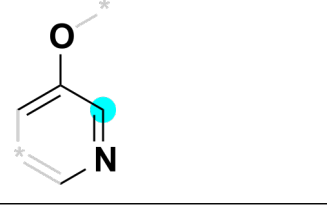
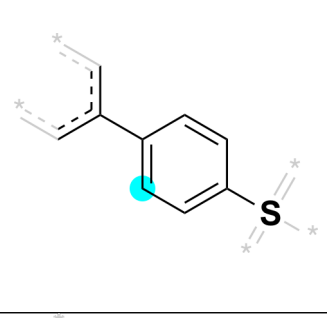
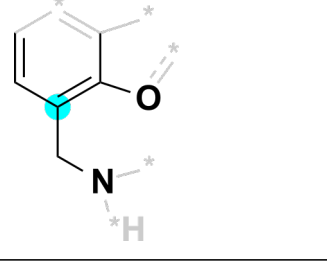
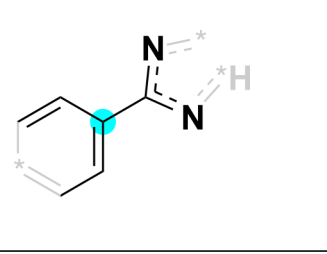
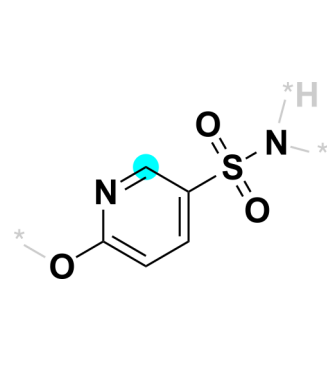


Figure S40: Substructure-pair analysis on the DD1S CAIX dataset (random split, seed 1; *cf.* Figure 2d), based on the top substructure from the single-substructure analysis.

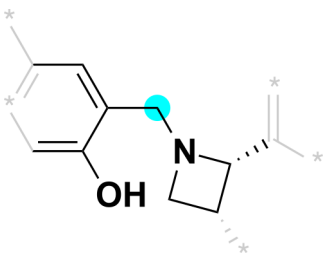
Table S21: SMARTS for substructure-pair analysis on the DD1S CAIX dataset (random split, seed 1).

bit ID	substructure example	SMARTS
833		<chem>[*]([*])S(=O)(=O)N</chem>

1785		$[\#6;D3;H0;R1;+0]-[\#6;D3;H0;R1;+0]1:$ $[\#6;D2;H1;R1;+0]:[\#6;D2;H1;R1;+0]:$ $[\#6;D3;H0;R1;+0](-[\#16;D4;H0;R0;+0](-$ $[\#7;D1;H2;R0;+0])(=[\#8;D1;H0;R0;+0])=$ $[\#8;D1;H0;R0;+0]):[\#6;D2;H1;R1;+0]:$ $[\#6;D2;H1;R1;+0]:1$
1785		$[\#6;D2;H0;R0;+0]-[\#6;D3;H0;R1;+0](:$ $[\#6;D2;H1;R1;+0]):[\#6;D3;H0;R1;+0](:$ $[\#6;D2;H1;R1;+0]:[\#6;D2;H1;R1;+0])-$ $[\#16;D4;H0;R0;+0])(=[\#8;D1;H0;R0;+0])(=$ $[\#8;D1;H0;R0;+0])-[\#7;D3;H0;R1;+0]1-$ $[\#6;D2;H2;R1;+0]-[\#6;D3;H1;R1;+0]-$ $[\#6;D3;H1;R1;+0]-1-[\#6;D3;H0;R0;+0]$
1489		$[\#6;D2;H1;R1;+0]:[\#6;D2;H1;R1;+0]:$ $[\#6;D3;H0;R1;+0](:[\#6;D2;H1;R1;+0]:$ $[\#6;D2;H1;R1;+0])-[\#16;D4;H0;R0;+0](-$ $[\#7;D1;H2;R0;+0])(=[\#8;D1;H0;R0;+0])=$ $[\#8;D1;H0;R0;+0]$
1489		$[\#6;D2;H0;R0;+0]-[\#6;D3;H0;R1;+0](:$ $[\#7;D2;H0;R1;+0]):[\#6;D3;H0;R1;+0](:$ $[\#6;D2;H1;R1;+0]:[\#6;D2;H1;R1;+0])-$ $[\#16;D4;H0;R0;+0])(=[\#8;D1;H0;R0;+0])(=$ $[\#8;D1;H0;R0;+0])-[\#7;D3;H0;R1;+0]1-$ $[\#6;D2;H2;R1;+0]-[\#6;D3;H1;R1;+0]-$ $[\#6;D3;H1;R1;+0]-1-[\#6;D3;H0;R0;+0]$

1197		$[\#6;D2;H1;R1;+0]:[\#6;D3;H0;R1;+0](\colon$ $[\#6;D2;H1;R1;+0)]-[\#16;D4;H0;R0;+0](\colon$ $[\#7;D1;H2;R0;+0])(=[\#8;D1;H0;R0;+0])=$ $[\#8;D1;H0;R0;+0]$
1197		$[\#6;D2;H1;R1;+0]:[\#7;D2;H0;R1;+0]:$ $[\#6;D2;H1;R1;+0]:[\#6;D3;H0;R1;+0](\colon$ $[\#6;D2;H1;R1;+0)]-[\#8;D2;H0;R0;+0]$
168		$[\#16;D4;H0;R0;+0]-[\#6;D3;H0;R1;+0]1:$ $[\#6;D2;H1;R1;+0]:[\#6;D2;H1;R1;+0]:$ $[\#6;D3;H0;R1;+0](\colon[\#6;D3;H0;R1;+0](\colon$ $[\#6;D2;H1;R1;+0]):[\#6;D2;H1;R1;+0]):$ $[\#6;D2;H1;R1;+0]:[\#6;D2;H1;R1;+0]:1$
168		$[\#6;D2;H1;R1;+0]:[\#6;D2;H1;R1;+0]:$ $[\#6;D3;H0;R1;+0](\colon[\#6;D2;H2;R0;+0]-$ $[\#7;D3;H0;R1;+0]):[\#6;D3;H0;R2;+0](\colon$ $[\#6;D3;H0;R2;+0]):[\#8;D2;H0;R1;+0]$
168		$[\#6;D2;H1;R1;+0]:[\#6;D2;H1;R1;+0]:$ $[\#6;D3;H0;R1;+0](\colon[\#6;D2;H1;R1;+0]:$ $[\#6;D2;H1;R1;+0)]-[\#6;D3;H0;R1;+0](\colon$ $[\#7;D2;H0;R1;+0]):[\#7;D2;H0;R1;+0]$
1705		$[\#7;D3;H0;R1;+0]-[\#16;D4;H0;R0;+0](=$ $[\#8;D1;H0;R0;+0])(=[\#8;D1;H0;R0;+0])-$ $[\#6;D3;H0;R1;+0]1: [\#6;D2;H1;R1;+0]:$ $[\#6;D2;H1;R1;+0]:[\#6;D3;H0;R1;+0](\colon$ $[\#8;D2;H0;R0;+0]):[\#7;D2;H0;R1;+0]:$ $[\#6;D2;H1;R1;+0]:1$

1705		$[\#7;D3;H0;R1;+0]-[\#6;D2;H2;R0;+0]-$ $[\#6;D3;H0;R1;+0]1:[\#6;D2;H1;R1;+0]:$ $[\#6;D3;H0;R1;+0]:[\#6;D2;H1;R1;+0]:$ $[\#6;D2;H1;R1;+0]:[\#6;D3;H0;R1;+0]:1-$ $[\#8;D1;H1;R0;+0]$
1537		$[\#6;D2;H1;R1;+0]:[\#6;D2;H1;R1;+0]:$ $[\#6;D3;H0;R1;+0](-[\#8;D1;H1;R0;+0]):$ $[\#6;D3;H0;R1;+0](:[\#6;D2;H1;R1;+0])-$ $[\#6;D2;H2;R0;+0]$
1537		$[\#6;D3;H0;R1;+0]-[\#6;D3;H1;R1;+0]1-$ $[\#6;D2;H2;R1;+0]-[\#6;D2;H2;R1;+0]-$ $[\#7;D3;H0;R1;+0](-[\#16;D4;H0;R0;+0])(=$ $[\#8;D1;H0;R0;+0])(=[\#8;D1;H0;R0;+0])-$ $[\#6;D3;H0;R1;+0](:[\#7;D2;H0;R1;+0]):$ $[\#7;D2;H1;R1;+0])-[\#6;D3;H1;R1;+0]1-$ $[\#6;D3;H0;R0;+0](-[\#7;D2;H1;R0;+0])=$ $[\#8;D1;H0;R0;+0]$
1537		$[\#102;D1;H0;R0;+0]-[\#7;D2;H1;R0;+0]-$ $[\#6;D3;H0;R0;+0](=[\#8;D1;H0;R0;+0])-$ $[\#6;D3;H1;R1;+0]1-[\#6;D3;H1;R1;+0](-$ $[\#6;D3;H0;R1;+0](:[\#6;D2;H1;R1;+0]):$ $[\#6;D2;H1;R1;+0])-[\#6;D2;H2;R1;+0]-$ $[\#7;D3;H0;R1;+0]1-[\#6;D2;H2;R0;+0]-$ $[\#6;D3;H0;R0;+0]$

1736		$[\#6;D2;H1;R1;+0]:[\#6;D3;H0;R1;+0](-$ $[\#8;D1;H1;R0;+0]):[\#6;D3;H0;R1;+0](:$ $[\#6;D2;H1;R1;+0]:[\#6;D3;H0;R1;+0])-$ $[\#6;D2;H2;R0;+0]-[\#7;D3;H0;R1;+0]1-$ $[\#6;D2;H2;R1;+0]-[\#6;D3;H1;R1;+0]-$ $[\#6;D3;H1;R1;+0]-1-[\#6;D3;H0;R0;+0]$
------	---	---

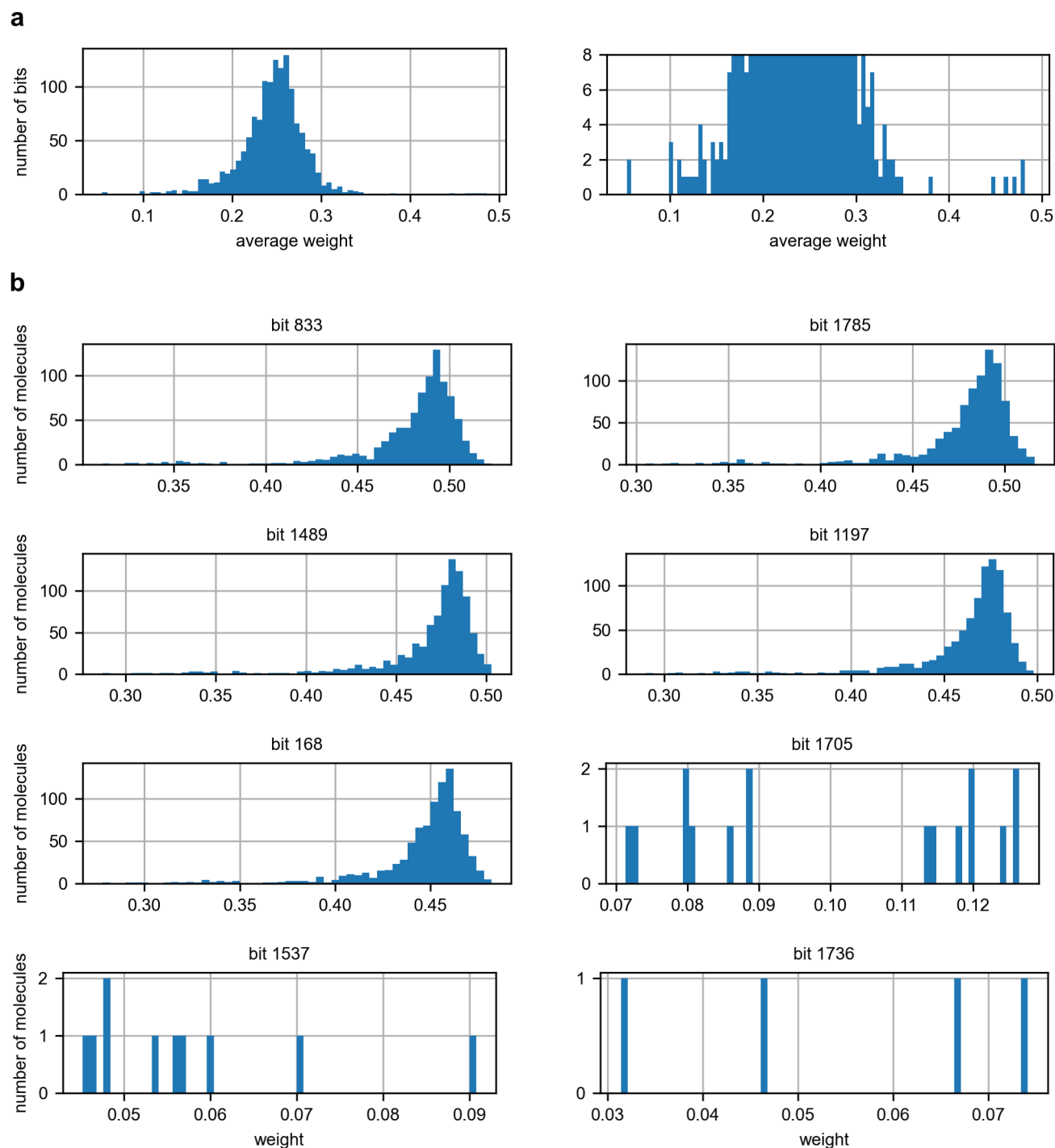


Figure S41: Histograms of **(a)** bit weights (only including bits set by at least one molecule in the dataset; plot shown in full and zoomed in) and **(b)** molecule-level bit weights for substructure-pair analysis on the DD1S CAIX dataset (random split, seed 1; *cf.* Figure 2d), including the top 5 and bottom 3 bits.

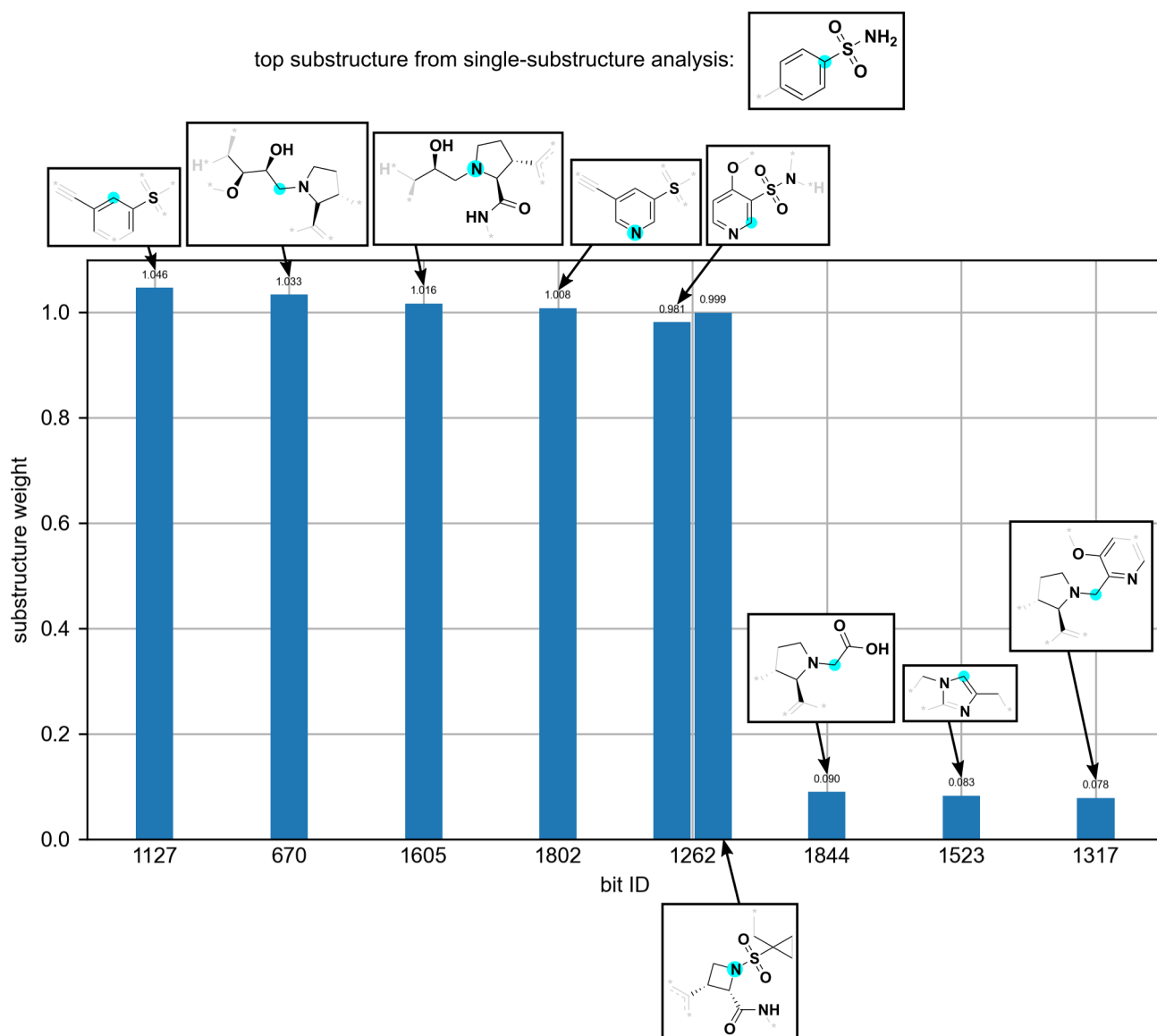
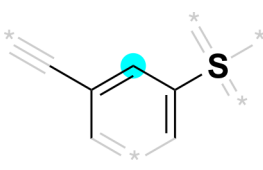


Figure S42: Substructure-pair analysis on the DD1S CAIX dataset (random split, seed 2; *cf.* Figure 2d), based on the top substructure from the single-substructure analysis.

Table S22: SMARTS for substructure-pair analysis on the DD1S CAIX dataset (random split, seed 2).

bit ID	substructure example	SMARTS
1127		<chem>[*]1C=CC(=C(C#C)S(=O)(=O)N)C=C1[*]</chem>

670		$[\#6;D2;H2;R1;+0]-[\#6;D2;H2;R1;+0]-$ $[\#7;D3;H0;R1;+0](-[\#6;D2;H2;R0;+0]-$ $[\#6;D3;H1;R0;+0](-[\#8;D1;H1;R0;+0])-$ $[\#6;D3;H1;R1;+0](-[\#6;D3;H1;R1;+0])-$ $[\#8;D2;H0;R1;+0]-[\#6;D3;H1;R1;+0](-$ $[\#6;D3;H0;R0;+0]-[\#6;D3;H1;R1;+0]$
1605		$[\#6;D3;H0;R1;+0]-[\#6;D3;H1;R1;+0]1-$ $[\#6;D2;H2;R1;+0]-[\#6;D2;H2;R1;+0]-$ $[\#7;D3;H0;R1;+0](-[\#6;D2;H2;R0;+0]-$ $[\#6;D3;H1;R0;+0](-[\#6;D3;H1;R1;+0])-$ $[\#8;D1;H1;R0;+0]-[\#6;D3;H1;R1;+0]1-$ $[\#6;D3;H0;R0;+0](-[\#7;D2;H1;R0;+0])=$ $[\#8;D1;H0;R0;+0]$
1802		$[\#16;D4;H0;R0;+0]-[\#6;D3;H0;R1;+0]1:$ $[\#6;D2;H1;R1;+0]:[\#7;D2;H0;R1;+0]:$ $[\#6;D2;H1;R1;+0]:[\#6;D3;H0;R1;+0](-$ $[\#6;D2;H0;R0;+0]):[\#6;D2;H1;R1;+0]:1$
1262		$[\#7;D3;H0;R1;+0]-[\#16;D4;H0;R0;+0](=$ $[\#8;D1;H0;R0;+0])(=[\#8;D1;H0;R0;+0])-$ $[\#6;D3;H0;R1;+0]1: [\#6;D2;H1;R1;+0]:$ $[\#7;D2;H0;R1;+0]: [\#6;D2;H1;R1;+0]:$ $[\#6;D2;H1;R1;+0]: [\#6;D3;H0;R1;+0]:1-$ $[\#8;D2;H0;R0;+0]$

1262		$ \begin{aligned} &[\#6;\text{D}2;\text{H}2;\text{R}0;+0]-[\#6;\text{D}4;\text{H}0;\text{R}1;+0](- \\ &[\#6;\text{D}2;\text{H}2;\text{R}1;+0])(-[\#6;\text{D}2;\text{H}2;\text{R}1;+0])- \\ &[\#16;\text{D}4;\text{H}0;\text{R}0;+0](=[\#8;\text{D}1;\text{H}0;\text{R}0;+0])(= \\ &[\#8;\text{D}1;\text{H}0;\text{R}0;+0]) - [\#7;\text{D}3;\text{H}0;\text{R}1;+0]1- \\ &[\#6;\text{D}2;\text{H}2;\text{R}1;+0]-[\#6;\text{D}3;\text{H}1;\text{R}1;+0](- \\ &[\#6;\text{D}3;\text{H}0;\text{R}1;+0]) - [\#6;\text{D}3;\text{H}1;\text{R}1;+0]1- \\ &[\#6;\text{D}3;\text{H}0;\text{R}0;+0](-[\#7;\text{D}2;\text{H}1;\text{R}0;+0])= \\ &[\#8;\text{D}1;\text{H}0;\text{R}0;+0] \end{aligned} $
1844		$ \begin{aligned} &[\#6;\text{D}2;\text{H}2;\text{R}1;+0]-[\#6;\text{D}2;\text{H}2;\text{R}1;+0]- \\ &[\#7;\text{D}3;\text{H}0;\text{R}1;+0](-[\#6;\text{D}2;\text{H}2;\text{R}0;+0]- \\ &[\#6;\text{D}3;\text{H}0;\text{R}0;+0])(=[\#8;\text{D}1;\text{H}0;\text{R}0;+0]) - \\ &[\#8;\text{D}1;\text{H}1;\text{R}0;+0]) - [\#6;\text{D}3;\text{H}1;\text{R}1;+0](- \\ &[\#6;\text{D}3;\text{H}0;\text{R}0;+0]) - [\#6;\text{D}3;\text{H}1;\text{R}1;+0] \end{aligned} $
1523		$ \begin{aligned} &[\#6;\text{D}2;\text{H}2;\text{R}0;+0]-[\#6;\text{D}3;\text{H}0;\text{R}1;+0](: \\ &[\#7;\text{D}2;\text{H}0;\text{R}1;+0]) : [\#6;\text{D}2;\text{H}1;\text{R}1;+0] : \\ &[\#7;\text{D}3;\text{H}0;\text{R}2;+0](-[\#6;\text{D}2;\text{H}2;\text{R}1;+0]) : \\ &[\#6;\text{D}3;\text{H}0;\text{R}2;+0] \end{aligned} $
1317		$ \begin{aligned} &[\#6;\text{D}2;\text{H}1;\text{R}1;+0] : [\#7;\text{D}2;\text{H}0;\text{R}1;+0] : \\ &[\#6;\text{D}3;\text{H}0;\text{R}1;+0](-[\#6;\text{D}2;\text{H}2;\text{R}0;+0]- \\ &[\#7;\text{D}3;\text{H}0;\text{R}1;+0](-[\#6;\text{D}2;\text{H}2;\text{R}1;+0]- \\ &[\#6;\text{D}2;\text{H}2;\text{R}1;+0]) - [\#6;\text{D}3;\text{H}1;\text{R}1;+0](- \\ &[\#6;\text{D}3;\text{H}0;\text{R}0;+0]) - [\#6;\text{D}3;\text{H}1;\text{R}1;+0]) : \\ &[\#6;\text{D}3;\text{H}0;\text{R}1;+0](: [\#6;\text{D}2;\text{H}1;\text{R}1;+0]) - \\ &[\#8;\text{D}2;\text{H}0;\text{R}0;+0] \end{aligned} $

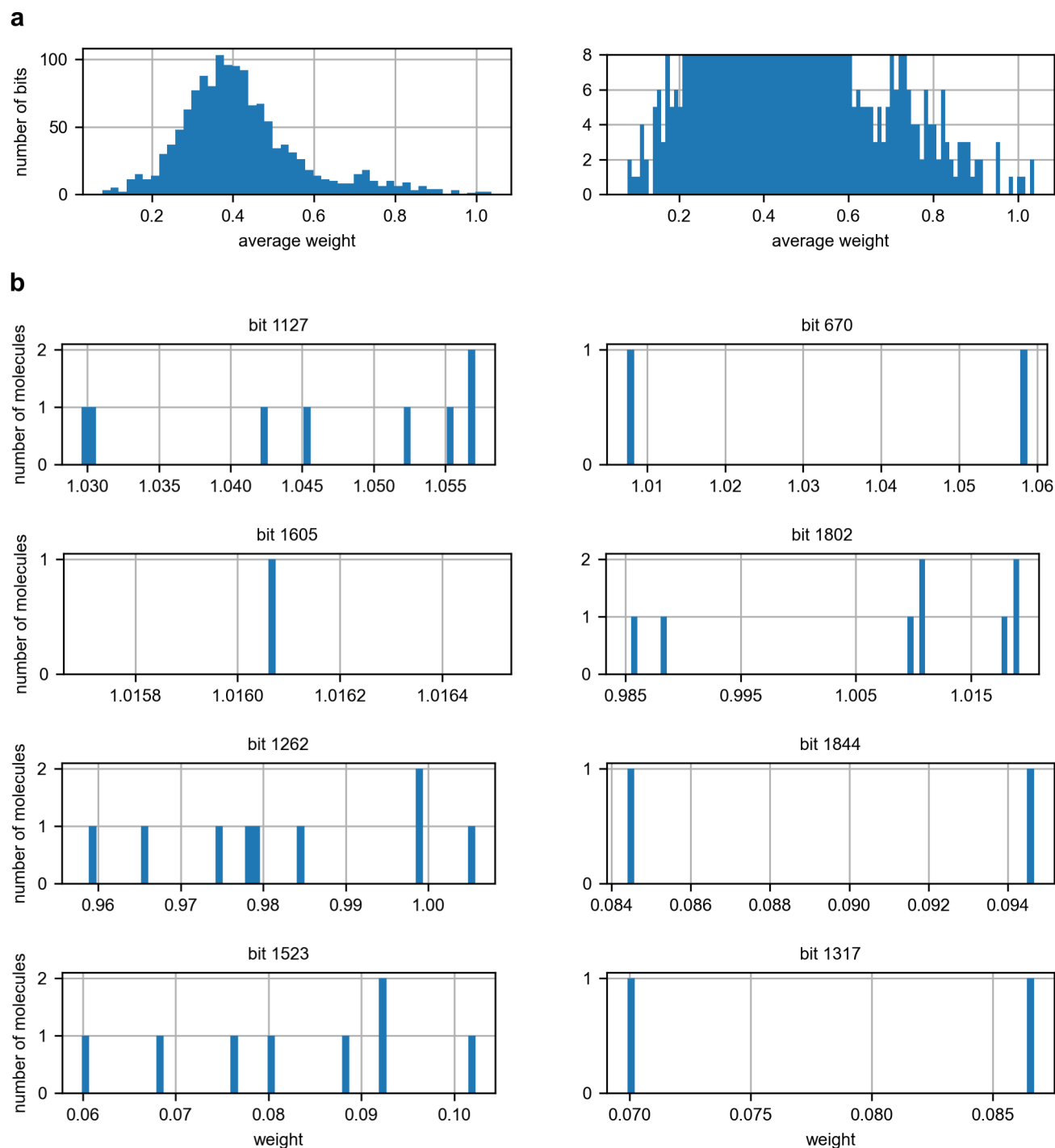


Figure S43: Histograms of **(a)** bit weights (only including bits set by at least one molecule in the dataset; plot shown in full and zoomed in) and **(b)** molecule-level bit weights for substructure-pair analysis on the DD1S CAIX dataset (random split, seed 2; *cf.* Figure 2d), including the top 5 and bottom 3 bits.

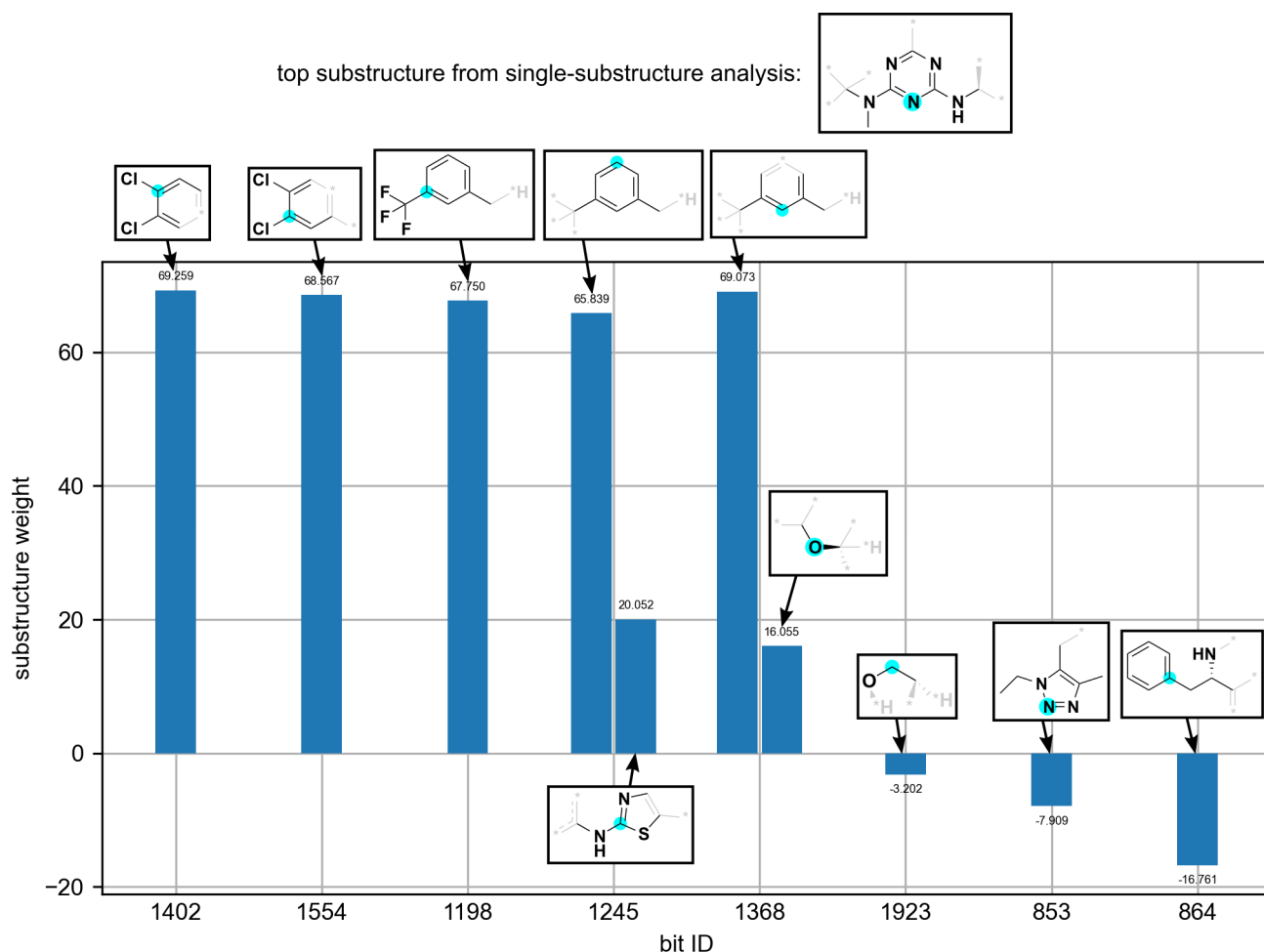
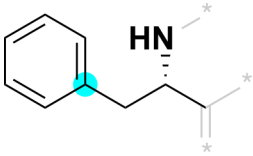


Figure S44: Substructure-pair analysis on the triazine sEH dataset (random split, seed 0; *cf.* Figure 2d), based on the top substructure from the single-substructure analysis.

Table S23: SMARTS for substructure-pair analysis on the triazine sEH dataset (random split, seed 0).

bit ID	substructure example	SMARTS
1402		<chem>[*]1C=CC(Cl)=C(Cl)N1</chem>
1554		<chem>[*]1C=CC(Cl)=C(Cl)N1</chem>

1198		$[#6;D2;H2;R0;+0]-[#6;D3;H0;R1;+0]1:$ $[#6;D2;H1;R1;+0]:[#6;D2;H1;R1;+0]:$ $[#6;D2;H1;R1;+0]:[#6;D3;H0;R1;+0](-$ $[#6;D4;H0;R0;+0](-[#9;D1;H0;R0;+0])(-$ $[#9;D1;H0;R0;+0])-[#9;D1;H0;R0;+0]):$ $[#6;D2;H1;R1;+0]:1$
1245		$[#6;D2;H2;R0;+0]-[#6;D3;H0;R1;+0]1:$ $[#6;D2;H1;R1;+0]:[#6;D2;H1;R1;+0]:$ $[#6;D2;H1;R1;+0]:[#6;D3;H0;R1;+0](-$ $[#6;D4;H0;R0;+0]):[#6;D2;H1;R1;+0]:1$
1245		$[#6;D2;H1;R1;+0]:[#7;D2;H0;R1;+0]:$ $[#6;D3;H0;R1;+0](:[#16;D2;H0;R1;+0]:$ $[#6;D3;H0;R1;+0])-[#7;D2;H1;R0;+0]-$ $[#6;D3;H0;R1;+0]$
1368		$[#6;D2;H1;R1;+0]:[#6;D3;H0;R1;+0](-$ $[#6;D2;H2;R0;+0]):[#6;D2;H1;R1;+0]:$ $[#6;D3;H0;R1;+0](:[#6;D2;H1;R1;+0])-$ $[#6;D4;H0;R0;+0]$
1368		$[#6;D3;H1;R0;+0]-[#8;D2;H0;R0;+0]-$ $[#6;D4;H0;R1;+0]$
1923		$[#6;D3;H1;R2;+0]-[#6;D2;H2;R1;+0]-$ $[#8;D2;H0;R1;+0]$
853		$[#6;D1;H3;R0;+0]-[#6;D2;H2;R0;+0]-$ $[#7;D3;H0;R1;+0]1:[#7;D2;H0;R1;+0]:$ $[#7;D2;H0;R1;+0]:[#6;D3;H0;R1;+0](-$ $[#6;D1;H3;R0;+0]):[#6;D3;H0;R1;+0]:1-$ $[#6;D2;H2;R0;+0]$

864		$[\#6;\text{D}3;\text{H}0;\text{R}0;+0]-[\#6;\text{D}3;\text{H}1;\text{R}0;+0](-$ $[\#7;\text{D}2;\text{H}1;\text{R}0;+0])-[\#6;\text{D}2;\text{H}2;\text{R}0;+0]-$ $[\#6;\text{D}3;\text{H}0;\text{R}1;+0]1:[\#6;\text{D}2;\text{H}1;\text{R}1;+0]:$ $[\#6;\text{D}2;\text{H}1;\text{R}1;+0]:[\#6;\text{D}2;\text{H}1;\text{R}1;+0]:$ $[\#6;\text{D}2;\text{H}1;\text{R}1;+0]:[\#6;\text{D}2;\text{H}1;\text{R}1;+0]:1$
-----	---	--

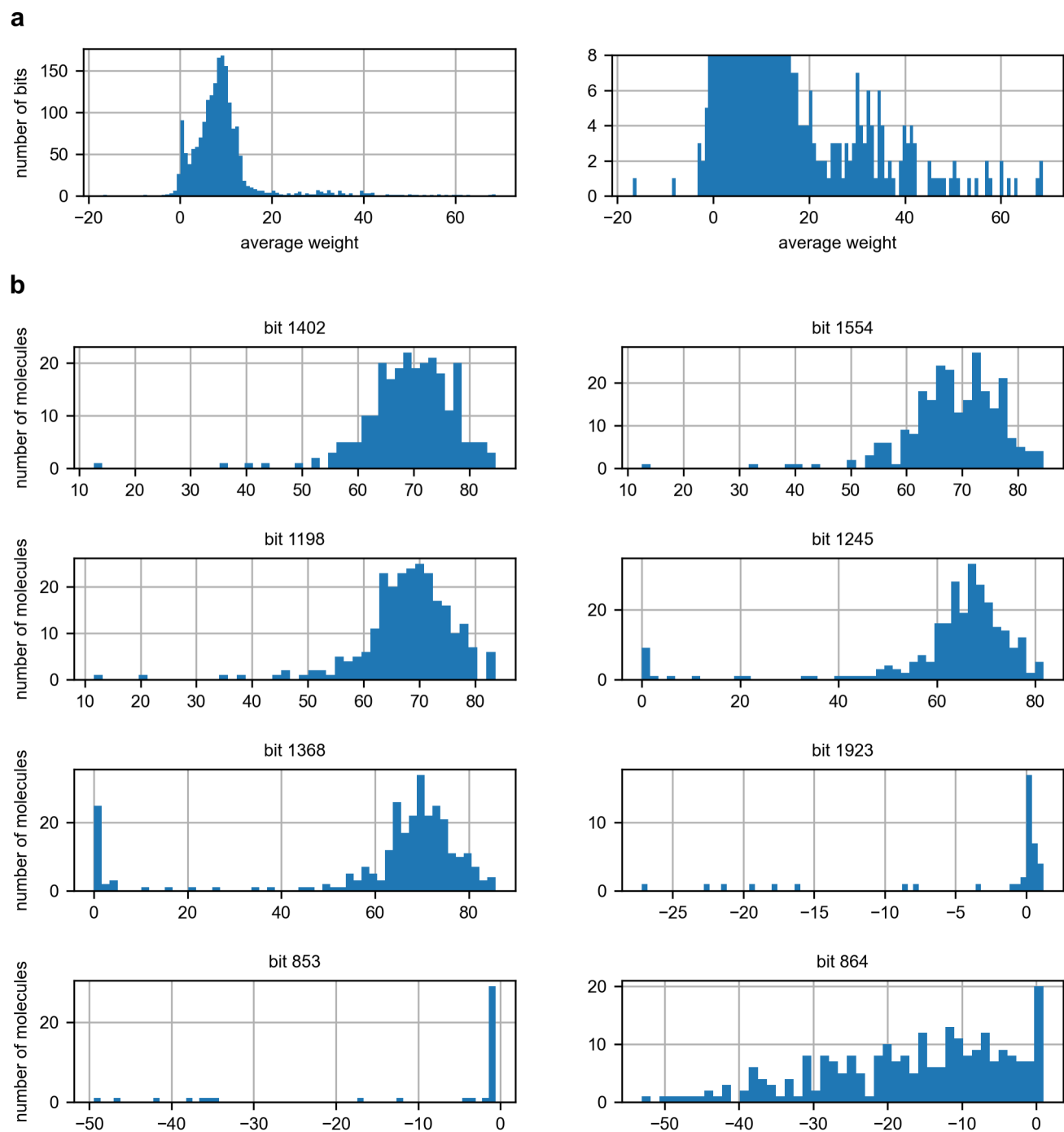


Figure S45: Histograms of **(a)** bit weights (only including bits set by at least one molecule in the dataset; plot shown in full and zoomed in) and **(b)** molecule-level bit weights for substructure-pair analysis on the triazine SEH dataset (random split, seed 0; cf. Figure 2d), including the top 5 and bottom 3 bits.

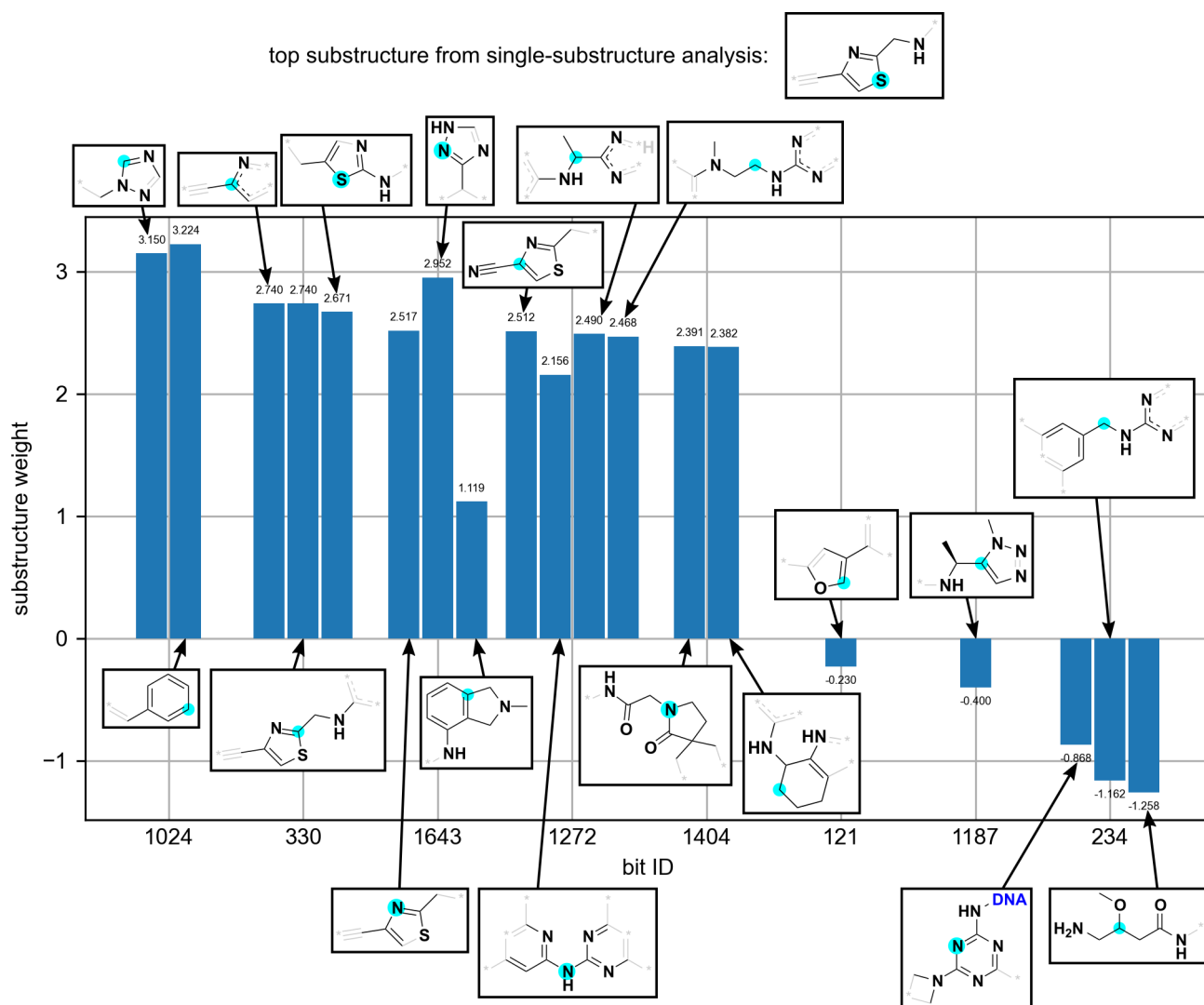
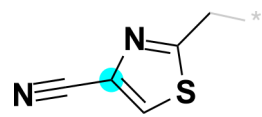
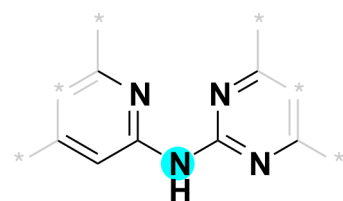
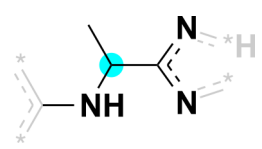
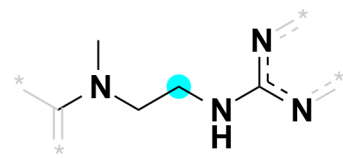
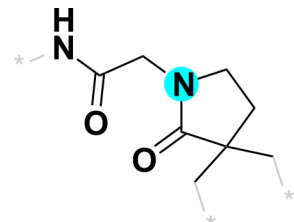
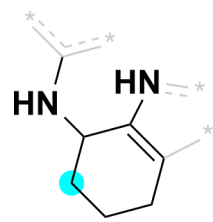
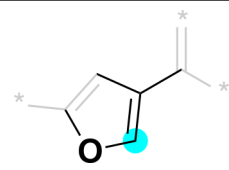
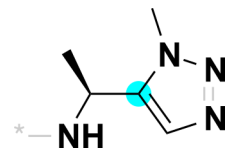
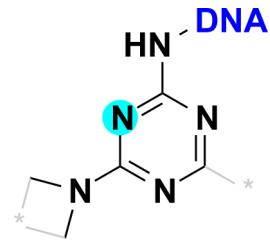
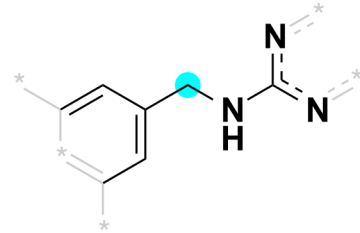


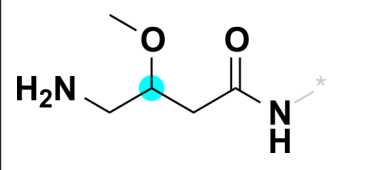
Figure S46: Substructure-pair analysis on the triazine SIRT2 dataset (random split, seed 0; *cf.* Figure 2d), based on the top substructure from the single-substructure analysis.

Table S24: SMARTS for substructure-pair analysis on the triazine SIRT2 dataset (random split, seed 0).

bit ID	substructure example	SMARTS
1024		<chem>[*]c1nn[nH]1</chem> <chem>[*]c1nn[nH]1</chem> <chem>[*]c1nn[nH]1</chem>
1024		<chem>[*]c1ccccc1</chem> <chem>[*]c1ccccc1</chem> <chem>[*]c1ccccc1</chem>

1272		$[\#6;D2;H2;R0;+0]-[\#6;D3;H0;R1;+0]1:$ $[\#16;D2;H0;R1;+0]:[\#6;D2;H1;R1;+0]:$ $[\#6;D3;H0;R1;+0](-[\#6;D2;H0;R0;+0]\#$ $[\#7;D1;H0;R0;+0]):[\#7;D2;H0;R1;+0]:1$
1272		$[\#6;D3;H0;R1;+0]:[\#6;D2;H1;R1;+0]:$ $[\#6;D3;H0;R1;+0]([\#7;D2;H0;R1;+0]:$ $[\#6;D3;H0;R1;+0])-[\#7;D2;H1;R0;+0]-$ $[\#6;D3;H0;R1;+0]([\#7;D2;H0;R1;+0]:$ $[\#6;D3;H0;R1;+0]):[\#7;D2;H0;R1;+0]:$ $[\#6;D3;H0;R1;+0]$
1272		$[\#6;D1;H3;R0;+0]-[\#6;D3;H1;R0;+0](-$ $[\#7;D2;H1;R0;+0]-[\#6;D3;H0;R1;+0])-$ $[\#6;D3;H0;R1;+0]([\#7;D2;H0;R1;+0]):$ $[\#7;D2;H0;R1;+0]$
1272		$[\#6;D1;H3;R0;+0]-[\#7;D3;H0;R0;+0](-$ $[\#6;D3;H0;R0;+0])-[\#6;D2;H2;R0;+0]-$ $[\#6;D2;H2;R0;+0]-[\#7;D2;H1;R0;+0]-$ $[\#6;D3;H0;R1;+0]([\#7;D2;H0;R1;+0]):$ $[\#7;D2;H0;R1;+0]$
1404		$[\#6;D2;H2;R1;+0]-[\#6;D4;H0;R2;+0]1(-$ $[\#6;D2;H2;R1;+0])-[\#6;D2;H2;R1;+0]-$ $[\#6;D2;H2;R1;+0]-[\#7;D3;H0;R1;+0](-$ $[\#6;D2;H2;R0;+0]-[\#6;D3;H0;R0;+0](-$ $[\#7;D2;H1;R0;+0])=[\#8;D1;H0;R0;+0])-$ $[\#6;D3;H0;R1;+0]-1=[\#8;D1;H0;R0;+0]$

1404		[#6;D3;H0;R1;+0]-[#7;D2;H1;R0;+0]- [#6;D3;H1;R1;+0]1-[#6;D2;H2;R1;+0]- [#6;D2;H2;R1;+0]-[#6;D2;H2;R1;+0]- [#6;D3;H0;R2;+0]:[#6;D3;H0;R2;+0]-1: [#7;D2;H1;R1;+0]
121		[#6;D2;H1;R1;+0]:[#6;D3;H0;R1;+0](- [#6;D3;H0;R0;+0]):[#6;D2;H1;R1;+0]: [#8;D2;H0;R1;+0]:[#6;D3;H0;R1;+0]
1187		[#6;D1;H3;R0;+0]-[#6;D3;H1;R0;+0](- [#7;D2;H1;R0;+0])-[#6;D3;H0;R1;+0](: [#6;D2;H1;R1;+0]:[#7;D2;H0;R1;+0]): [#7;D3;H0;R1;+0](-[#6;D1;H3;R0;+0]): [#7;D2;H0;R1;+0]
234		[#102;D1;H0;R0;+0]-[#7;D2;H1;R0;+0]- [#6;D3;H0;R1;+0]1:[#7;D2;H0;R1;+0]: [#6;D3;H0;R1;+0]:[#7;D2;H0;R1;+0]: [#6;D3;H0;R1;+0](-[#7;D3;H0;R1;+0](- [#6;D2;H2;R1;+0])-[#6;D2;H2;R1;+0]): [#7;D2;H0;R1;+0]:1
234		[#6;D3;H0;R1;+0]:[#6;D2;H1;R1;+0]: [#6;D3;H0;R1;+0](:[#6;D2;H1;R1;+0]: [#6;D3;H0;R1;+0])-[#6;D2;H2;R0;+0]- [#7;D2;H1;R0;+0]-[#6;D3;H0;R1;+0](: [#7;D2;H0;R1;+0]):[#7;D2;H0;R1;+0]

234		$ \begin{aligned} & [\#6;D1;H3;R0;+0] - [\#8;D2;H0;R0;+0] - \\ & [\#6;D3;H1;R0;+0] (-[\#6;D2;H2;R0;+0] - \\ & [\#7;D1;H2;R0;+0]) - [\#6;D2;H2;R0;+0] - \\ & [\#6;D3;H0;R0;+0] (-[\#7;D2;H1;R0;+0]) = \\ & [\#8;D1;H0;R0;+0] \end{aligned} $
-----	---	---

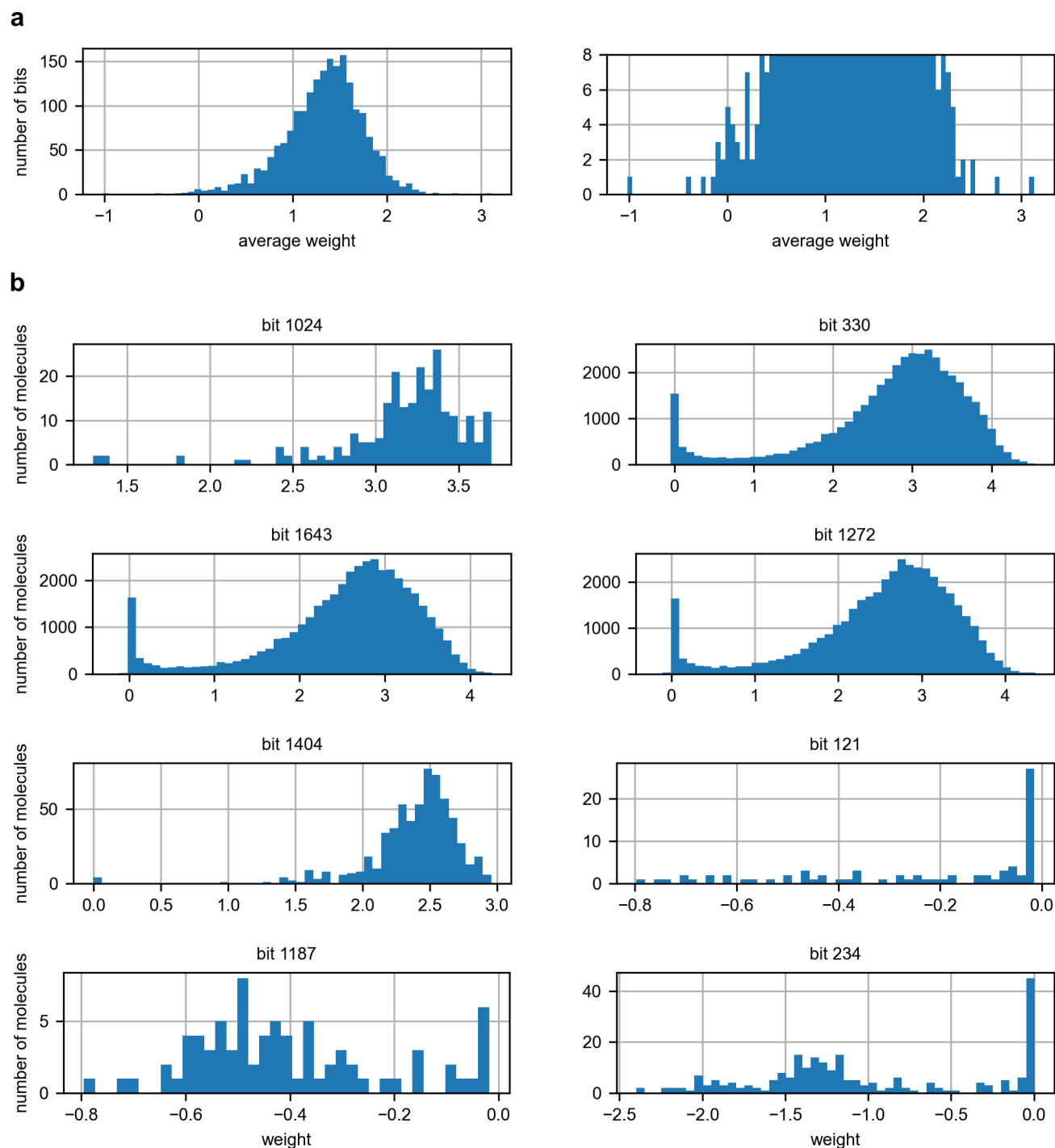


Figure S47: Histograms of **(a)** bit weights (only including bits set by at least one molecule in the dataset; plot shown in full and zoomed in) and **(b)** molecule-level bit weights for substructure-pair analysis on the triazine SIRT2 dataset (random split, seed 0; *cf.* Figure 2d), including the top 5 and bottom 3 bits.

S2.10 Parity plots to evaluate ability to generalize on the triazine sEH and SIRT2 datasets

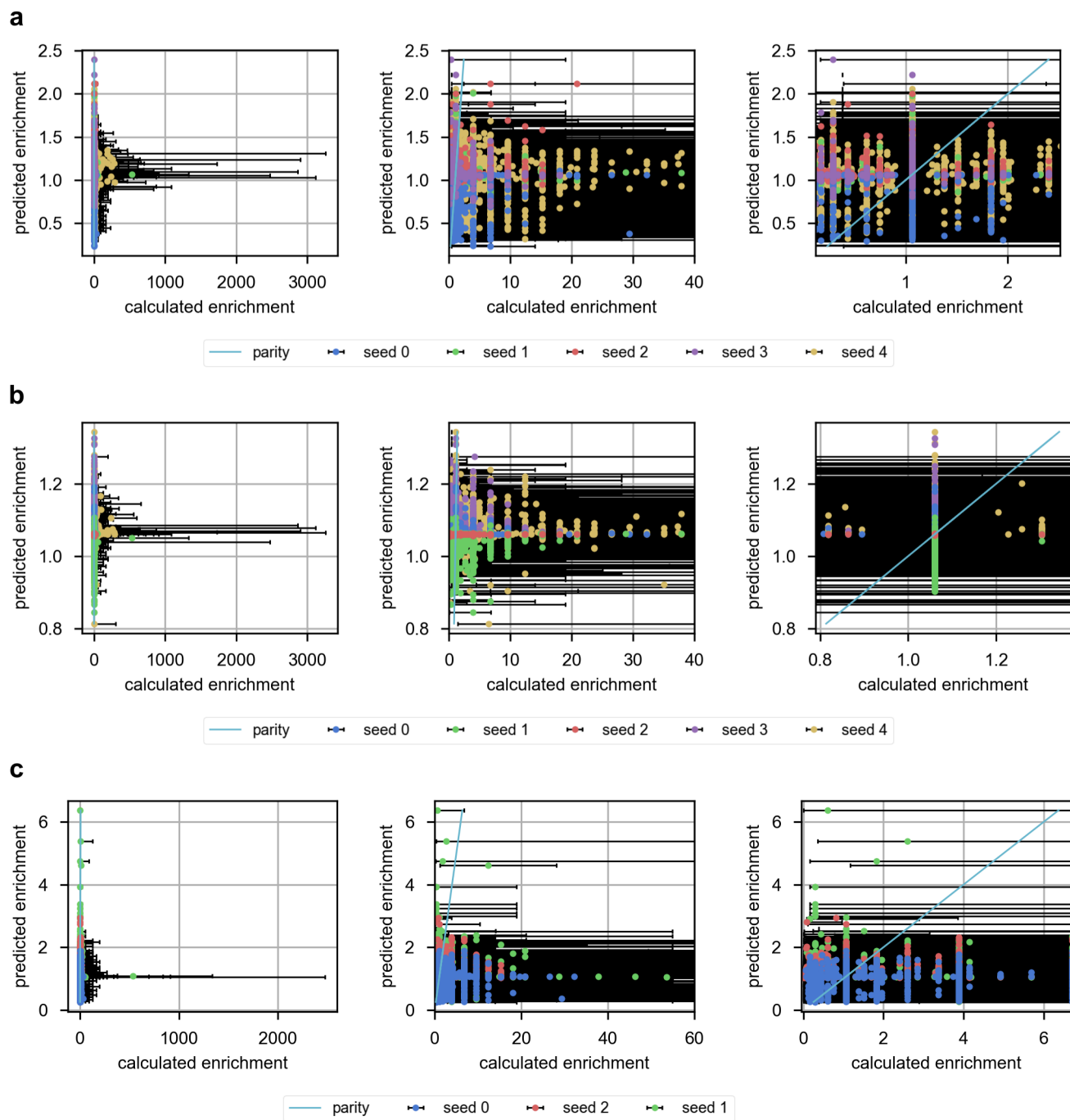


Figure S48: Scatter plots (full and zoomed-in) of predicted versus calculated enrichments for (a) FP-FFNN, (b) OH-FFNN, (c) D-MPNN on five cycle-1+2+3 splits (*cf.* Figure 2d) of the triazine sEH dataset. Only the subset of test-set compounds with all building blocks in the test set are included for each split. The light blue parity line is the identity function, for reference. Error bars represent 95% confidence intervals for calculated enrichments.

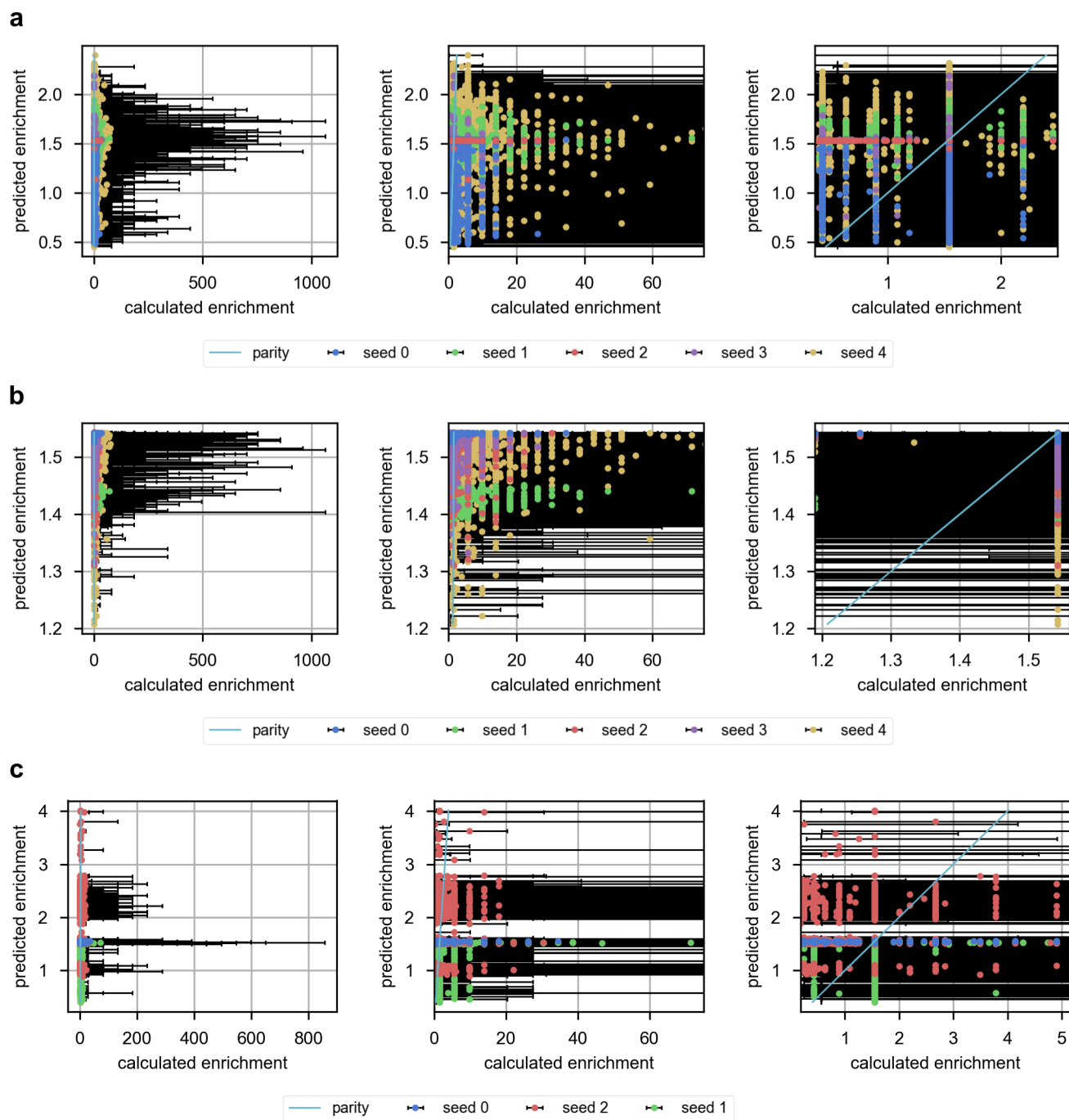


Figure S49: Scatter plots (full and zoomed-in) of predicted versus calculated enrichments for **(a)** FP-FFNN, **(b)** OH-FFNN, **(c)** D-MPNN on five cycle-1+2+3 splits (*cf.* Figure 2d) of the triazine SIRT2 dataset. Only the subset of test-set compounds with all building blocks in the test set are included for each split. The light blue parity line is the identity function, for reference. Error bars represent 95% confidence intervals for calculated enrichments.

S2.11 Atom-centered Gaussian visualizations for top predicted compounds

S2.11.1 Random split

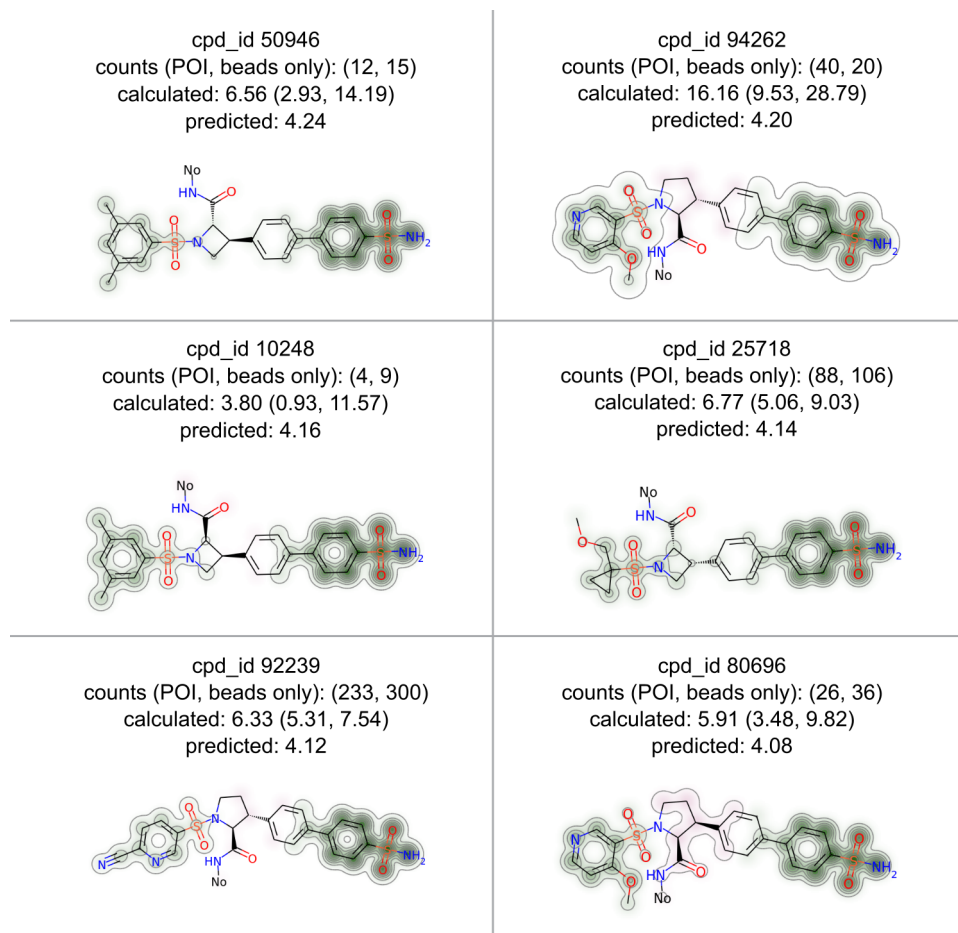


Figure S50: Atom-centered Gaussian visualizations for the top 6 predicted compounds from the test set of a FP-FFNN on a random split (seed 0; *cf.* Figure 2d) of the DD1S CAIX dataset. Atoms contributing positively to enrichment are highlighted in green, and atoms contributing negatively to enrichment are highlighted in pink, with color intensity corresponding to the level of contribution to enrichment. “No” represents the DNA linker attachment point. Compound IDs (“cpd_id”) are sequential based on building block cycle numbers.

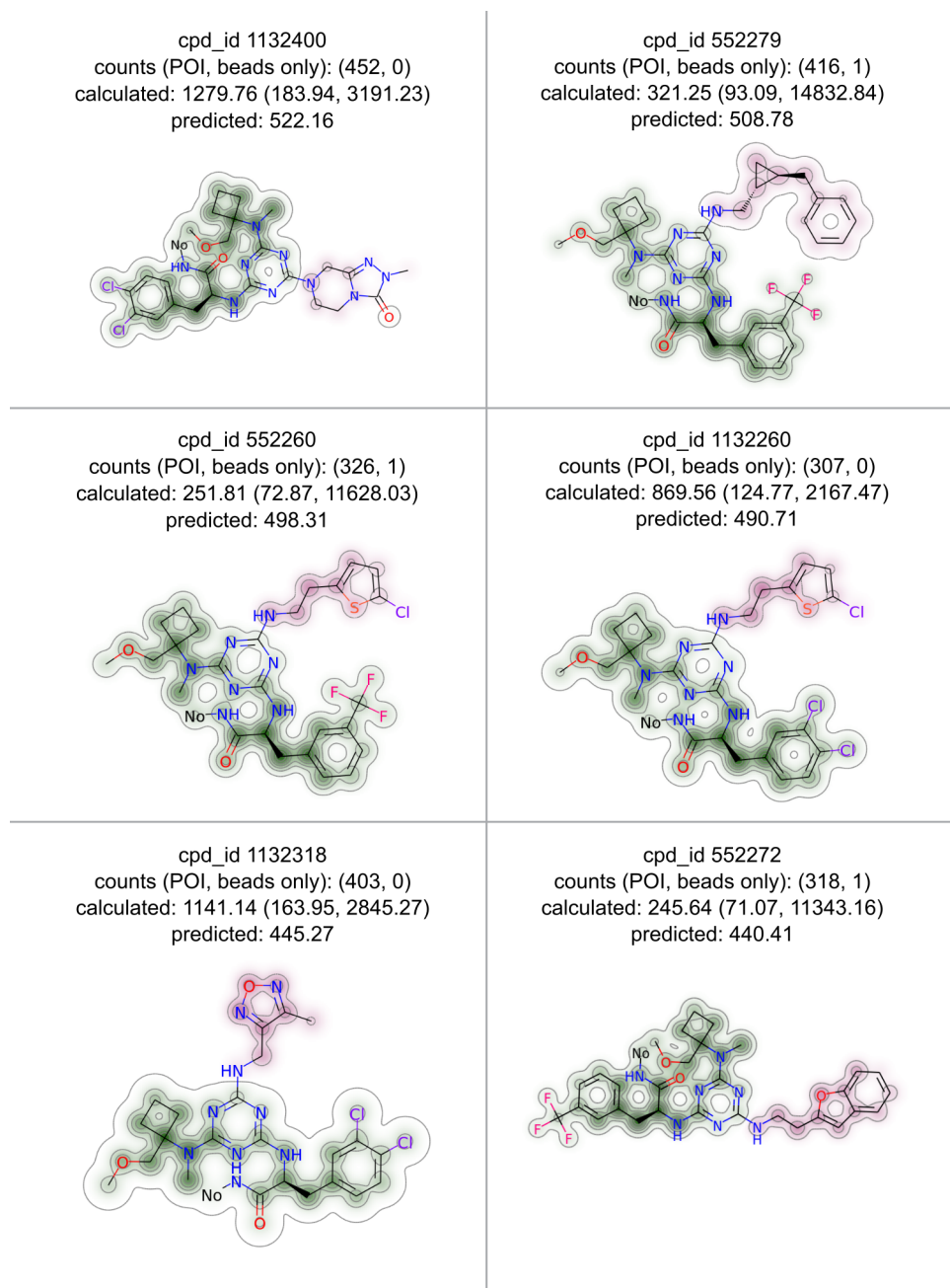


Figure S51: Atom-centered Gaussian visualizations for the top 6 predicted compounds from the test set of a FP-FFNN on a random split (seed 0; *cf.* Figure 2d) of the triazine sEH dataset. Atoms contributing positively to enrichment are highlighted in green, and atoms contributing negatively to enrichment are highlighted in pink, with color intensity corresponding to the level of contribution to enrichment. “No” represents the DNA linker attachment point. Compound IDs (“cpd_id”) are sequential based on building block cycle numbers.

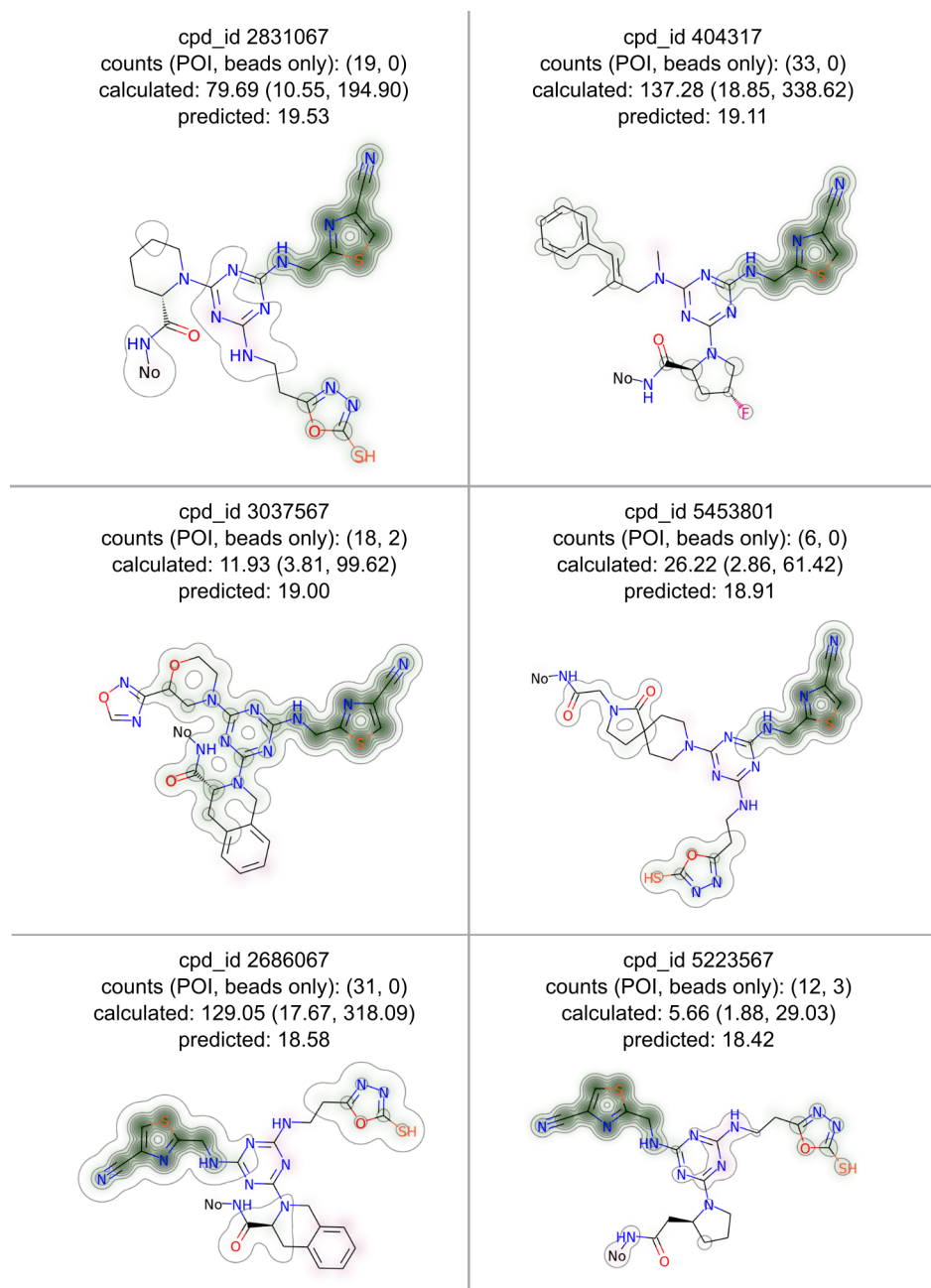


Figure S52: Atom-centered Gaussian visualizations for the top 6 predicted compounds from the test set of a FP-FFNN on a random split (seed 0; *cf.* Figure 2d) of the triazine SIRT2 dataset. Atoms contributing positively to enrichment are highlighted in green, and atoms contributing negatively to enrichment are highlighted in pink, with color intensity corresponding to the level of contribution to enrichment. “No” represents the DNA linker attachment point. Compound IDs (“cpd_id”) are sequential based on building block cycle numbers.

S2.11.2 Cycle-1+2+3 split

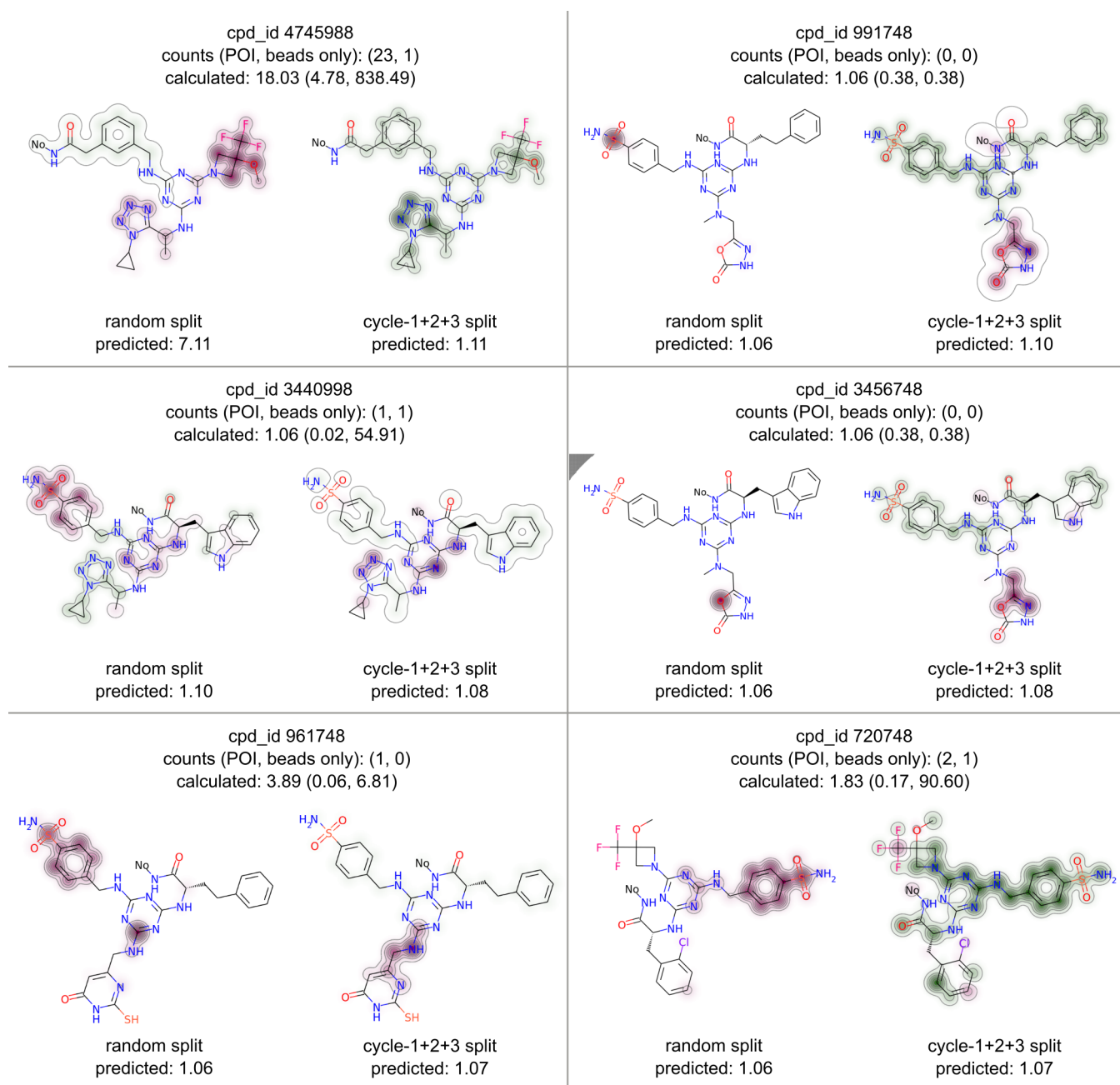


Figure S53: Atom-centered Gaussian visualizations for the top 6 predicted compounds with all building blocks uniquely in the test set for a FP-FFNN on a cycle-1+2+3 split (seed 0; *cf.* Figure 2d) of the triazine sEH dataset. These compounds do not contain any of the building blocks the cycle-1+2+3 split model was trained on. For comparison, corresponding visualizations based on the predictions of a FP-FFNN on a random split (seed 0; *cf.* Figure 2d) of the dataset are also shown. Atoms contributing positively to enrichment are highlighted in green, and atoms contributing negatively to enrichment are highlighted in pink, with color intensity corresponding to the level of contribution to enrichment. “No” represents the DNA linker attachment point. Compound IDs (“cpd_id”) are sequential based on building block cycle numbers.

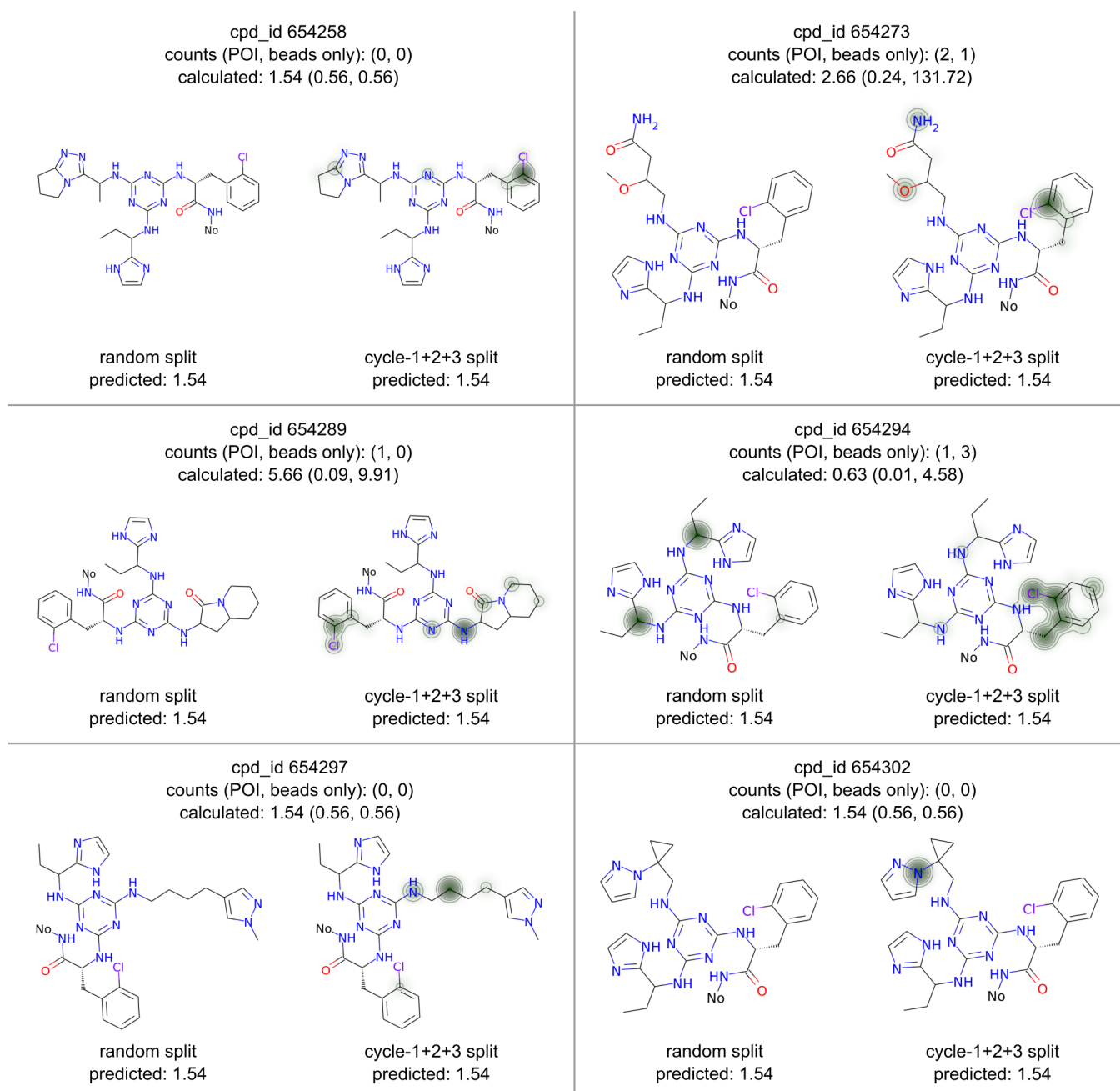


Figure S54: Atom-centered Gaussian visualizations for the top 6 predicted compounds with all building blocks uniquely in the test set for a FP-FFNN on a cycle-1+2+3 split (seed 0; cf. Figure 2d) of the triazine SIRT2 dataset. These compounds do not contain any of the building blocks the cycle-1+2+3 split model was trained on. For comparison, corresponding visualizations based on the predictions of a FP-FFNN on a random split (seed 0; cf. Figure 2d) of the dataset are also shown. Atoms contributing positively to enrichment are highlighted in green, and atoms contributing negatively to enrichment are highlighted in pink, with color intensity corresponding to the level of contribution to enrichment. “No” represents the DNA linker attachment point. Compound IDs (“cpd_id”) are sequential based on building block cycle numbers.

S2.12 Chemical similarity between Enamine on-demand libraries and top compounds from DD1S CAIX dataset

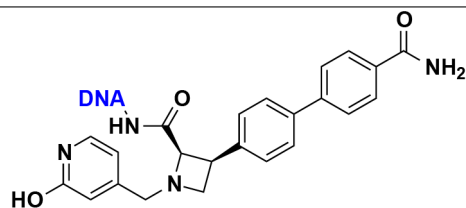
Table S25: Top hits from similarity searches in the Enamine REAL database and Enamine screening collection, for the top 5 compounds (by lower bound of calculated enrichment) in the DD1S CAIX dataset. “No” represents the DNA linker attachment point.

DD1S compound	nearest two hits in Enamine REAL database	nearest two hits in Enamine screening collection

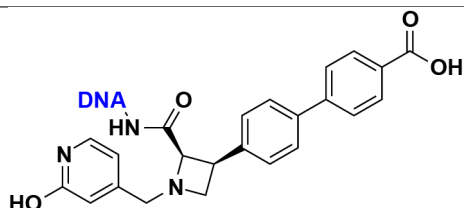
S2.13 DD1S CAIX outliers

Table S26: Example outliers (with high calculated enrichment but low predicted enrichment) and their nearest neighbors (as determined by a FP-KNN model trained on the entire DD1S CAIX dataset) in the test set of a FP-FFNN on a random split (seed 0) of the DD1S CAIX dataset. Compound IDs (“cpd_id”) are sequential based on building block cycle numbers.

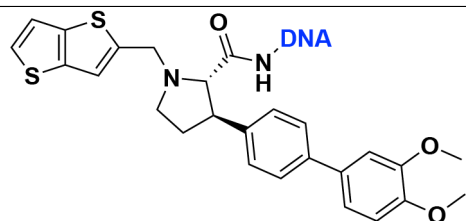
outlier	nearest neighbor
---------	------------------



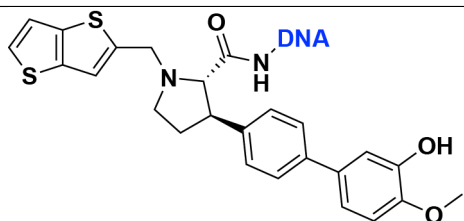
cpd_id 3858
counts (POI, beads only): (2, 0)
calculated: 51.63 (3.00, 107.22)
predicted: 1.13



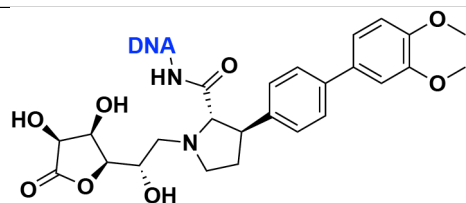
cpd_id 3855
counts (POI, beads only): (4, 20)
calculated: 1.75 (0.45, 4.45)
predicted: 1.06



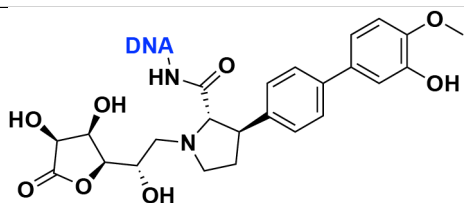
cpd_id 87395
counts (POI, beads only): (1, 0)
calculated: 29.89 (0.46, 52.37)
predicted: 1.05



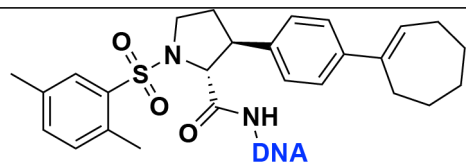
cpd_id 87351
counts (POI, beads only): (1, 4)
calculated: 2.56 (0.05, 15.36)
predicted: 0.99



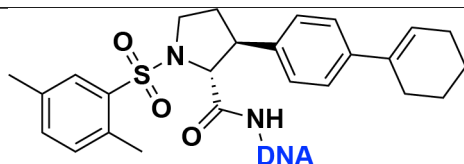
cpd_id 81921
counts (POI, beads only): (1, 0)
calculated: 29.89 (0.46, 52.37)
predicted: 1.06



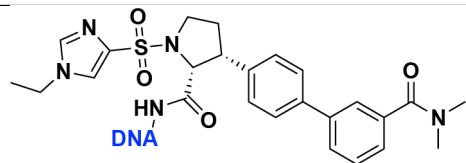
cpd_id 81877
counts (POI, beads only): (1, 6)
calculated: 1.76 (0.04, 8.72)
predicted: 1.07



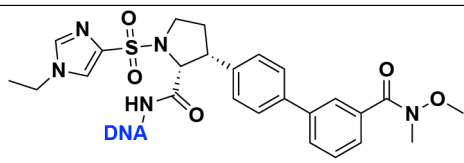
cpd_id 104265
counts (POI, beads only): (1, 0)
calculated: 29.89 (0.46, 52.37)
predicted: 1.09



cpd_id 104321
counts (POI, beads only): (0, 10)
calculated: 0.29 (0.12, 2.41)
predicted: 1.05



cpd_id 66579
counts (POI, beads only): (1, 0)
calculated: 29.89 (0.46, 52.37)
predicted: 1.14



cpd_id 66525
counts (POI, beads only): (1, 9)
calculated: 1.20 (0.03, 5.24)
predicted: 1.00

References

- (S1) Kuai, L.; O’Keeffe, T.; Arico-Muendel, C. Randomness in DNA Encoded Library Selection Data Can Be Modeled for More Reliable Enrichment Calculation. *SLAS Discovery* **2018**, *23*, 405–416.
- (S2) Gu, K.; Ng, H. K. T.; Tang, M. L.; Schucany, W. R. Testing the Ratio of Two Poisson Rates. *Biom. J.* **2008**, *50*, 283–298.
- (S3) McCloskey, K.; Sigel, E. A.; Kearnes, S.; Xue, L.; Tian, X.; Moccia, D.; Gikunju, D.; Bazzaz, S.; Chan, B.; Clark, M. A.; Cuzzo, J. W.; Guié, M.-A.; Guiling, J. P.; Huguet, C.; Hupp, C. D.; Keefe, A. D.; Mulhern, C. J.; Zhang, Y.; Riley, P. Machine Learning on DNA-Encoded Libraries: A New Paradigm for Hit Finding. *J. Med. Chem.* **2020**, *63*, 8857–8866.